



TECHNISCHE
UNIVERSITÄT
WIEN
Vienna | Austria



Diplomarbeit

Stability Analysis and State Multiplicity of Incompressible Buoyancy-Driven Flows in an Inclined Differentially Heated Square Cavity

ausgeführt zum Zwecke der Erlangung des akademischen Grades eines Diplom-Ingenieurs

(Dipl.-Ing.), eingereicht an der TU Wien, Fakultät für Maschinenwesen und

Betriebswissenschaften, von

Giousef-Alexandros Charinti

Mat. Num.: 1127666

unter der Leitung von

Univ.-Prof. Hendrik C. Kuhlmann

Dr.techn. Pierre-Emmanuel des Bosc

Institut für Strömungsmechanik und Wärmeübertragung

Wien, Juni 2022

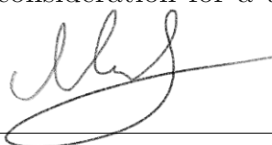
I confirm, that going to press of this thesis needs the confirmation of the examination committee.

Affidavit

I declare in lieu of oath, that I wrote this thesis and performed the associated research myself, using only literature cited in this volume. If text passages from sources are used literally, they are marked as such.

I confirm that this work is original and has not been submitted elsewhere for any examination, nor is it currently under consideration for a thesis elsewhere.

Vienna, June 2022


Giousef-Alexandros Charinti

Zusammenfassung

Es wird die inkompressible Strömung im Inneren eines geneigten, unterschiedlich beheizten quadratischen Behälters untersucht. Zwei gegenüberliegende Behälterwände werden bei einer konstanten und gleichmäßigen Temperatur beheizt, respektive gekühlt. Die übrigen Seitenwände werden entweder als perfekt leitend oder adiabatisch modelliert. Der Behälter ist im zweidimensionalen Raum so geneigt, dass eine Beheizung von unten einem Neigungswinkel von $\alpha = 0^\circ$ und eine Beheizung von oben einem Neigungswinkel von $\alpha = 180^\circ$ entspricht.

Zunächst wird die stationäre Lösung der zweidimensionalen Strömung mit dem Neigungswinkel $\alpha \in [-180^\circ, 180^\circ]$ betrachtet. Wird die Flüssigkeit von unten beheizt, werden neben dem klassischen bewegungslosen Zustand der Rayleigh-Bénard-Konvektion, auch andere stationäre Lösungen beobachtet. Diese Lösungen unterliegen unterschiedlichen Wirbelbildungen, welche den Behälter ausfüllen. Sie sind durch Variationen des Neigungswinkels kontinuierlich und nahtlos miteinander verbunden. Diese Zustandsvielfalt wird sowohl bei perfekt leitenden als auch adiabatischen Seitenwänden aufgefunden. In beiden Fällen werden mehrere Zustände mit einer ähnlichen Strömungsstruktur beobachtet. Um einen Vergleich der verschiedenen stationären Lösungen zu erreichen, wird der Wärmeübergang der heißen Wand als Funktion des Neigungswinkels dargestellt.

Als nächstes wird die Stabilität der Strömung in einem Behälter mit perfekt leitenden Seitenwänden untersucht. Die Strömung wird in eine zweidimensionale Grundströmung und eine dreidimensionale Störungsströmung aufgeteilt. Mit Hilfe einer linearen Stabilitätsanalyse wird die Störungsströmung durch einen Normalmodenansatz dargestellt. Dabei wird angenommen, dass der Behälter in der dritten Dimension unendlich ausgedehnt ist. Es wird der Verlauf von Parametern wie der kritischen Rayleigh-Zahl, der Wellenzahl und der Schwingungsfrequenz in Abhängigkeit vom Neigungswinkel gezeigt. Die lineare Stabilitätsanalyse zeigt eine erhöhte Stabilität, wenn das Fluid von oben beheizt wird, im Gegensatz zu einer Beheizung von unten. Im ersten Fall zeigt eine Untersuchung der Änderungsrate der kinetischen Energie, dass die Destabilisierung hauptsächlich auf den Strömungsimpuls und im zweiten Fall auf den Auftrieb zurückzuführen ist.



Die approbierte gedruckte Originalversion dieser Diplomarbeit ist an der TU Wien Bibliothek verfügbar
The approved original version of this thesis is available in print at TU Wien Bibliothek.

Abstract

The incompressible flow inside an inclined differentially heated square cavity is investigated. Two walls of the cavity opposite to each other are heated and cooled at a constant and uniform temperature and the remainder lateral walls are modelled as either perfectly conducting or adiabatic. The cavity is tilted in the two dimensional space such that an inclination angle of $\alpha = 0^\circ$ corresponds to a heating from below and $\alpha = 180^\circ$ to a heating from above.

First, we consider the steady state solutions of the two dimensional flow for inclination angles $\alpha \in [-180^\circ, 180^\circ]$. Alongside the classical motionless state of Rayleigh–Bénard convection, other steady states are found when the fluid is heated from below. These solutions, composed of a different number of vortices filling the cavity, are smoothly connected with each other by varying the cavity's inclination angle. This observed state multiplicity is investigated for both perfectly conducting and adiabatic lateral walls, with both cases delivering multiple states with a similar flow structure. In order to compare the different steady states to each other, the heat transfer of the hot wall is shown as a function of the inclination angle.

Second, the flow stability inside a cavity with perfectly conducting lateral walls is investigated. The flow is decomposed into a two dimensional basic flow and a three dimensional perturbation flow. Using a linear stability analysis, the perturbation flow is represented by a normal mode ansatz, assuming the cavity is infinitely extended in the third dimension. We show the curve of parameters such as the critical Rayleigh number, wavenumber and mode oscillation frequency as a function of the inclination angle. The linear stability analysis shows an increased stability when the fluid is heated from above compared to a heating from below. In the former case, a study of the growth of the kinetic energy reveals that the destabilisation can be attributed mainly to inertia and in the latter case, to buoyancy.



Die approbierte gedruckte Originalversion dieser Diplomarbeit ist an der TU Wien Bibliothek verfügbar
The approved original version of this thesis is available in print at TU Wien Bibliothek.

Acknowledgments

I shall start by expressing my sincere gratitude to Prof. Hendrik C. Kuhlmann for his thorough and helpful feedback on my thesis, who taught me the need of accuracy and precision in scientific writing. He has been an inspiration for me and a driving factor behind my decision on pursuing a career in research.

I would like to extend my sincere thanks to my supervisor, Pierre-Emmanuel des Bosc, for his guidance, patience and support throughout all stages of this thesis. I could not have asked for a better supervisor.

I would also like to thank the institute and its people for providing me with a nice and friendly working environment which was decisive in completing my thesis and further inspired me to continue working in research.

I am also deeply thankful for the continuous support I have received over the years from my family. I also thank all of my friends who stood by me in difficult times and pushed me to continue. Finally, I wish to thank my partner for supporting me throughout my journey in research and for always being there for me. I could not have done this without her.



Die approbierte gedruckte Originalversion dieser Diplomarbeit ist an der TU Wien Bibliothek verfügbar
The approved original version of this thesis is available in print at TU Wien Bibliothek.

Contents

1	Introduction	1
1.1	Natural Convection	1
1.2	Hydrodynamic Stability	2
1.3	Buoyancy Driven Flows in Cavities	4
1.4	Flow State Multiplicity	6
2	Theoretical Basics	7
2.1	The Inclined Differentially Heated Cavity	7
2.2	Equations of Fluid Dynamics	8
2.3	Boundary Conditions	9
2.4	Basic Flow	9
2.5	Linear Stability	9
2.6	Dynamical System Formulation	10
2.7	A Posteriori Energy Analysis	11
3	Numerical Methods	13
3.1	Weak Formulation	13
3.2	Python Packages	14
3.3	Discretisation	14
3.4	Basic Flow	15
3.5	Eigenvalue Problem	16
3.6	Spectral Element Solver: NEK5000	17
3.7	Arc Length Continuation for the Basic Flow	18
3.8	Continuation Method for Neutral Curve Tracking	19
3.9	Coarse Eigenvalue Study	21
3.10	Neutral Curve Tracking	23
3.10.1	Inner Loop: Ra over k	23
3.10.2	Outer Loop: Ra over α	24
3.10.3	Error Handling	25
4	Validation	27
4.1	Convergence Study	27
4.2	Modes at $\alpha = 90^\circ$	27
4.3	Neutral Curve of Mode 1	28
5	Steady State Multiplicity	31
5.1	Perfectly Conducting Lateral Walls	32
5.1.1	Solution set at $Ra = 2.5 \times 10^4$, conducting lateral walls	32
5.1.2	Solution sets at $Ra = 10^5$, conducting lateral walls	35
5.2	Adiabatic Lateral Walls	38
5.2.1	Solution sets at $Ra = 2.5 \times 10^4$, adiabatic lateral walls	40
5.2.2	Solution sets at $Ra = 10^5$, adiabatic lateral walls	40
5.3	Comparison of the State Multiplicity	43

5.3.1	Variation of the Rayleigh number	43
5.3.2	Conducting or Adiabatic Lateral Walls	46
6	Linear Stability Analysis	47
6.1	Neutral and Critical Curves over the Inclination Angle α	47
6.2	Three Dimensional Flow Perturbation	49
7	Conclusion	55
7.1	Steady State Multiplicity	55
7.2	Linear Stability Analysis	56
	Bibliography	57

1.1 Natural Convection

An example of natural convection is a flow which is the result of a temperature change from an external heating or cooling source. Initially, a small temperature gradient leads to heat conduction between the fluid molecules. As the temperature gradient increases, density changes start to create a flow within the fluid, which is directed from the high density areas to the lower density areas. In case of a heated or cooled fluid, the flow is directed from the hotter to the cooler areas of the fluid. The term natural convection covers all flows due to density changes within the fluid, including density changes due to a temperature gradient [31]. Thus, natural convection can be induced by gravitational and mass forces that are acting on a fluid as well as the presence of different phases with different densities within a fluid [31].

It is worth noting that natural convection includes only flows where the flow is not driven by an external mechanical source. In the opposite case, such flows are classified as forced convection flows [27]. Usually, buoyancy forces can be neglected in case of forced convection within a fluid, since the flow is driven by other forces originating from an external source, such as a pump. Other examples of forced convection include heating and cooling systems with a ventilator.

Figure 1.1 shows a typical example of natural convection. A hot, cuboid object generates a flow around it by heating the surrounding air which is driven upwards by the buoyancy force.

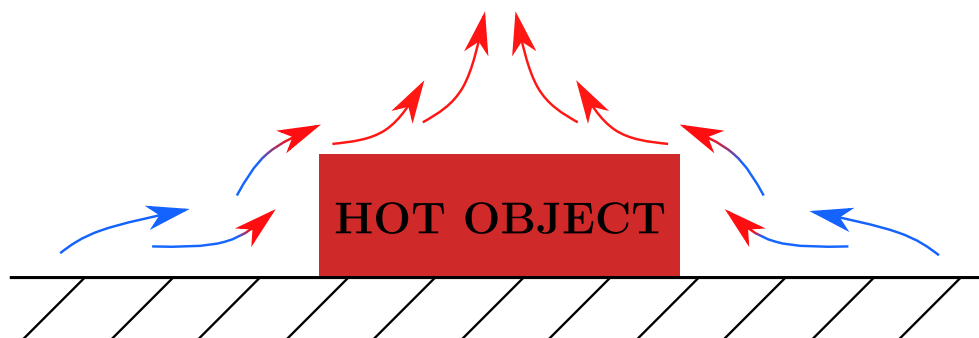


FIGURE 1.1 – Natural convection, air flow around a hot object.

Once again, the density change of the air is responsible for the resulting flow. This is the principle by which most conventional heaters operate.

1.2 Hydrodynamic Stability

Per definition, flow patterns that are unable to sustain themselves against small perturbations are deemed unstable [9]. The term *hydrodynamic stability* covers the study of the stability and instability of motions of fluids [13]. The starting point of studying the stability of a laminar flow is a *basic flow*, which is defined by the steady or unsteady fields of velocity $\mathbf{u}_0(\mathbf{x}, t)$, pressure $p_0(\mathbf{x}, t)$, and temperature $\theta_0(\mathbf{x}, t)$ which need to satisfy the equations of motion and the boundary conditions of the problem [14]. The basic flow is Liapunov-stable if for any $\epsilon > 0$ there exists a number $\delta > 0$ such that if

$$\|\mathbf{u}(\mathbf{x}, 0) - \mathbf{u}_0(\mathbf{x}, 0)\|, \|p(\mathbf{x}, 0) - p_0(\mathbf{x}, 0)\|, \|\theta(\mathbf{x}, 0) - \theta_0(\mathbf{x}, 0)\| < \delta. \quad (1.1)$$

then

$$\|\mathbf{u}(\mathbf{x}, t) - \mathbf{u}_0(\mathbf{x}, t)\|, \|p(\mathbf{x}, t) - p_0(\mathbf{x}, t)\|, \|\theta(\mathbf{x}, t) - \theta_0(\mathbf{x}, t)\| < \epsilon, \forall t \geq 0, \quad (1.2)$$

where $\mathbf{u}(\mathbf{x}, t)$, $p(\mathbf{x}, t)$ and $\theta(\mathbf{x}, t)$ are the velocity, pressure and temperature fields that satisfy the equations of motions and the boundary conditions. If we consider a two dimensional flow with $\mathbf{u}(x, y)$ which is invariant in the z -axis, it is possible to determine the onset of instability as of which the flow is no longer two dimensional by decomposing the flow velocity as

$$\mathbf{u}(x, y, z, t) = \mathbf{u}_0(x, y) + \mathbf{u}'(x, y, z, t), \quad (1.3)$$

where \mathbf{u}_0 is a basic flow and \mathbf{u}' a three dimensional, time dependent perturbation. Moreover, the equations of motion can be linearised if we assume that \mathbf{u}' is sufficiently small, with $\|\mathbf{u}'\|_{L_2} \ll 1$, where the L_2 norm is computed using the following formula

$$\|\mathbf{x}\|_{L^2} = \left(\int_{\Omega} |\mathbf{x}|^2 \, d\Omega \right)^{\frac{1}{2}}, \quad (1.4)$$

with $\Omega \in \mathbb{R}^2$ denoting the domain space. Then, a normal mode ansatz can be introduced for the perturbation such that

$$\mathbf{u}'(x, y, z, t) = \sum \hat{\mathbf{u}}(x, y) e^{\lambda t + ikz}, \quad (1.5)$$

where λ is the complex growth rate, k a wavenumber and $\hat{\mathbf{u}}$ is determined from the linearised system equations. The real part of λ defines if the system is either

- **linearly asymptotically stable** if $\forall_i \Re(\lambda_i) < 0$ or,
- **linearly stable** if $\forall_i \Re(\lambda_i) \leq 0$ or
- **linearly unstable** if $\exists_i \Re(\lambda_i) > 0$.

The same process can be repeated with the other flow variables, p and θ .

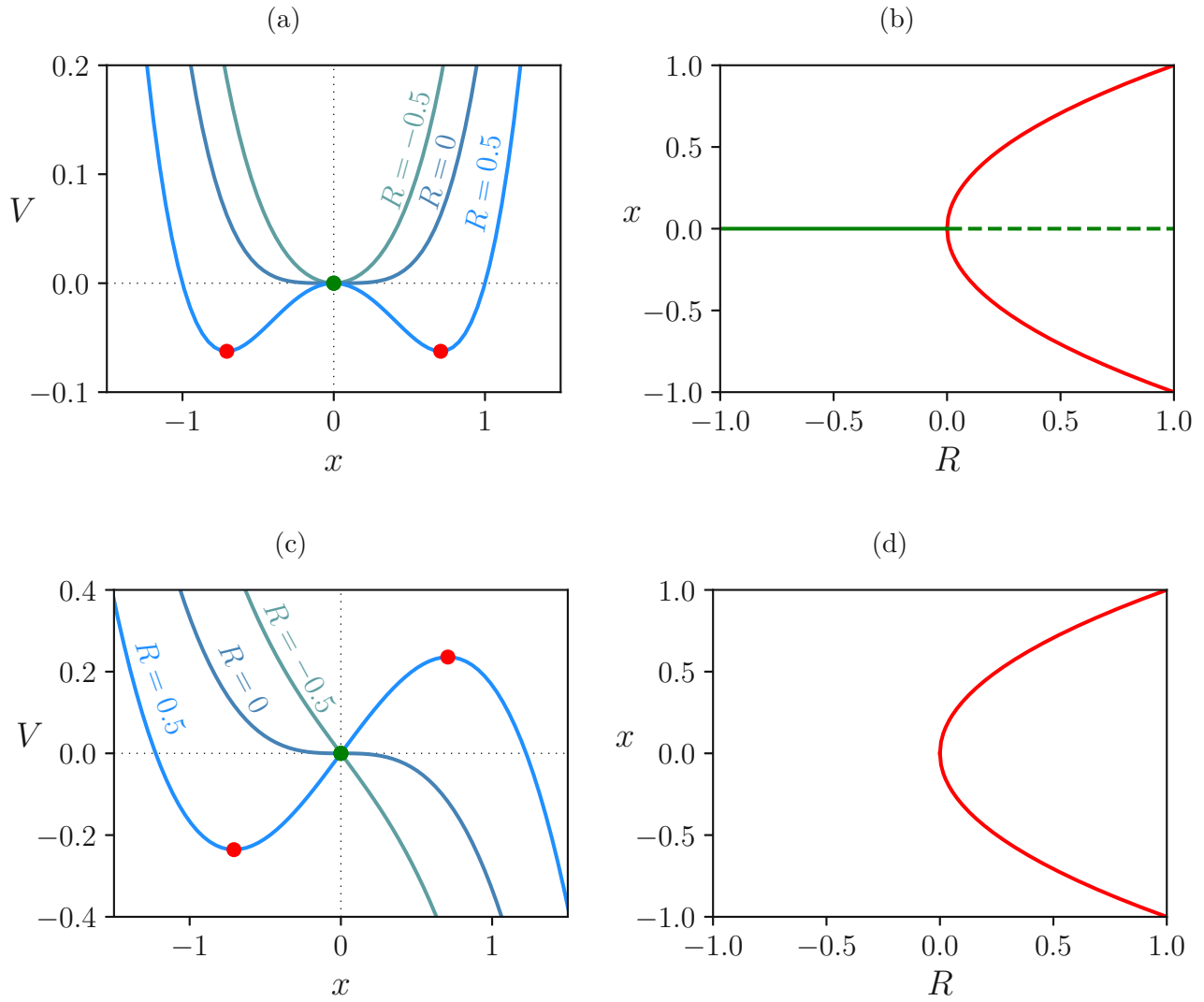


FIGURE 1.2 – (a), (b) Pitchfork and (c), (d) saddle–node bifurcation with $R = -0.5, 0, 0.5$.

Instabilities lead often to bifurcations, which are defined as the branching of the solution from a known solution branch to a new solution, which is continuously connected to the old solution [28]. Let us consider the potential equation of

$$V(x) = -R\frac{x^2}{2} + \frac{x^4}{4}, \tag{1.6}$$

where R is a control parameter. Figures 1.2a, 1.2b show the potential equation plotted at the values of $R = -0.5, 0, 0.5$ on the left and the bifurcation plot on the right. For values of $R < 0$ we see a unique minimum at $x = 0$ and for $R > 0$, two minima exist. Thus, by increasing the control parameter R , the solution branches into two solutions. This bifurcation is defined as *pitchfork bifurcation* [28]. Other types of bifurcations are possible, such as the *saddle–node bifurcation* in Figures 1.2c, 1.2d, which annihilates two solutions with a change of the control parameter [28]. In this particular example the potential equation

$$V(x) = Rx - \frac{x^3}{3}, \tag{1.7}$$

has two local extrema for $R > 0$ and one saddle point for $R = 0$, which is represented by the

green point on the potential equation in Figure 1.2c. As for $R < 0$, there are no extrema and therefore the bifurcation plot shows solutions only for $R \geq 0$ as seen in Figure 1.2d.

A classical example flow where hydrodynamic stability has been studied extensively are Rayleigh–Bénard flows. They serve as a prototype for studying instabilities induced by thermal convection in related flows [14]. In such flows, the fluid is heated from below and causes a horizontal density difference in the fluid, which induces a flow. One of the first studies in such flows was conducted by Bénard [7], who experimentally discovered the formation of cells on the surface of the fluid, now known as Bénard cells. As the initially resting fluid is heated from below, the Bénard cells appear on its surface after convection starts in the fluid, which is triggered after a certain temperature of the bottom boundary is surpassed. Figure 1.3 shows an experiment from Koschmieder & Pallas [26] where the Bénard cells are visible under an air surface. Later, Rayleigh [34] considered an initially resting fluid between two infinite planes with a constant temperature and tried to determine analytically the temperature difference of the plates as of which a flow could be induced. The control parameter of this problem, which can be used to determine the stability boundary of the flow, is the Rayleigh number, which is equal to

$$\text{Ra} = \frac{L^3 \beta g \Delta T}{\nu \kappa}, \quad (1.8)$$

where L is the characteristic length scale of the flow, g the gravitational acceleration, ΔT the temperature difference between the planes, ν the kinematic viscosity and κ the thermal diffusivity. Rayleigh considered a steady two dimensional basic flow which is invariant in the third direction. In case of two free boundaries, Rayleigh determined analytically that the onset of instability occurs as of the critical value of

$$\text{Ra}_c = \frac{27\pi}{4} \approx 657.51. \quad (1.9)$$

As of this number, the symmetry of the two dimensional flow is broken and the flow transcends into a three dimensional flow. The critical wavenumber is given by

$$k_c = \frac{\pi}{\sqrt{2}} \approx 2.221. \quad (1.10)$$

Drazin [13] considered different boundary conditions for the infinite planes, which they modelled either as free or rigid, and placed the critical Rayleigh number with two rigid boundaries at $\text{Ra}_c = 1708$, with $k_c = 3.117$. Rayleigh–Bénard flows can also be used to describe large scale flows in the atmosphere, oceans, volcanoes or avalanches, due to the dependence of the Rayleigh number on L^3 [11].

1.3 Buoyancy Driven Flows in Cavities

Buoyancy driven flows are induced by a density difference within the fluid in a gravitational field [11]. Previously, we covered Rayleigh–Bénard flows, where the flow is driven due to a horizontal density difference which is caused by a heating from below. Many studies considered the effect of side walls on the stability of Rayleigh–Bénard flows. Studies such as those of Charlson & Sani [10] and Davis [12] showed how the side walls can affect the flow stability, with the former considering a flow inside a cylinder and the later a flow inside rectangular boxes. Other studies have considered enclosures with vertical heated walls. Unlike Rayleigh–Bénard flows, there are

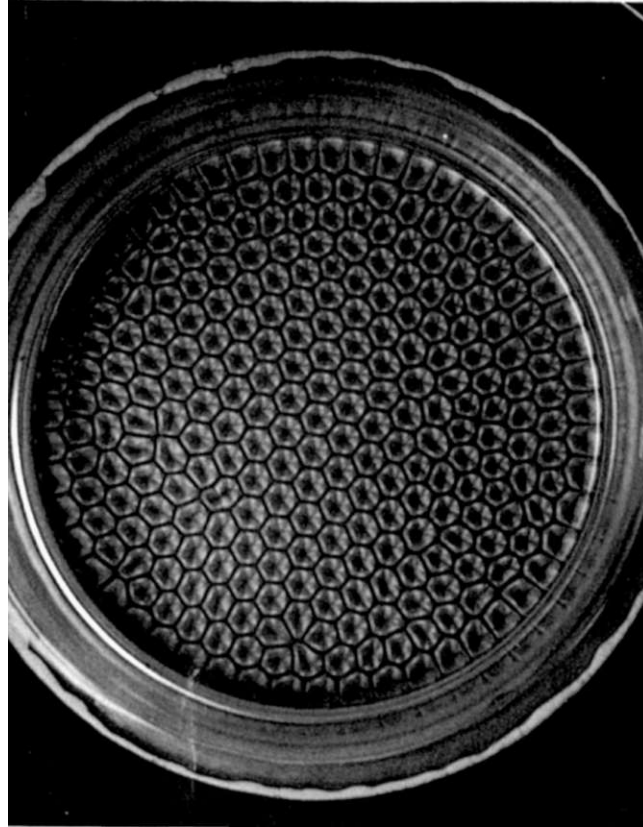


FIGURE 1.3 – Bénard cells under an air surface from Koschmieder & Pallas [26].

no resting states in this configuration [14]. Studies that investigated the flow stability in such flows include Hart [20], Janssen & Henkes [25] and Gelfgat & Tanasawa [18] to mention a few.

Both aforementioned cases with horizontal or vertical heated walls are shown in Figure 1.4. The cavities in the figure are assumed to be two dimensional and infinitely extended in the third dimension. An experimental setup with this configuration can be realised by considering the square cross section of a slab with a sufficiently larger length compared to the edge length of the square. The flow is driven by the density difference which is caused by the temperature gradient $\Delta T = T_H - T_C$ within the flow, since the density of the fluid decreases near the hot wall and increases near the cold wall. This density difference results into a flow circulation within the cavity. According to Chassignet *et al.* [11], a useful term to describe buoyancy driven flows is the reduced gravity which is defined as

$$\mathbf{g}' = \mathbf{g} \frac{\Delta\rho}{\rho}, \quad (1.11)$$

where $\Delta\rho$ is the local density difference and ρ a representative density. The reduced gravity is essentially the local acceleration of the flow which is caused by a local density difference. With heating from below as in Figure 1.4a, other circulations are also possible, with more than one roll and there is also a motionless state that is realisable. Other studies also investigated the effect of an inclination in a two dimensional plane on the flow stability in differentially heated cavities such as Hart [21] and Hiroyuki *et al.* [22]. The setup in Figure 1.4 is a simplified version of the subject of this thesis in which the cavity is tilted in a two dimensional space, similarly to the two aforementioned studies.

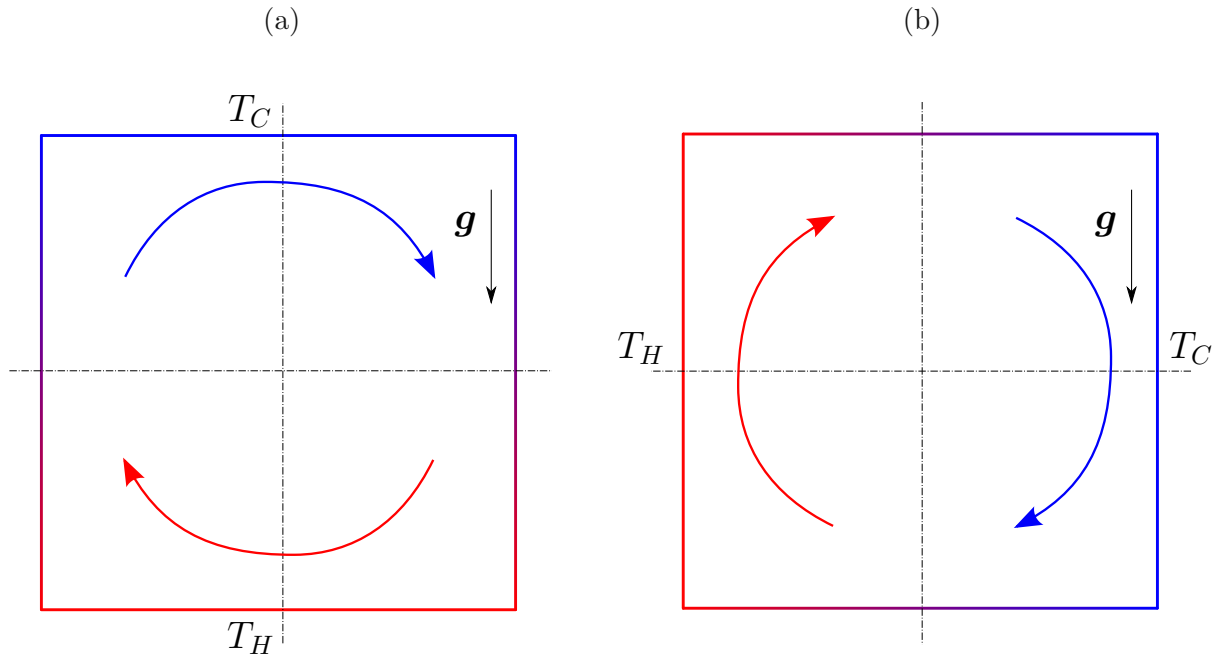


FIGURE 1.4 – Two differentially heated two dimensional square cavities with a buoyancy driven flow, (a) with horizontal heated walls and (b) with vertical heated walls.

1.4 Flow State Multiplicity

The non-dimensional Navier–Stokes equations can be defined as

$$\frac{\partial \mathbf{u}}{\partial t} + (\mathbf{u} \cdot \nabla) \mathbf{u} = -\nabla p + \frac{1}{\text{Re}} \Delta \mathbf{u}. \quad (1.12)$$

The control parameter in this notation is the Reynolds number Re , which is defined as

$$\text{Re} = \frac{uL}{\nu}, \quad (1.13)$$

with u the characteristic flow velocity magnitude, L the characteristic scale length of the flow and ν the kinematic flow viscosity. If $\text{Re} \rightarrow 0$, (1.12) has a unique solution. However by increasing the Reynolds number, multiple flow states can come into existence through saddle–node bifurcations, in a similar manner as in Figure 1.2d.

In the present thesis, the state multiplicity comes into question for the Rayleigh–Bénard flow inside the cavity as shown in Figure 1.4a, as well as inclinations where the hot wall remains on the bottom. Identifying the different steady states was crucial to determine the flow stability, as each state has different stability properties. Steady state multiplicities have also been confirmed in similar convective flows. For instance, Gelfgat *et al.* [17] identified multiple steady states during a flow stability study in cavities with different aspect ratios and vertical heated walls. Similarly, Piller *et al.* [33] showed that the flow inside an inclined channel, which is heated from one side, can have multiple steady states for the same inclination. Albensoeder *et al.* [2] also determined multiple flow states in a two sided lid driven cavity. In this thesis, we use the results of Huelsz & Rechtman [23] and Boullé *et al.* [8] to discuss the multiple steady states that were discovered.

2.1 The Inclined Differentially Heated Cavity

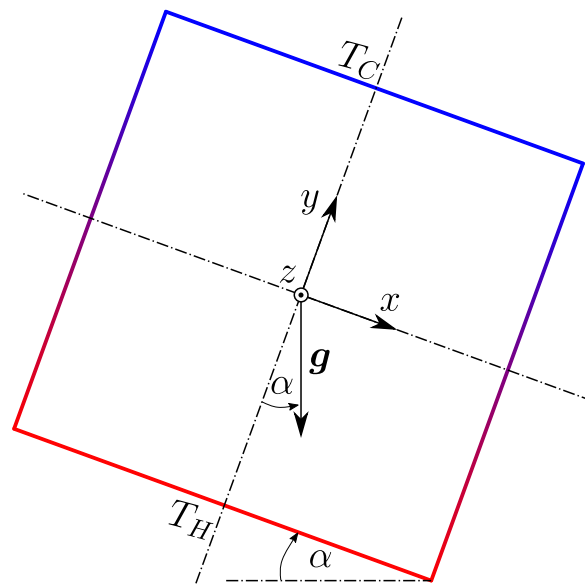


FIGURE 2.1 – Sketch of a differentially heated 2D cavity, with the temperatures T_C and T_H for the cold and hot wall respectively. The cavity is rotated with the angle α .

We consider the case of a differentially heated cavity with a square cross section on the x - y plane and is infinitely extended in the z direction. The origin of the coordinate system is placed in the middle of the square cross section. The top and bottom walls at $y = \pm 0.5$, are cooled and heated uniformly at a constant temperature of T_C and T_H respectively. The remaining lateral vertical walls at $x = \pm 0.5$ are modelled as perfectly conducting throughout the majority of this thesis, apart from Chapter 5, where they are modelled as adiabatic as well.

We also introduce an inclination angle α , which tilts the cavity in a two dimensional plane as shown in Figure 2.1. The inclination angle α represents a positive rotation of the coordinate system around the z -axis. The coordinate system can be transformed by taking the direction of the rotation into consideration which results in the following rotation matrix

$$R(\alpha) = \begin{bmatrix} \cos(\alpha) & -\sin(\alpha) & 0 \\ \sin(\alpha) & \cos(\alpha) & 0 \\ 0 & 0 & 1 \end{bmatrix}. \quad (2.1)$$

2.2 Equations of Fluid Dynamics

The Navier–Stokes equations for a Newtonian fluid, the heat equation and the continuity equation are defined as

$$\rho \left(\frac{\partial}{\partial t} + \mathbf{u} \cdot \nabla \right) \mathbf{u} = -\nabla p + \mu \Delta \mathbf{u} + \mathbf{f}, \quad (2.2a)$$

$$\rho c_p \left(\frac{\partial}{\partial t} + \mathbf{u} \cdot \nabla \right) T = \lambda \Delta T, \quad (2.2b)$$

$$\frac{\partial \rho}{\partial t} + \nabla \cdot (\rho \mathbf{u}) = 0, \quad (2.2c)$$

where ρ is the fluid density, t the time, \mathbf{u} the flow velocity, p the pressure, μ the dynamic viscosity and \mathbf{f} an external forcing vector in (2.2a). In the heat equation in (2.2b), T is the temperature, β the thermal expansion coefficient, \mathbf{g} is the gravity acceleration, c_p the heat capacity and λ the Fourier coefficient. In order to model the buoyancy forces, we use the Oberbeck–Boussinesq approximation by adapting the forcing vector \mathbf{f} in (2.2a). The Oberbeck–Boussinesq approximation ignores density differences that are not dependent on the gravity acceleration \mathbf{g} , such as differences caused by changes in pressure [29]. Despite this fact, the Oberbeck–Boussinesq approximation is accurate in describing buoyancy driven flows, provided that small temperature differences within the fluid are considered. Moreover, the approximation is only valid if the resulting density differences in the fluid are negligible compared to the density of the fluid. Since other density changes are ignored, the fluid is assumed to be incompressible with $\rho = \text{const}$, which modifies the continuity equation in (2.2c). The resulting three equations are

$$\rho \left(\frac{\partial}{\partial t} + \mathbf{u} \cdot \nabla \right) \mathbf{u} = -\nabla p + \mu \Delta \mathbf{u} + \rho \beta T \mathbf{g}, \quad (2.3a)$$

$$\rho c_p \left(\frac{\partial}{\partial t} + \mathbf{u} \cdot \nabla \right) T = \lambda \Delta T, \quad (2.3b)$$

$$\nabla \cdot \mathbf{u} = 0. \quad (2.3c)$$

All equations in (2.3) can be non-dimensionalized by introducing the following non-dimensional scales for the length, time, velocity, pressure and temperature

$$\mathbf{x} = L \mathbf{x}^*, \quad t = \frac{L^2}{\nu} t^*, \quad \mathbf{u} = \frac{\nu}{L} \mathbf{u}^*, \quad p = \frac{\rho \nu^2}{L^2} p^*, \quad T = \Delta T \theta^*,$$

which transforms them to

$$\left(\frac{\partial}{\partial t^*} + \mathbf{u}^* \cdot \nabla_* \right) \mathbf{u}^* = -\nabla_* p^* + \Delta_* \mathbf{u}^* + \frac{\text{Ra}}{\text{Pr}} \theta^* \mathbf{e}_g, \quad (2.4a)$$

$$\left(\frac{\partial}{\partial t^*} + \mathbf{u}^* \cdot \nabla_* \right) \theta^* = \frac{1}{\text{Pr}} \Delta_* \theta^*, \quad (2.4b)$$

$$\nabla_* \cdot \mathbf{u}^* = 0, \quad (2.4c)$$

where the dimensionless Rayleigh and Prandtl numbers are defined as

$$\text{Ra} = \frac{L^3 \beta g \Delta T}{\nu \kappa}, \quad \text{Pr} = \frac{\nu}{\kappa}, \quad (2.5)$$

and $\kappa = \lambda / \rho c_p$ is the thermal diffusivity. Since the fluid in cavity is always air in this thesis, we can fix the Prandtl number to $\text{Pr} = 0.71$. For the sake of readability, the asterisk * symbol will not be used as of this point when the equations in (2.4) are referenced. Thus, all resulting equations from (2.4) are non-dimensional. The rotation of the coordinate system is applied to the governing equations by multiplying the rotation matrix with the unit gravity acceleration vector \mathbf{e}_0 in order to obtain

$$\mathbf{e}_g = R(\alpha) \cdot \mathbf{e}_0 = \begin{bmatrix} \cos(\alpha) & -\sin(\alpha) & 0 \\ \sin(\alpha) & \cos(\alpha) & 0 \\ 0 & 0 & 1 \end{bmatrix} \cdot \begin{bmatrix} 0 \\ -1 \\ 0 \end{bmatrix} = \begin{bmatrix} \sin(\alpha) \\ -\cos(\alpha) \\ 0 \end{bmatrix}. \quad (2.6)$$

2.3 Boundary Conditions

The temperatures on the hot and cold walls are:

$$\begin{aligned} \theta(x, y = -0.5) &= \theta_H = 0.5, \\ \theta(x, y = 0.5) &= \theta_C = -0.5. \end{aligned} \quad (2.7)$$

In case the lateral walls are perfectly conducting, the lateral wall temperature decreases linearly from θ_H to θ_C with

$$\theta(x = \pm 0.5, y) = -y. \quad (2.8)$$

With adiabatic lateral walls, the heat exchange between the fluid and the surrounding environment is fixed to zero, such that

$$\nabla \theta \cdot \mathbf{n} = 0, \quad (2.9)$$

where \mathbf{n} is an outward unit normal vector to the lateral walls. The velocity on all walls is modelled with a no-slip boundary condition and is zero on the whole domain at the start of each simulation

$$\mathbf{u}(x, y = \pm 0.5) = \mathbf{0}, \quad \mathbf{u}(t = 0) = \mathbf{0}. \quad (2.10)$$

2.4 Basic Flow

The variables of the flow velocity \mathbf{u} , pressure p and temperature θ are combined into a single flow variable $\mathbf{q} = (\mathbf{u}, \theta, p)^T$. We define the *basic flow* as $\mathbf{q}_0 = (\mathbf{u}_0, \theta_0, p_0)^T$ such that it satisfies the governing equations in the x - y plane without the time dependent terms in (2.4), as well as the boundary conditions in Section 2.3. Moreover, we assume that the basic flow is time independent and two dimensional with $\mathbf{q}_0 = \mathbf{q}_0(x, y)$.

2.5 Linear Stability

Next, \mathbf{q} can be decomposed into the basic flow, $\mathbf{q}_0(x, y)$ and an infinitesimal three dimensional, time dependent perturbation flow $\mathbf{q}'(x, y, z, t)$, with $\|\mathbf{q}'\|_{L^2} \ll 1$ such that

$$\mathbf{q}(x, y, z, t) = \mathbf{q}_0(x, y) + \mathbf{q}'(x, y, z, t). \quad (2.11)$$

Due to homogeneity of the problem in the z -axis and time, a normal mode ansatz can be applied in the z direction. This leads to

$$\mathbf{q}'(x, y, z, t) = \sum \hat{\mathbf{q}}_i(x, y) e^{\lambda t + ikz} + \text{c.c.}, \quad (2.12)$$

where $\hat{\mathbf{q}}_i \in \mathbb{C}$ represents the complex modes, $\lambda \in \mathbb{C}$ the complex growth rates, $k \in \mathbb{R}$ the wavenumber and c.c. is a complex conjugate of the leading sum term on the right hand side, which is added in order to force a real solution for \mathbf{q}' . Consequently, the wavenumber is an additional parameter to the problem. The complex growth rates λ can be written as $\lambda = \sigma + i\omega$, where σ is the growth rate of the mode and ω its oscillation frequency. Any mode with $\sigma > 0$ represents an unstable mode with a growing perturbation and modes with $\sigma < 0$ represent stable modes where the perturbation diminishes over time.

2.6 Dynamical System Formulation

It is beneficial to express (2.4) with a dynamical system formulation to simplify the equations. Leaving only the time dependent terms on the left hand side, and by using the flow vector \mathbf{q} which was defined in the previous section, we obtain the following system of equations

$$\frac{\partial}{\partial t} \mathcal{B} \cdot \mathbf{q} = \mathbf{F}(\mathbf{q}). \quad (2.13)$$

$\mathbf{F}(\mathbf{q})$ contains all the remaining time independent terms in the right hand side and is defined as

$$\mathbf{F}(\mathbf{q}) = \begin{bmatrix} -\mathbf{u} \cdot \nabla \mathbf{u} - \nabla p + \Delta \mathbf{u} + \frac{\text{Ra}}{\text{Pr}} \theta \mathbf{e}_g \\ -\mathbf{u} \cdot \nabla T + \frac{1}{\text{Pr}} \Delta \theta \\ \nabla \cdot \mathbf{u} \end{bmatrix}. \quad (2.14)$$

\mathcal{B} is a symmetric matrix operator that matches the time dependent terms of each equation with the rows of (2.14) and is equal to

$$\mathcal{B} = \begin{bmatrix} 1 & 0 & 0 & 0 & 0 \\ & 1 & 0 & 0 & 0 \\ & & 1 & 0 & 0 \\ & & & 1 & 0 \\ & & & & 0 \end{bmatrix}. \quad (2.15)$$

The basic flow is the steady state solution of the system in (2.13) when $\mathbf{q} = \mathbf{q}_0$ which can be expressed by

$$\mathbf{F}(\mathbf{q}_0) = 0. \quad (2.16)$$

Inserting the above decomposition of $\mathbf{q} = \mathbf{q}_0 + \mathbf{q}'$ in (2.13) and applying a Taylor expansion in $\mathbf{F}(\mathbf{q}_0 + \mathbf{q}')$ results in

$$\begin{aligned} \frac{\partial}{\partial t} \mathcal{B} \cdot \mathbf{q}' &= \mathbf{F}(\mathbf{q}_0 + \mathbf{q}') \\ &= \mathbf{F}(\mathbf{q}_0) + \frac{\partial \mathbf{F}(\mathbf{q}_0)}{\partial \mathbf{q}_0} \cdot \mathbf{q}' + O(\|\mathbf{q}'\|_{L^2}^2) \\ &= \underbrace{\mathbf{F}(\mathbf{q}_0)}_{=0} + \mathcal{A}_p(\mathbf{q}_0) \cdot \mathbf{q}' + O(\|\mathbf{q}'\|_{L^2}^2). \end{aligned}$$

$\mathbf{F}(\mathbf{q}_0)$ vanishes as a consequence of (2.16) and $\mathcal{A}_p(\mathbf{q}_0) \cdot \mathbf{q}'$ is obtained by linearising the equations in (2.4)

$$\mathcal{A}_p(\mathbf{q}_0) \cdot \mathbf{q}' = \begin{bmatrix} \left(\frac{\partial}{\partial t} + \mathbf{u}_0 \cdot \nabla \right) \mathbf{u}' + \mathbf{u}' \cdot \nabla \mathbf{u}_0 - \nabla p' + \Delta \mathbf{u}' + \frac{\text{Ra}}{\text{Pr}} \theta' \mathbf{e}_g \\ \left(\frac{\partial}{\partial t} + \mathbf{u}_0 \cdot \nabla \right) \theta' - \mathbf{u}' \cdot \nabla \theta_0 + \frac{1}{\text{Pr}} \Delta \theta' \\ \nabla \cdot \mathbf{u}' \end{bmatrix}. \quad (2.17)$$

All higher order terms in $O(\|\mathbf{q}'\|_{L^2}^2)$ can be neglected due to $\|\mathbf{q}'\|_{L^2} \ll 1$ which leads to a linearised problem with

$$\frac{\partial}{\partial t} \mathcal{B} \cdot \mathbf{q}' = \mathcal{A}_p(\mathbf{q}_0) \cdot \mathbf{q}'. \quad (2.18)$$

Applying the normal mode ansatz from (2.12) to \mathbf{q}' leads to the generalized eigenvalue problem of

$$\lambda \mathcal{B} \cdot \hat{\mathbf{q}}_i = \mathcal{A}(\mathbf{q}_0) \cdot \hat{\mathbf{q}}_i, \quad (2.19)$$

where $\mathcal{A}(\mathbf{q}_0)$ is a complex matrix due to the complex ansatz in (2.12). In conclusion, the problem is decomposed into two systems of equations. First, the solution of the basic flow equation in (2.16) enables obtaining the basic flow \mathbf{q}_0 and second, solving the eigenvalue problem in (2.19) delivers the eigenmodes $\hat{\mathbf{q}}_i$. We are interested in obtaining the neutral eigenmodes with $\sigma = 0$, where the perturbation neither grows nor decays. The conventional way to achieve this, is to solve the eigenvalue problem for different values of the Rayleigh number and the wavenumber until the neutral modes with the neutral values of the Rayleigh number Ra_N have been determined. From a numerical point of view, the eigenvalue problem in (2.19) is the most expensive operation between the two systems of equations and if treated conventionally, it has to be solved for multiple values of the Rayleigh number and the wavenumber which is inefficient. Moreover, we are interested in obtaining the minimum neutral Rayleigh number for each inclination angle depending the wavenumber, which further increases the computational effort. The numerical solution of these two systems of equations is the main topic of Chapter 3.

2.7 A Posteriori Energy Analysis

In order to have an insight into the instability mechanism, it is beneficial to examine the energy transfer between the basic state and the perturbation. The perturbation kinetic energy can be defined as

$$E' = \frac{1}{2} \int_V \mathbf{u}'^2 \, dV, \quad (2.20)$$

where V is the volume occupied by the fluid, defined by the square cross section of the cavity and one wavelength in the z direction measuring $z_k = 2\pi/k$. We are interested in investigating the rate of change of E' which is given by the Orr–Reynolds equation as

$$\partial_t E' = \partial_t \left[\frac{1}{2} \int_V \mathbf{u}'^2 \, dV \right] = \int_V \mathbf{u}' \cdot \partial_t \mathbf{u}' \, dV. \quad (2.21)$$

Neutral states, where the flow crosses from a stable to an unstable state are characterised by $\partial_t E' = 0$ over one period of wavelength due to periodicity. The term $\partial_t \mathbf{u}'$ can be equated to

the first row of the linearised equations in (2.17) such that

$$-\int_V \mathbf{u}' \cdot (\mathbf{u}' \cdot \nabla) \mathbf{u}_0 \, dV + \int_V \frac{\text{Ra}}{\text{Pr}} T' \mathbf{u}' \cdot \mathbf{e}_g \, dV + \int_V \mathbf{u}' \cdot \Delta \mathbf{u}' \, dV = 0. \quad (2.22)$$

The dissipative term can be further simplified to

$$D = \int_V \mathbf{u}' \cdot \Delta \mathbf{u}' \, dV = \int_V \nabla \mathbf{u}' : \nabla \mathbf{u}' \, dV, \quad (2.23)$$

through integration by parts. Consequently, (2.22) can be rewritten as

$$I_t + B_t - D = 0, \quad (2.24)$$

where I_t is the inertial production term, B_t the buoyancy production term and D the dissipation term. Finally, since $D > 0$ the equation above can be normalised such that

$$I + B = 1, \quad I = \frac{I_t}{D}, \quad B = \frac{B_t}{D}. \quad (2.25)$$

As such, I is the normalised inertia production term and B is the normalised buoyancy term and are defined as

$$I = -\frac{1}{D} \int_V \mathbf{u}' \cdot (\mathbf{u}' \cdot \nabla) \mathbf{u}_0 \, dV, \quad (2.26)$$

$$B = \frac{1}{D} \int_V \frac{\text{Ra}}{\text{Pr}} T' \mathbf{u}' \cdot \mathbf{e}_g \, dV. \quad (2.27)$$

The instability mechanism can be identified by comparing these two parameters with each other. If $I > B$, then the instability is driven by the inertial forces and on the contrary, if $I < B$, by the buoyancy. The inertial production term can be further decomposed into four components as done in [3] with

$$I_1 = -\frac{1}{D} \int_V \mathbf{u}'_{\perp} \cdot (\mathbf{u}'_{\perp} \cdot \nabla) \mathbf{u}_0 \, dV, \quad (2.28)$$

$$I_2 = -\frac{1}{D} \int_V \mathbf{u}'_{\parallel} \cdot (\mathbf{u}'_{\perp} \cdot \nabla) \mathbf{u}_0 \, dV, \quad (2.29)$$

$$I_3 = -\frac{1}{D} \int_V \mathbf{u}'_{\perp} \cdot (\mathbf{u}'_{\parallel} \cdot \nabla) \mathbf{u}_0 \, dV, \quad (2.30)$$

$$I_4 = -\frac{1}{D} \int_V \mathbf{u}'_{\parallel} \cdot (\mathbf{u}'_{\parallel} \cdot \nabla) \mathbf{u}_0 \, dV, \quad (2.31)$$

in which the perturbation velocity \mathbf{u}' is decomposed into a component tangential and perpendicular to the basic flow velocity \mathbf{u}_0 with

$$\mathbf{u}'_{\parallel} = \frac{(\mathbf{u}_0 \cdot \mathbf{u}') \mathbf{u}_0}{\|\mathbf{u}_0\|^2}, \quad \text{and} \quad \mathbf{u}'_{\perp} = \mathbf{u}' - \mathbf{u}'_{\parallel}. \quad (2.32)$$

The summation of the components I_i is equal to I itself with

$$I = \sum_{i=1}^4 I_i. \quad (2.33)$$

This decomposition is useful in identifying whether the inertial production is due to lift up with $I_2 \neq 0$ or a flow deceleration if $I_4 \neq 0$. The contribution of I and B to the instability mechanism will be discussed in detail in Chapter 6 below.

Numerical Methods

In this chapter, the numerical methods that were used in this thesis will be presented. The code for all numerical methods in this thesis was written in Python 3. With the exception of the neutral curve tracking method in Section 3.10, all methods in this chapter were already implemented in the house code that was used during this thesis.

3.1 Weak Formulation

First, we start by introducing the weak or variational form of the governing equations in (2.4), since this formulation is required by the numerical methods that were used in this thesis. A partial differential equation (PDE) written in a weak formulation is mathematically equivalent to its strong form and thus solutions derived from either form are also equivalent to each other [32]. PDEs written in a strong formulation have continuity and differentiability requirements imposed on their solutions. The weak formulation does not impose such requirements on the solution, but instead imposes them on approximation functions, also known as test functions. Therefore, the advantage of using a weak form lies with the test functions, because they are generally lesser degree polynomials, which lower the computational effort. In order to derive the weak form of (2.4), the equations are multiplied by the test functions $\mathbf{u}_V, \theta_V, q_V$ and subsequently integrated over the domain space $\Omega \in \mathbb{R}^2$. Moreover, they inherit the boundary conditions of their respective variables. Adding all equations leads to

$$\begin{aligned} \int_{\Omega} \left(\frac{\partial \mathbf{u}}{\partial t} + \mathbf{u} \cdot \nabla \mathbf{u} \right) \cdot \mathbf{u}_V \, d\Omega + \int_{\Omega} \nabla p \cdot \mathbf{u}_V \, d\Omega - \int_{\Omega} \Delta \mathbf{u} \cdot \mathbf{u}_V \, d\Omega - \frac{\text{Ra}}{\text{Pr}} \int_{\Omega} \theta \mathbf{e}_g \cdot \mathbf{u}_V \, d\Omega \\ + \int_{\Omega} \theta_V \left(\frac{\partial \theta}{\partial t} + \mathbf{u} \cdot \nabla \theta \right) \, d\Omega - \frac{1}{\text{Pr}} \int_{\Omega} \theta_V \Delta \theta \, d\Omega \\ + \int_{\Omega} (\nabla \cdot \mathbf{u}) q_V \, d\Omega = 0. \end{aligned} \quad (3.1)$$

One then integrates by parts the pressure term, dissipative term and the Laplacian of the temperature to obtain

$$\int_{\Omega} \nabla p \cdot \mathbf{u}_V \, d\Omega = \int_{\Omega} p \nabla \cdot \mathbf{u}_V \, d\Omega - \underbrace{\int_{\Gamma} p \mathbf{u}_V \cdot \mathbf{n} \, d\Gamma}_{=0}, \quad (3.2a)$$

$$\int_{\Omega} \Delta \mathbf{u} \cdot \mathbf{u}_V \, d\Omega = \int_{\Omega} \nabla \mathbf{u} : \nabla \mathbf{u}_V \, d\Omega - \underbrace{\int_{\Gamma} \nabla \mathbf{u} (\mathbf{u}_V \cdot \mathbf{n}) \, d\Gamma}_{=0}, \quad (3.2b)$$

$$\int_{\Omega} \theta_V \Delta \theta \, d\Omega = \int_{\Omega} \nabla \theta \cdot \nabla \theta_V \, d\Omega - \underbrace{\int_{\Gamma} (\nabla \theta \cdot \mathbf{n}) \theta_V \, d\Gamma}_{=0}, \quad (3.2c)$$

where $\Gamma = \partial\Omega$ is the domain space on the boundaries. The above integration by parts leads to the derivation of the known test functions, while also lowering the derivative order of the unknown variables. Moreover, the first two boundary terms in (3.2a) and (3.2b) are trivial due to the Dirichlet boundary conditions that are imposed on the velocity on \mathbf{u}_V . In (3.2c), the test function θ_V is trivial on the boundary if the lateral walls are adiabatic. If we consider perfectly conducting lateral walls, the term $\nabla \theta \cdot \mathbf{n}$ becomes trivial instead. Finally, the above terms can be reinserted in (3.1) to obtain

$$\begin{aligned} \int_{\Omega} \left(\frac{\partial \mathbf{u}}{\partial t} + \mathbf{u} \cdot \nabla \mathbf{u} \right) \cdot \mathbf{u}_V \, d\Omega + \int_{\Omega} p \nabla \cdot \mathbf{u}_V \, d\Omega - \int_{\Omega} \nabla \mathbf{u} : \nabla \mathbf{u}_V \, d\Omega - \frac{\text{Ra}}{\text{Pr}} \int_{\Omega} \theta \mathbf{u}_V \cdot \mathbf{e}_g \, d\Omega \\ + \int_{\Omega} \theta_V \left(\frac{\partial \theta}{\partial t} + \mathbf{u} \cdot \nabla \theta \right) \, d\Omega - \frac{1}{\text{Pr}} \int_{\Omega} \nabla \theta \cdot \nabla \theta_V \, d\Omega \\ + \int_{\Omega} (\nabla \cdot \mathbf{u}) q_V \, d\Omega = 0. \end{aligned} \quad (3.3)$$

3.2 Python Packages

Before we discuss the exact numerical methods that were used in this thesis, this section briefly describes the most important Python packages that were employed in the coding process.

FEniCS is the main package employed in the code. It is written in Python and C++ that enables the translation of scientific problems into finite element code [4]. In the scope of this thesis, it is used for computing the basic flow and to compute any derivatives in tasks such as the computation of the energy budget. FEniCS is able to solve partial differential equations (PDE) written in their variational form, such as the non-linear system equation in (3.3).

`scipy` contains a multitude of algorithms in the areas of optimization, integration, interpolation and others [36]. The main purpose of `scipy` in the code is to solve the eigenvalue problem in (2.19), using its builtin `eigs` function.

`numpy` offers a range of tools such as handling of large multidimensional arrays and useful mathematical functions [19]. It is mainly used in the code for the purpose of indexing and sorting data in arrays, as well as for polynomial fitting in tracking the minimum of the neutral curve in Section 3.10.

`matplotlib` provides an array of functions for visualizing data using Python [24]. The majority of the plots in this thesis were created with the help of this library.

3.3 Discretisation

Using the FEniCS library, the velocity and the pressure are discretised using quadratic Taylor-Hood elements \mathbb{P}^2 , for the velocity and linear \mathbb{P}^1 elements for the pressure. This is done in order to satisfy the Ladyzhenskaya–Babuška–Brezzi (LBB) condition [15]. The temperature is discretised using continuous piecewise quadratic polynomials. Since only steady states are considered, time is not discretised. The mesh is also generated with FEniCS, initially with

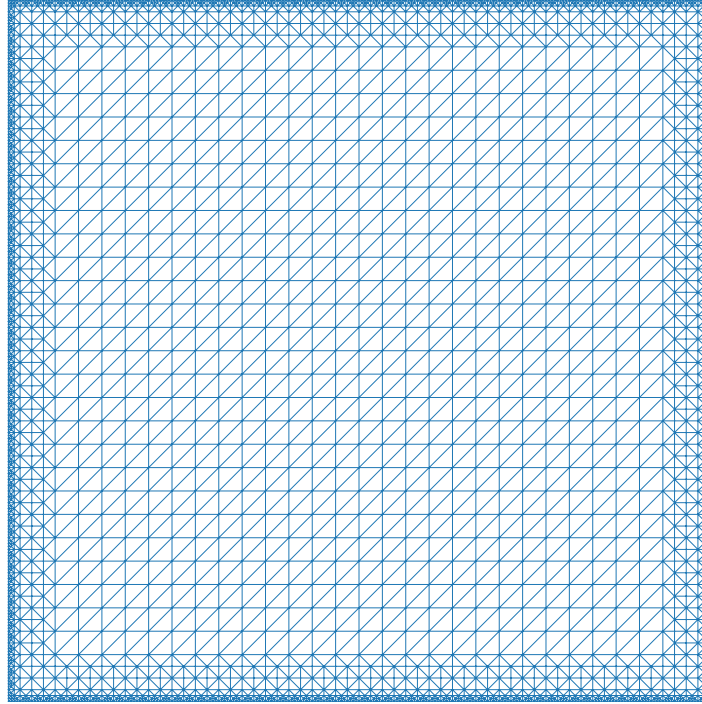


FIGURE 3.1 – Cavity mesh with 6136 triangular elements, refined on the boundaries.

30 triangular elements on each side of the cavity. Three further refinements occur at a 0.05, 0.01 and 0.005 distance from the walls, which results in a mesh with 6136 elements. The two dimensional mesh is shown in Figure 3.1 below.

3.4 Basic Flow

The basic flow is obtained mathematically using Equation (2.16). The non linear problem is solved using Newton's method with the `solve` function of FEniCS. A single iteration step of Newton's method for this particular equation can be written as

$$\nabla \mathbf{F}(\mathbf{q}_0^n) \cdot \Delta \mathbf{q}_0 = -\mathbf{F}(\mathbf{q}_0^n), \quad (3.4a)$$

$$\mathbf{q}_0^{n+1} = \mathbf{q}_0^n + \Delta \mathbf{q}_0^n, \quad (3.4b)$$

where \mathbf{q}_0^n is the basic flow on a specific iteration iteration step n and $\nabla \mathbf{F}(\mathbf{q}_0^n)$ the Jacobian of \mathbf{F} evaluated at \mathbf{q}_0^n . On each iteration step, $\Delta \mathbf{q}_0^n$ is computed by solving the linear system in (3.4). The algorithm requires an initial guess for \mathbf{q}_0^n and continues iterating until convergence within a given tolerance has been achieved. The absolute or relative norm of the increment are required to be lower than a tolerance $\epsilon = 10^{-7}$ such that

$$\|\Delta \mathbf{q}_0^n\|_{L^2} < \epsilon \vee \frac{\|\Delta \mathbf{q}_0^n\|_{L^2}}{\|\Delta \mathbf{q}_0^0\|_{L^2}} < \epsilon. \quad (3.5)$$

The chosen solver for Newton's method is MUMPS which stands for Multifrontal Massively Parallel Solver. Its starting point is a general matrix inversion problem $\mathcal{A}\mathbf{x} = \mathbf{b}$. The matrix

that needs to be inverted, \mathcal{A} , can be decomposed into a product of a lower triangular matrix \mathcal{L} and an upper triangular matrix \mathcal{U} such that

$$\mathcal{A} = \mathcal{L} \cdot \mathcal{U}. \quad (3.6)$$

This decomposition reduces the computational effort due to the shape of \mathcal{L} and \mathcal{U} and is executed once every iteration step. The reader can refer to [5] for more information.

3.5 Eigenvalue Problem

The aim of solving the eigenvalue problem in (2.19) is to obtain the most dangerous mode, which is identified by its eigenvalue λ with the largest real part $\sigma = \Re(\lambda)$. We are interested to vary the parameters of the problem such that we obtain $\sigma = 0$ for the most dangerous mode. Due to the large parameter space, solving the eigenvalue problem for every variation of our parameter space, which is defined by the Rayleigh number Ra , the wavenumber k and the inclination angle α , would be an expensive computational endeavour. As such, the eigenvalue problem and the basic flow need to be solved only once which delivers an initial guess for the basic flow \mathbf{q}_0 and the eigenmodes $\hat{\mathbf{q}}_i$. This initial guess is utilised by the continuation method, which varies the problem's parameters to locate the neutral states, as described in Section 3.8 below. The eigenvalue problem is solved using `scipy`'s `eigs` function. When solving the eigenvalue problem in (2.19), it is not necessary to compute all eigenvalues and eigenmodes. Instead, the algorithm in `eigs` is executed until the largest n_λ eigenvalues and eigenmodes have converged, where n_λ is user determined and is set to 150 in the scope of this thesis. Solving (2.19) delivers the eigenvalue spectrum around $(\Re(\lambda)=0, \Im(\lambda)=0)$.

However, `eigs` is based on ARPACK's shift and invert spectral transformation mode which improves convergence around a specific portion of the spectrum [30]. This can be beneficial if we wish to obtain oscillatory modes with $\Re(\lambda) \approx 0$ and $\Im(\lambda) \neq 0$, as the eigenvalues of these modes can be missed by the algorithm without shifting the spectrum. Applying the transformation on (2.19) expands it to

$$(\mathcal{A}(\mathbf{q}_0) - \sigma_\lambda \mathcal{B})^{-1} \mathcal{B} \cdot \hat{\mathbf{q}}_i = \hat{\mathbf{q}}_i v_\lambda. \quad (3.7)$$

σ_λ is user defined number that shifts the eigenvalue spectrum and is usually sufficient to set it to 10^4 in the scope of this thesis. The transformed eigenvalues v_λ are defined as

$$v_\lambda = \frac{1}{\lambda - \sigma_\lambda}. \quad (3.8)$$

Once computed, the eigenvalues v_λ can be used to find the actual eigenvalues of the problem λ through (3.8).

Even if we consider the transformed eigenvalue problem, it still represents an expensive computational operation. It cannot be solved by a simple matrix inversion, because matrices such as $\mathcal{A}(\mathbf{q}_0)$ are too large to be inverted directly. The size of $\mathcal{A}(\mathbf{q}_0)$ depends on the number of unknown variables on every mesh element. With the chosen mesh in Figure 3.1, this results in a 56481×56481 sized matrix. In order to remedy this, `eigs` uses an IRAM algorithm, which stands for Implicit Restarted Arnoldi Method. The simple Arnoldi method itself belongs to the Krylov subspace methods [6]. The method uses an arbitrary initial vector \mathbf{b} and then computes the products in a Krylov space which is defined as

$$K_n = [\mathbf{b}, \mathcal{A} \cdot \mathbf{b}, \mathcal{A}^2 \cdot \mathbf{b}, \dots, \mathcal{A}^{n-1} \cdot \mathbf{b}]. \quad (3.9)$$

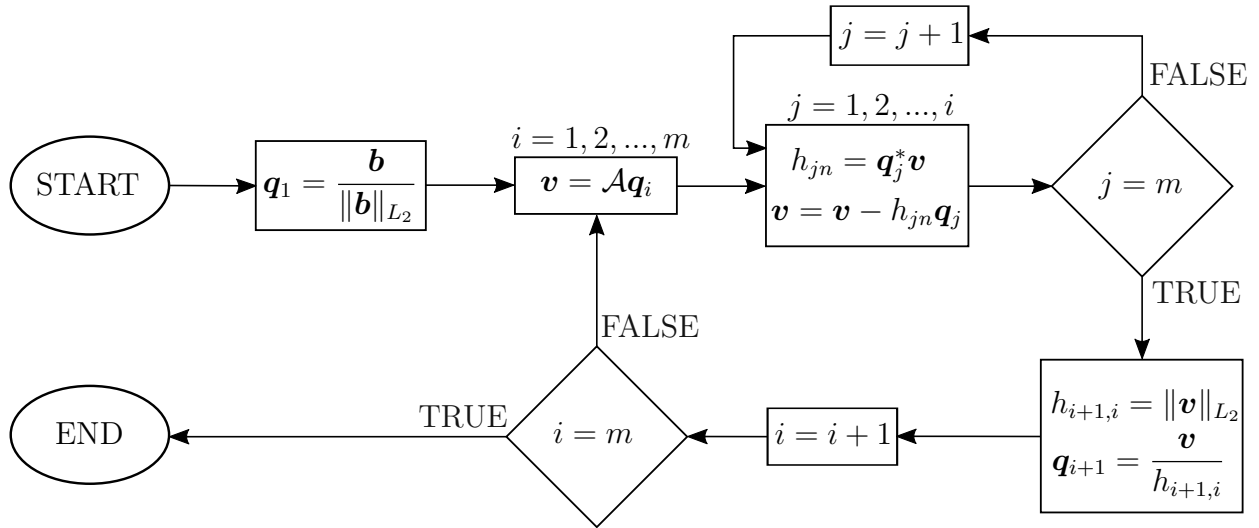


FIGURE 3.2 – Arnoldi method block diagram.

The largest matrix of the eigenvalue problem $\mathcal{A}(\mathbf{q}_0)$ can be decomposed into a product of three matrices such that

$$\mathcal{A} = \mathcal{Q} \cdot \mathcal{H} \cdot \mathcal{Q}^*, \quad (3.10)$$

where \mathcal{Q} is a unitary matrix and \mathcal{H} an upper Hessenberg matrix. The matrices \mathcal{Q} , \mathcal{H} and \mathcal{A} are equally sized with $m \times m$ elements and in our case $m = 56481$. In order to obtain \mathcal{Q} and \mathcal{H} , the algorithm follows the steps in the block diagram in Figure 3.2. The algorithm first uses an arbitrary vector \mathbf{b} and then proceeds to obtain first the elements of \mathcal{H} and then \mathcal{Q} . The most expensive operation is the multiplication step of $\mathbf{v} = \mathcal{A} \cdot \mathbf{q}_i$, because of the size of \mathcal{A} .

IRAM uses a similar algorithm, with the difference that an additional transformation step is applied to \mathcal{H} . First, a real shift μ is applied on \mathcal{H} and then the resulting matrix is decomposed into a product of an upper Hessenberg matrix \mathcal{Q}_H and an upper triangular matrix \mathcal{R}_H using a QR algorithm such that

$$\mathcal{H} - \mu \mathcal{I} = \mathcal{Q}_H \cdot \mathcal{R}_H. \quad (3.11)$$

The transformed matrix can then be reinserted in the Arnoldi iteration which does not have to be restarted from scratch, since \mathcal{A} and \mathbf{q}_i remain the same as before. More information about IRAM and the shift and invert method can be found in [30].

3.6 Spectral Element Solver: NEK5000

In order to verify the results of the basic flow in Chapter 5, a spectral element software was used. NEK5000 is capable of solving large scale time dependent flow problems using high order polynomials [16]. A third-order BDF-EXT scheme, which stands for backwards differentiation formulae with a time extrapolation scheme, is used for time intergration. The spatial integration is achieved using tenth order piecewise polynomials defined with the Gauss–Legendre–Lobatto points on a 20×20 mesh.

3.7 Arc Length Continuation for the Basic Flow

Directly solving the basic flow equations in (2.16) with Newton's method as describe in 3.4, does not provide all possible steady state solutions when the fluid is heated from below. This is due to a state multiplicity which is realisable with an inclination angle $\alpha < |\Delta\alpha|$, where $\Delta\alpha \in [0^\circ, 25^\circ]$ is the angle span where a state multiplicity was observed in the present results. The exact value of $\Delta\alpha$ is dependent on the Rayleigh number and the boundary condition of the lateral walls and will be discussed in Chapter 5. In order to acquire the multiple steady states within this angle interval, we use the arc length continuation method for the basic flow which tracks only one basic flow solution by varying the inclination angle and starting from a computed guess, which is determined using a pseudo arc length. The present method is based on the Pseudo Arc Length Method in LOCA (Library Of Continuation Algorithms) which is described in [section 2.1.2 of 35]. We define the generalised arc length equation of the basic flow \mathbf{q}_0 and the inclination angle α as

$$l(\mathbf{q}_0, \alpha) = c_1 \|\mathbf{q}_0^n - \mathbf{q}_0^{n-1}\|_{L^2}^2 + c_2 |\alpha^n - \alpha^{n-1}|^2, \quad (3.12)$$

where the superscript n denotes the iteration step and c_1, c_2 are coefficients that apply weight to either \mathbf{q}_0 or α .

Figure 3.3 demonstrates how the method works. The algorithm starts with the initial parameters $(\mathbf{q}_0^{n-1}, \alpha^{n-1})$ and proceeds to predict new guesses $(\mathbf{q}_0^{j+1}, \alpha^{j+1})$ using Newton's method until the solution has converged at the final result of $(\mathbf{q}_0^n, \alpha^n)$. Provided that $c_1 = c_2$, the final result should lie on a circle with its origin at $(\mathbf{q}_0^{n-1}, \alpha^{n-1})$ and a radius of 1, due to the arc length equation in (3.12). If $c_1 \neq c_2$, the circle becomes an ellipse, which could be beneficial if the user wants to apply more weight on either \mathbf{q}_0 or α . Usually better convergence is achieved if $c_1 \neq c_2$, $c_1 > c_2$ and when changes of \mathbf{q}_0 between two iterations remain small, which is possibly traced back to the scaling of the basic flow equations. If we combine the basic flow equation in (2.16) with the arc length equation in (3.12), this leads to the following system of equations

$$\begin{bmatrix} \mathbf{F}(\mathbf{q}_0, \alpha) \\ l(\mathbf{q}_0, \alpha) - 1 \end{bmatrix} = \mathbf{0}, \quad (3.13)$$

which can be solved with Newton's method to form the algorithm

$$\begin{bmatrix} \frac{\partial \mathbf{F}(\mathbf{q}_0, \alpha)}{\partial \mathbf{q}} & \frac{\partial \mathbf{F}(\mathbf{q}_0, \alpha)}{\partial \alpha} \\ \frac{\partial l(\mathbf{q}_0, \alpha)}{\partial \mathbf{q}} & \frac{\partial l(\mathbf{q}_0, \alpha)}{\partial \alpha} \end{bmatrix} \cdot \begin{bmatrix} \Delta \mathbf{q}_0 \\ \Delta \alpha \end{bmatrix} = - \begin{bmatrix} \mathbf{F}(\mathbf{q}_0, \alpha) \\ l(\mathbf{q}_0, \alpha) - 1 \end{bmatrix}. \quad (3.14)$$

In the first iteration, an initial increment for $\Delta\alpha^0$ is defined by the user. With this increment, the first row of equations in (3.14), which represent a non linear problem, are solved using Newton's method. During each iteration step of the Newton method j , new increments $\Delta\mathbf{q}_0^j$ and $\Delta\alpha^j$ are used to compute two new approximations for the basic flow, \mathbf{q}_0^{j+1} and the angle α^{j+1} as

$$\mathbf{q}_0^{j+1} = \mathbf{q}_0^j + r\Delta\mathbf{q}_0^j, \quad (3.15a)$$

$$\alpha^{j+1} = \alpha^j + r\Delta\alpha^j, \quad (3.15b)$$

where $r \in [0, 1]$ is a relaxation factor. The process continues until either of the following conditions for the increments or the residuals have been met

$$\|\Delta\mathbf{q}_0^j\|_{L^2} + |\Delta\alpha^j| < \epsilon_{inc} \quad \vee \quad \|\nabla \mathbf{F}(\mathbf{q}_0^j)\|_{L^2} + |l(\mathbf{q}_0^j, \alpha^j)| < \epsilon_{res}, \quad (3.16)$$

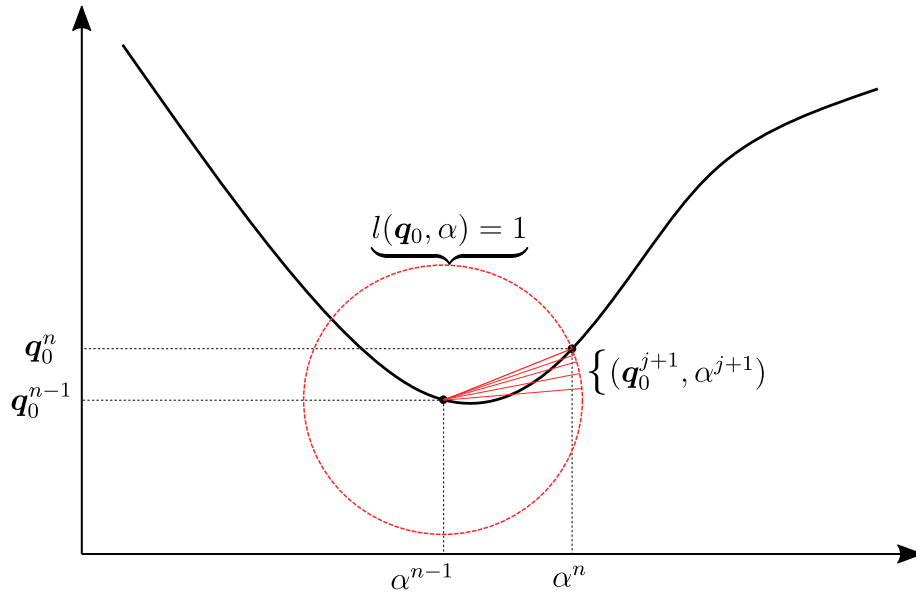


FIGURE 3.3 – Continuation method for the basic flow. The black curve represents the tracked basic flow solution and the circle represents the arc length equation $l(\mathbf{q}_0, \alpha)$ in (3.14), with $c_1, c_2 = 1$.

with $\epsilon_{inc} = 10^{-7}$ and $\epsilon_{res} = 10^{-6}$. Next, starting from the last computed result of $(\mathbf{q}_0^n, \alpha^n)$, the second row of equations in (3.14) is evaluated and the new increments $\Delta \mathbf{q}_0^{n+1}$ and $\Delta \alpha^{n+1}$ are used to obtain two new approximations $\mathbf{q}_0^{n+1}, \alpha^{n+1}$. The new approximations are then used to restart the algorithm by solving the non linear problem in the first row of (3.14). The process repeats itself until a user defined threshold for the angle has been reached.

This method is numerically stable for most cases, but convergence is not always possible, particularly when two solutions with $\|\mathbf{q}_0^1 - \mathbf{q}_0^2\|_{L^2} \ll 1$ and $|\alpha_1 - \alpha_2| \ll 1$ are possible. In order to enable convergence in such cases, we can adjust c_1 and c_2 in (3.12) by increasing them up to 10%. Should that prove insufficient, the method can be restarted by recomputing the basic flow or from a previously computed basic flow.

3.8 Continuation Method for Neutral Curve Tracking

The continuation method in this section is the main building block of the inhouse code where the linear stability problem is solved. It enables the tracking of the neutral curve of a mode with a variation of one of the problem's parameters. Computing repeatedly the eigenmodes and the basic flow by varying one parameter each time is a very expensive numerical process. However, the continuation method varies one of the problem's parameters in a system which can be solved using Newton's method, without the need of solving the eigenvalue problem. As such, the computational effort is reduced significantly. The method presented here is based on LOCA's user guide, specifically the Hopf Point Tracking Algorithm [section 2.1.2 of 35]. The method requires that the eigenvalue problem in (2.19) is solved at least once, in order to obtain a guess for the eigenmodes. These eigenmodes are complex, with $\hat{\mathbf{q}}_i = \hat{\mathbf{q}}_R + i\hat{\mathbf{q}}_I$, where $\hat{\mathbf{q}}_R, \hat{\mathbf{q}}_I \in \mathbb{R}$ denote their real and imaginary part respectively. Similarly, inserting the normal mode ansatz of the perturbation in (2.12) in the linearized equations in (2.17) leads to a complex matrix: $\mathcal{A}(\mathbf{q}_0) = \mathcal{A}_R + i\mathcal{A}_I$. Inserting these notations in (2.19) and equating both

real and imaginary parts to zero leads to

$$\mathcal{A}_R \cdot \hat{\mathbf{q}}_R - \mathcal{A}_I \cdot \hat{\mathbf{q}}_I + \omega \mathcal{B} \cdot \hat{\mathbf{q}}_I - \sigma \mathcal{B} \cdot \hat{\mathbf{q}}_R = 0, \quad (3.17a)$$

$$\mathcal{A}_I \cdot \hat{\mathbf{q}}_R + \mathcal{A}_R \cdot \hat{\mathbf{q}}_I - \omega \mathcal{B} \cdot \hat{\mathbf{q}}_R - \sigma \mathcal{B} \cdot \hat{\mathbf{q}}_I = 0. \quad (3.17b)$$

Next, in order to investigate the stability of the problem we enforce $\sigma = 0$ such that the real part of the eigenvalue is always 0. As a result, any solution will be automatically a neutral state. For example, if the varying parameter is the Rayleigh number, then the continuation method would output a neutral value Ra_N . This modifies the equations in (3.17) to

$$\mathcal{A}_R \cdot \hat{\mathbf{q}}_R - \mathcal{A}_I \cdot \hat{\mathbf{q}}_I + \omega \mathcal{B} \cdot \hat{\mathbf{q}}_I = 0, \quad (3.18a)$$

$$\mathcal{A}_I \cdot \hat{\mathbf{q}}_R + \mathcal{A}_R \cdot \hat{\mathbf{q}}_I - \omega \mathcal{B} \cdot \hat{\mathbf{q}}_R = 0. \quad (3.18b)$$

Therefore, the original eigenvalue problem is split into a system of equations with two unknowns, $\hat{\mathbf{q}}_R$ and $\hat{\mathbf{q}}_I$. The summarized algorithm reads

$$\mathcal{J}_C \cdot \Delta \mathbf{x} = \mathbf{C}. \quad (3.19)$$

$\Delta \mathbf{x}$ contains the increments with which every unknown variable is incremented after each iteration and is defined as

$$[\Delta \mathbf{q}_0, \Delta \hat{\mathbf{q}}_R, \Delta \hat{\mathbf{q}}_I, \Delta \omega, \Delta P]^T. \quad (3.20)$$

The five unknowns are the basic flow \mathbf{q}_0 , the real and imaginary parts of the eigenmode $\hat{\mathbf{q}}_R$ and $\hat{\mathbf{q}}_I$, the oscillatory frequency ω and P , which denotes the parameter we wish to vary. As of this point, since the Rayleigh number is the parameter of interest, let $P = \text{Ra}$. \mathcal{C} includes the following components and residuals

$$\mathbf{C} = \begin{bmatrix} F(\mathbf{q}_0) \\ \mathcal{A}_R \cdot \hat{\mathbf{q}}_R - \mathcal{A}_I \cdot \hat{\mathbf{q}}_I + \omega \mathcal{B} \cdot \hat{\mathbf{q}}_I \\ \mathcal{A}_I \cdot \hat{\mathbf{q}}_R + \mathcal{A}_R \cdot \hat{\mathbf{q}}_I - \omega \mathcal{B} \cdot \hat{\mathbf{q}}_R \\ \int_{\Omega} \hat{\mathbf{q}}_R \, d\Omega - 1 \\ \int_{\Omega} \hat{\mathbf{q}}_I \, d\Omega \end{bmatrix}. \quad (3.21)$$

The first row contains the basic flow equations, whereas the second and third rows originate from (3.18). The last two rows are scaling conditions for the eigenmodes, where we enforce that the integral of the real part of the eigenmode is one and the imaginary part zero. Finally, \mathcal{J}_C

is the Jacobian of \mathcal{C} and is defined as

$$\begin{bmatrix} \frac{\partial \mathbf{F}(\mathbf{q}_0)}{\partial \mathbf{q}} & 0 & 0 & 0 & \frac{\partial \mathbf{F}(\mathbf{q}_0)}{\partial \text{Ra}} \\ \frac{\partial \mathcal{A}_R}{\partial \mathbf{q}} \cdot \hat{\mathbf{q}}_R - \frac{\partial \mathcal{A}_I}{\partial \mathbf{q}} \cdot \hat{\mathbf{q}}_I & \mathcal{A}_R & -\mathcal{A}_I + \omega \mathcal{B} & \mathcal{B} \cdot \hat{\mathbf{q}}_I & \frac{\partial \mathcal{A}_R}{\partial \text{Ra}} \cdot \hat{\mathbf{q}}_R - \frac{\partial \mathcal{A}_I}{\partial \text{Ra}} \cdot \hat{\mathbf{q}}_I + \omega \frac{\partial \mathcal{B}}{\partial \text{Ra}} \cdot \hat{\mathbf{q}}_I \\ \frac{\partial \mathcal{A}_R}{\partial \mathbf{q}} \cdot \hat{\mathbf{q}}_R + \frac{\partial \mathcal{A}_I}{\partial \mathbf{q}} \cdot \hat{\mathbf{q}}_I & \mathcal{A}_I - \omega \mathcal{B} & \mathcal{A}_R & -\mathcal{B} \cdot \hat{\mathbf{q}}_R & \frac{\partial \mathcal{A}_I}{\partial \text{Ra}} \cdot \hat{\mathbf{q}}_R + \frac{\partial \mathcal{A}_R}{\partial \text{Ra}} \cdot \hat{\mathbf{q}}_I - \omega \frac{\partial \mathcal{B}}{\partial \text{Ra}} \cdot \hat{\mathbf{q}}_R \\ 0 & \hat{\mathbf{q}}_R & 0 & 0 & 0 \\ 0 & 0 & \hat{\mathbf{q}}_I & 0 & 0 \end{bmatrix}. \quad (3.22)$$

The inversion of $\mathcal{J}_{\mathcal{C}}$ is the most expensive step in this algorithm and is achieved through Gaussian elimination. After one iteration, the increments in $\Delta \mathbf{x}$ are applied to every variable such that

$$\mathbf{x}^{n+1} = \mathbf{x}^n + r \Delta \mathbf{x}, \quad (3.23)$$

with n denoting the current iteration step and $r \in [0, 1]$ a relaxation factor. The new variables in \mathbf{x}^{n+1} are then used to rebuild \mathcal{C} and $\mathcal{J}_{\mathcal{C}}$ and the process repeats itself until convergence has been achieved. The main convergence requirement for this method is a starting point which lies in close proximity to the neutral curve. Convergence is achieved when either of the following conditions has been met

$$\|\Delta \mathbf{q}_0^n\|_{L^2} + \|\Delta \hat{\mathbf{q}}_R^n\|_{L^2} + \|\Delta \hat{\mathbf{q}}_I^n\|_{L^2} + |\Delta \omega| + |\Delta \text{Ra}| < \epsilon_{inc} \vee, \quad (3.24a)$$

$$\frac{\mathcal{A}_R^n \hat{\mathbf{q}}_R^n - \mathcal{A}_I^n \cdot \hat{\mathbf{q}}_I^n + \omega^n \mathcal{B} \cdot \hat{\mathbf{q}}_I^n - \sigma^n \mathcal{B} \cdot \hat{\mathbf{q}}_R^n}{\mathcal{A}_R^n \cdot \hat{\mathbf{q}}_R^n - \mathcal{A}_I^n \cdot \hat{\mathbf{q}}_I^n + \omega^n \mathcal{B} \cdot \hat{\mathbf{q}}_I^n} < \epsilon_{res} \vee, \quad (3.24b)$$

$$\frac{\mathcal{A}_I^n \cdot \hat{\mathbf{q}}_R^n + \mathcal{A}_R^n \cdot \hat{\mathbf{q}}_I^n - \omega^n \mathcal{B} \cdot \hat{\mathbf{q}}_R^n - \sigma^n \mathcal{B} \cdot \hat{\mathbf{q}}_I^n}{\mathcal{A}_I^n \cdot \hat{\mathbf{q}}_R^n + \mathcal{A}_R^n \cdot \hat{\mathbf{q}}_I^n - \omega^n \mathcal{B} \cdot \hat{\mathbf{q}}_R^n} < \epsilon_{res} \vee, \quad (3.24c)$$

$$\mathbf{F}(\mathbf{q}_0^n) < \epsilon_{res}, \quad (3.24d)$$

with $\epsilon_{inc} = \epsilon_{res} = 10^{-5}$.

3.9 Coarse Eigenvalue Study

In order to get a good approximation for the eigenmodes with which the continuation method in Section 3.8 can be initiated, a coarse study of the eigenvalues was conducted beforehand. The chosen parameter space for angles with $\alpha < 90^\circ$, the Rayleigh number and the wavenumber is shown in Table 3.1, where the minimum, maximum and interval points for each parameter are shown. The eigenvalue problem was solved for every possible combination of these parameters, which is equivalent to 2850 times.

The parameter space for $\alpha > 90^\circ$, shown in Table 3.2, was chosen differently because the critical modes are located at higher Rayleigh numbers as well as wavenumbers. Moreover, the eigenvalue problem was not solved for all combinations of the parameter space, because otherwise this would have been a very expensive computational effort due to the size of the parameter space. Instead, the study is initiated at a specific angle and a Rayleigh number

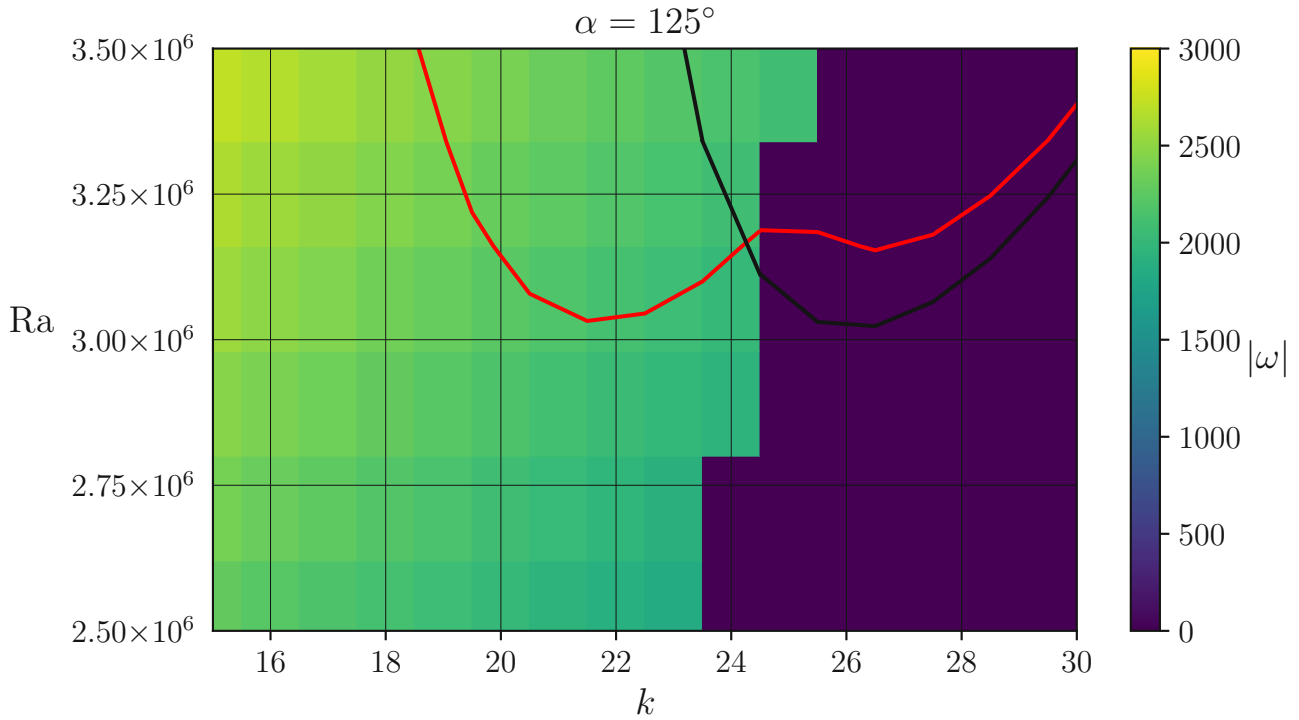


FIGURE 3.4 – Coarse eigenvalue study, $\alpha = -35^\circ$. Two different neutral modes can be identified which are represented by the black, red and green curves with Ra as a function of k . The background color shows the magnitude of ω of the eigenvalue with the largest real part.

Parameter	Minimum	Maximum	Interval Points
α	0°	80°	10
Ra	10^5	2×10^6	19
k	1	15	15

TABLE 3.1 – Parameter space for the coarse eigenvalue study, $\alpha < 90^\circ$.

Parameter	Minimum	Maximum	Interval Points
α	-70°	-10°	20
Ra	10^6	10^8	20-40
k	10	50	20-30

TABLE 3.2 – Parameter space for the coarse eigenvalue study, $\alpha > 90^\circ$. The interval points for Ra and k are shown in a range because a different number of points was chosen for each angle.

and we proceed solving the eigenvalue problem for every wavenumber in a given interval. The process is then repeated for the same angle by raising the Rayleigh number. Once the critical or other neutral modes of interest are located the study is halted and is re-initiated at a different angle.

Figure 3.4 shows an example plot of the coarse eigenvalue study for $\alpha = 125^\circ$ with two neutral modes. Due to the background color, which shows the magnitude of the oscillation frequency $|\omega|$ of the eigenvalue with the largest real part, we can identify that the red mode is oscillatory and the black mode stationary. For this particular angle, the black mode is also the critical mode because its minimum at $k \approx 26$ has a lower Rayleigh number than the red mode with a minimum at $k \approx 21$.

3.10 Neutral Curve Tracking

The neutral curve of a mode is approximated by the collection of points in a parameter space where $\sigma = 0$. The neutral Rayleigh values Ra_N , which are obtained with the continuation method, are evaluated for specific wavenumbers and angles of inclination. However, since the neutral curves of the Rayleigh number are dependent on both the wavenumber and the angle, the neutral curve must be determined using two separate steps. In the code, these steps are split into an inner and an outer loop. Figure 3.5 shows the complete block diagram for the method, where both code loops are visualized within the blue and green blocks and their functionality will be described in the following sections.

3.10.1 Inner Loop: Ra over k

The inner loop searches for the lowest neutral Rayleigh number Ra_{Nm} with a variation of the wavenumber k . If initialised without any previously computed neutral points, it requires an initial guess $(k_0, Ra_{N,0})$ with a computed basic flow, eigenvalues and eigenmodes. Three initial points are obtained using the continuation method with an increment $\Delta k \in [0.01, 0.1]$ such that $k_{i+1} = k_i + \Delta k$, with $i \in [0, 1]$. These points are then inserted into a polynomial fitting function which predicts a minimum (k_m, Ra_{Nm}) using 2nd order polynomials. After more than four points have been computed, 3rd order polynomials are used for a higher accuracy. The polynomial fitting is achieved using numpy's `polyfit` function. The inner loop is completed

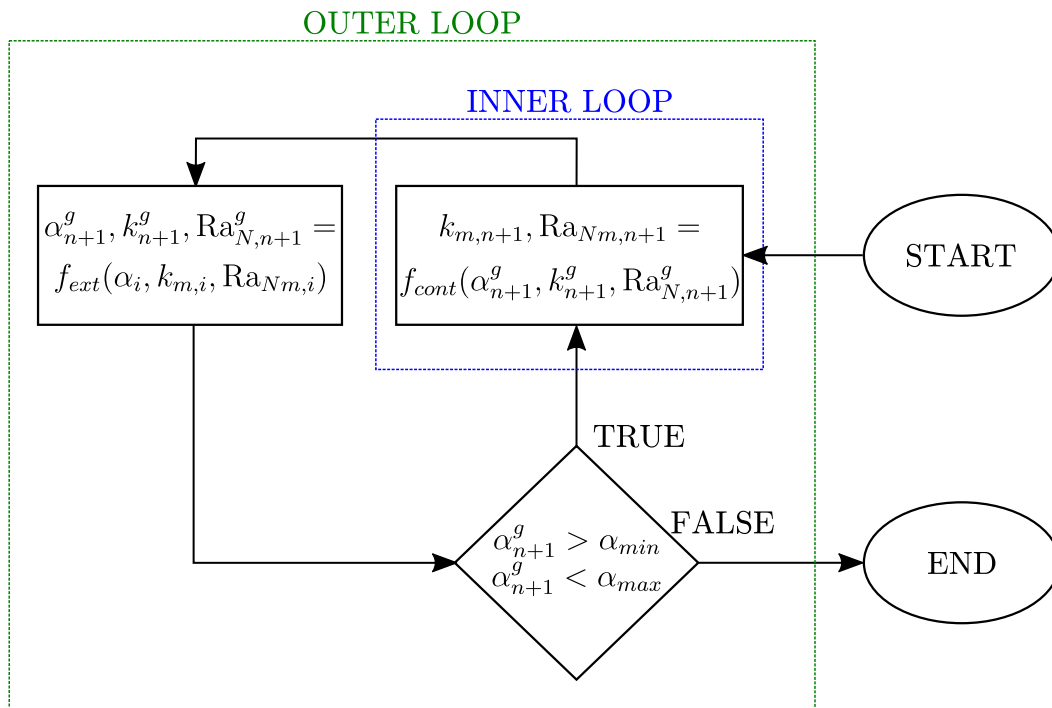


FIGURE 3.5 – Neutral curve tracking block diagram. The inner loop contains the continuation method from Section 3.8 and the outer loop the extrapolation process in (3.26), denoted by f_{cont} and f_{ext} respectively.

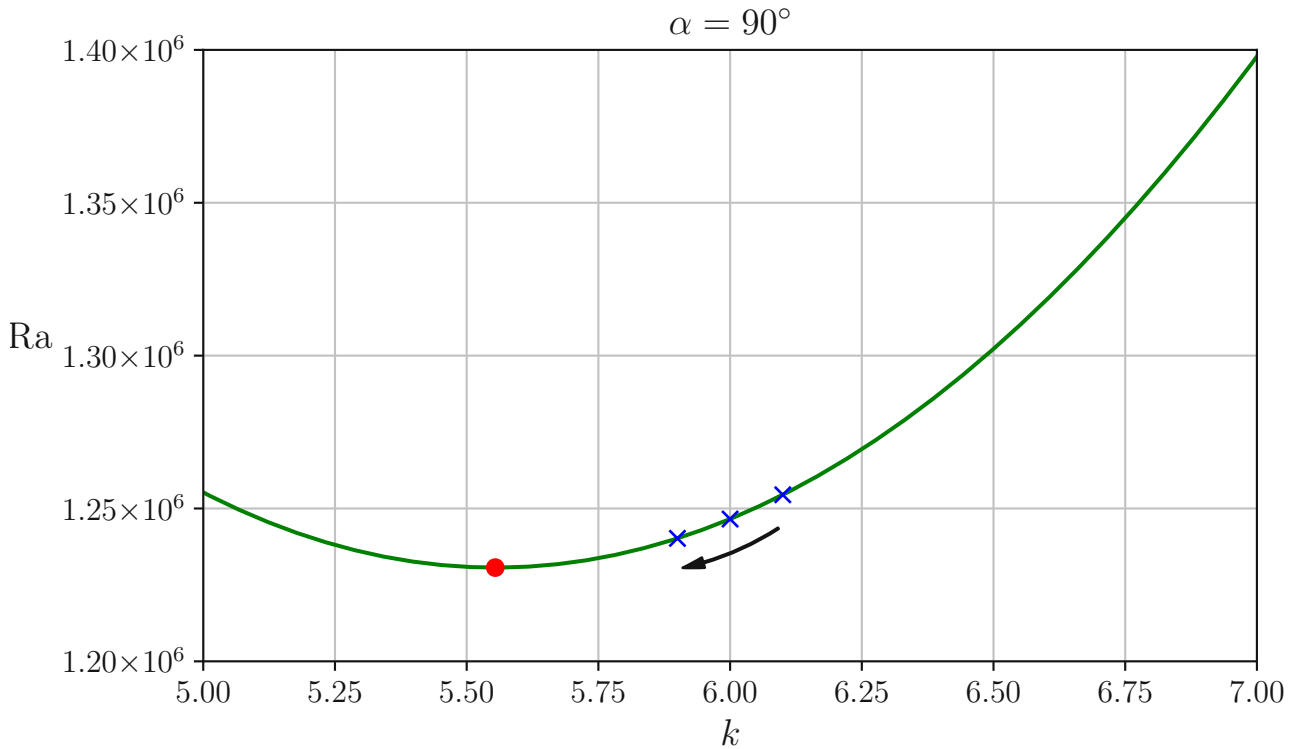


FIGURE 3.6 – Neutral curve tracking: inner loop, $\alpha = 90^\circ$. Blue crosses indicate previously computed neutral points and the red dot the predicted minimum. The arrow shows how the algorithm obtains new critical points in the direction of the predicted minimum.

once convergence for k_m has been achieved, which occurs when the relative tolerance

$$\epsilon_k = \frac{k_{m,i+1} - k_{m,i}}{k_{m,i}} < 10^{-6}. \quad (3.25)$$

The last computed minimum is the lowest neutral point for one specific angle α_n . Furthermore, if there are no other modes with Rayleigh numbers below this point, it is also a critical Rayleigh number at the angle α_n .

Figure 3.6 shows the process of the minimum tracking. The blue crosses represent the computed neutral points which were computed using the continuation method for Hopf bifurcations. The green curve is the polynomial fit of these points and the red point is the predicted minimum (k_m, Ra_{Nm}) . The function proceeds in incrementing k towards the position of the predicted minimum, as indicated by the arrow. In the process, new points are obtained, by progressively approaching the actual minimum. Furthermore, the predicted minimum is also updated using all previously computed points, with more weight on the last computed minimum.

3.10.2 Outer Loop: Ra over α

The outer loop searches for the neutral Rayleigh numbers Ra_N with a variation of the inclination angle α . If no previous minimum neutral points for at least two angles have been computed, the outer loop uses an increment $\Delta\alpha \in [0.05, 0.5]$ such that $\alpha_{n+1} = \alpha_n + \Delta\alpha_n$. The algorithm then enters the inner loop and also obtains $k_{m,n+1}$ and $Ra_{Nm,n+1}$. Two initial points are required to start the extrapolation process in the outer loop. Afterwards, an extrapolation function is used

to predict the minimum of the next angle. The extrapolation function computes the distance d_u between the first computed minimum $(\alpha_0, k_{m,0}, \text{Ra}_{Nm,0})$ and the last computed minimum $(\alpha_M, k_{m,M}, \text{Ra}_{Nm,M})$, with M denoting the total amount of points. The norm of this distance d_u is used to predict the next point along a polynomial, which is derived from the aforementioned computed minima using `numpy's polyfit` function. The predicted point $(\alpha_{n+1}^g, k_{n+1}^g, \text{Ra}_{N,n+1}^g)$ is determined by the following algorithm

$$(\Delta\alpha_n, \Delta k_{m,n}, \Delta \text{Ra}_{Nm,n}) = P \left(1 + \frac{d_u}{M-1} \right), \quad (3.26a)$$

$$(\alpha_{n+1}^g, k_{n+1}^g, \text{Ra}_{N,n+1}^g) = (\alpha_n, k_{m,n}, \text{Ra}_{Nm,n}) + (\Delta\alpha_n, \Delta k_{m,n}, \Delta \text{Ra}_{Nm,n}), \quad (3.26b)$$

where $P(x)$ denotes the polynomial that is derived from all the previously computed minima. Afterwards, the predicted point is inserted in the inner loop and the process repeats itself until a user defined threshold for the inclination angle has been breached.

3.10.3 Error Handling

As previously stated, the neutral curve tracking makes predictions based on the history of the computed minima of the neutral curves. One important feature of this method is the ability to save these points and to load them on prompt. This enables restarting the method without losing data in the eventuality of a crash. Crashes are common due to the numerical instability of the continuation method when the solution diverges significantly from the original guess for the eigenmodes or the basic flow. The first remedy to potential crashes, is setting the relaxation factor to $r < 0.5$ in the inner loop in order to track the first minimum and afterwards to $r = 0.9$. In case changing the relaxation factor proves insufficient, k is altered by 1%, which in most cases enables convergence. Finally, in case these remedies do not succeed in achieving convergence, the eigenvalue problem and the basic flow are recomputed at the point where the method failed to converge. Thus, the method is restarted from the newly computed guess. The method contains additionally various checks to ensure that the same neutral mode is being tracked.

4

Validation

The methods and tools mentioned in the previous section were tested against literature results in benchmark simulations. Additionally, a convergence study was also conducted in order to confirm that the chosen mesh density would provide accurate results. The aim of this section is to prove that all the aforementioned methods and tools were properly validated before being employed in the scope of this thesis. As we only consider air in the cavity, the results below were obtained with $Pr = 0.71$.

4.1 Convergence Study

Tables 4.1 and 4.2 summarise the results of the convergence study, in which the Nusselt number over the hot cavity wall Nu_H is compared for different values of Ra , α and the initial tensor mesh division N with perfectly conducting and adiabatic lateral walls respectively. Nu_H is a non dimensional quantity which is used to quantify the heat transfer over the hot wall and is defined as:

$$Nu_H = - \int_0^1 \frac{\partial \theta}{\partial y} dx. \quad (4.1)$$

Results are omitted for cases where the basic flow solver failed to converge, such as for $Ra > 10^7$ and $\alpha > 30^\circ$ in Table 4.1. However, convergence for such cases is not necessary since the onset of instability occurs at lower Rayleigh numbers with lower angles as shown in Chapter 6 below. Similar cases failed to converge when adiabatic lateral walls were considered, such as for $Ra > 10^8$ and $\alpha > 30^\circ$ in Table 4.2, which are also not relevant since they the maximum Rayleigh number in Chapter 5 is equal to 10^5 . The study showed that $N = 30$ is a good balance between performance and accuracy, since the Nusselt numbers between $N = 30$ and $N = 40$ converge up to the third digit in most cases.

4.2 Modes at $\alpha = 90^\circ$

Table 4.3 presents a comparison between the computed modes and the modes in Winters [37], Gelfgat & Tanasawa [18] and Xin & Le Quéré [38]. All aforementioned papers consider a differentially heated squared cavity with perfectly conducting walls, with a rotation equivalent to $\alpha = 90^\circ$ in this thesis. Winters [37] and Gelfgat & Tanasawa [18] did not use a three dimensional modelling for the perturbation and as such their results represent a non critical, but neutral mode with $k = 0$. The results for $|\omega_N|$ from Xin & Le Quéré [38] were scaled

α	N	Nu_H				
		$Ra = 10^4$	$Ra = 10^5$	$Ra = 10^6$	$Ra = 10^7$	$Ra = 10^8$
10°	20	1.619	2.987	5.243	-	-
	30	1.619	2.990	5.312	-	-
	40	1.619	2.990	5.320	-	-
30°	20	1.779	3.293	6.152	-	-
	30	1.779	3.295	6.188	-	-
	40	1.779	3.296	6.193	-	-
50°	20	1.842	3.420	6.450	11.407	-
	30	1.842	3.422	6.472	11.694	-
	40	1.842	3.422	6.475	11.783	-
70°	20	1.832	3.452	6.789	13.087	-
	30	1.832	3.454	6.798	13.232	-
	40	1.832	3.454	6.799	13.230	-
90°	20	1.748	3.357	6.789	12.731	23.820
	30	1.748	3.358	6.798	12.741	23.948
	40	1.747	3.358	6.799	12.747	23.923
110°	20	1.585	2.955	5.603	10.450	19.281
	30	1.585	2.955	5.605	10.453	19.100
	40	1.585	2.955	5.605	10.448	19.127
130°	20	1.361	2.237	3.876	6.849	12.307
	30	1.361	2.236	3.876	6.846	12.170
	40	1.361	2.236	3.876	6.843	12.141

TABLE 4.1 – Perfectly conducting lateral walls: Nusselt number for different angles α , Rayleigh numbers Ra , and initial tensor mesh division N .

with \sqrt{Ra}/Pr to match the scaling of the system equations in (2.4). Out of the five presented modes, four of them are oscillatory modes, with $|\omega_N| > 0$. The critical mode is a non oscillatory mode with $Ra_c = 1253217$, $k_c = 5.82$ and $|\omega_N| = 0$. On the other hand, the critical mode for oscillatory instability is Mode 2, with $Ra_{c,os} = 1640208$, $k_{c,os} = 7.2$ and $|\omega_{c,os}| = 2150.21$. The relative error for all parameters between the present results and Xin & Le Quéré [38] is in the order of 10^{-3} .

4.3 Neutral Curve of Mode 1

Figure 4.1 shows the neutral curve over the wavenumber k of the critical mode, Mode 1 in Table 4.3. Points below the neutral curve represent stable and above it unstable states. The relative error between the current results and [38] is plotted below the neutral curve and is defined as

$$\epsilon = \left| \frac{Ra_{N,p} - Ra_{N,l}}{Ra_{N,l}} \right|, \quad (4.2)$$

α	N	Nu_H				
		$Ra = 10^4$	$Ra = 10^5$	$Ra = 10^6$	$Ra = 10^7$	$Ra = 10^8$
10°	20	2.286	4.135	6.963	-	-
	30	2.286	4.138	6.992	-	-
	40	2.286	4.138	6.997	-	-
30°	20	2.436	4.417	7.887	14.228	-
	30	2.436	4.420	7.894	14.235	-
	40	2.436	4.420	7.896	14.272	-
50°	20	2.483	4.554	8.432	15.469	28.295
	30	2.483	4.556	8.438	15.502	27.985
	40	2.483	4.556	8.439	15.532	28.185
70°	20	2.428	4.674	8.953	16.682	30.622
	30	2.428	4.675	8.955	16.684	30.543
	40	2.428	4.676	8.955	16.698	30.572
90°	20	2.245	4.521	8.830	16.563	30.709
	30	2.245	4.522	8.827	16.534	30.388
	40	2.245	4.522	8.826	16.527	30.275
110°	20	1.913	3.675	6.868	12.543	22.930
	30	1.913	3.675	6.865	12.511	22.609
	40	1.913	3.674	6.864	12.493	22.492
130°	20	1.505	2.346	3.613	5.642	9.247
	30	1.505	2.346	3.610	5.627	9.081
	40	1.505	2.345	3.610	5.617	9.030

TABLE 4.2 – Adiabatic lateral walls: Nusselt number for different angles α , Rayleigh numbers Ra , and initial tensor mesh division N .

where the index l indicates literature results from [38] and p indicates present results. ϵ is in the order of 10^{-2} for most wavenumbers, with the exception of values for the Rayleigh number where $k < 4$, as a consequence of the steepness of the neutral curve at this range. From this curve, it is also possible to identify the critical point for $\alpha = 90^\circ$ at ($k_c = 5.82$, $Ra_c = 1.25 \times 10^6$), which is also shown in Table 4.3.

		Mode 1	Mode 2	Mode 3	Mode 4	Mode 5
Winters [37]	Ra_N	-	-	-	-	2109200
	k_N	-	-	-	-	0
	$ \omega_N $	-	-	-	-	2745.63
Gelfgat & Tanasawa [18]	Ra_N	-	-	-	-	2108040
	k_N	-	-	-	-	0
	$ \omega_N $	-	-	-	-	2745.19
Xin & Le Quéré [38]	Ra_N	1256870	1640317	1751794	1997110	-
	k_N	5.85	7.19	7.39	7.57	-
	$ \omega_N $	0	2152.02	2637.79	3228.45	-
Current	Ra_N	1253217	1640208	1752476	1999159	2106621
	k_N	5.82	7.20	7.40	7.58	0
	$ \omega_N $	0	2150.21	2636.18	3227.29	2743.59

TABLE 4.3 – Critical Rayleigh number, wavenumber and frequency, for $\alpha = 90^\circ$. All modes are neutral modes except mode 1, which is critical.

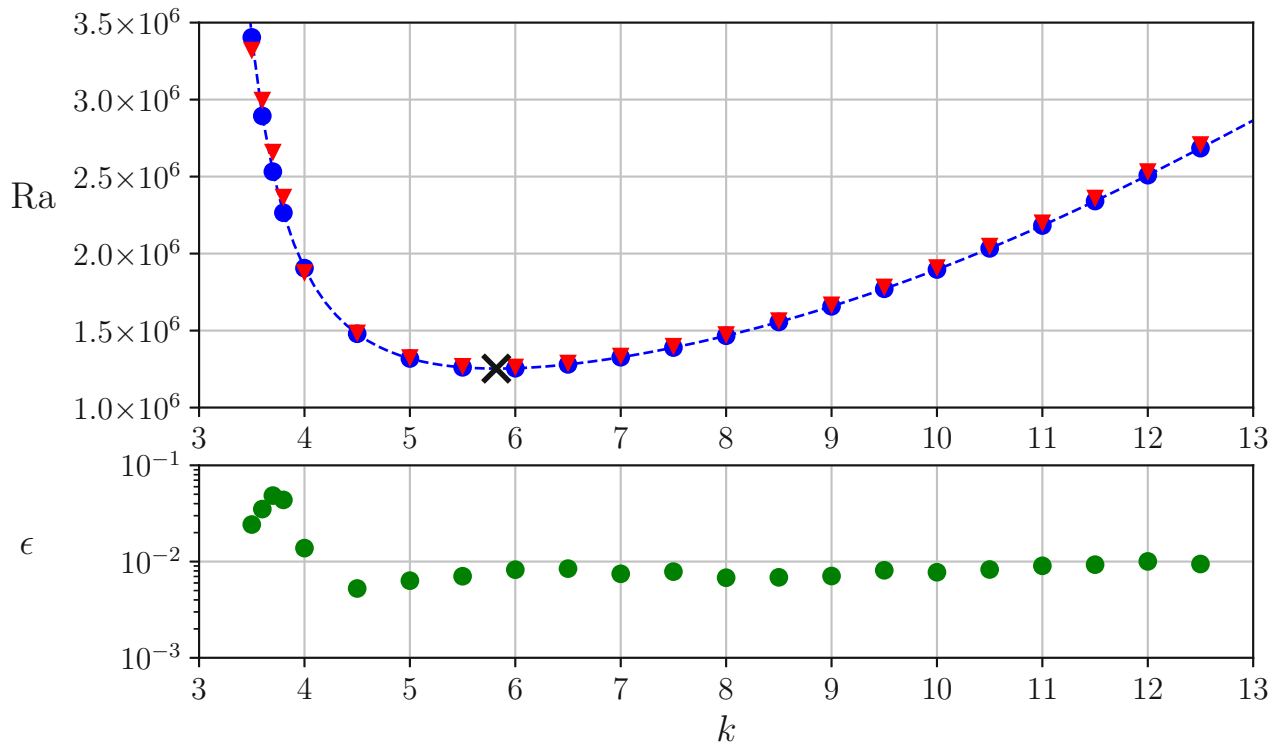


FIGURE 4.1 – Neutral curve of the most dangerous mode as a function of k , $\alpha = 90^\circ$. Blue points indicate current results and red triangles results from Xin & Le Quéré [38]. The curve minimum is marked with a black cross. Below, the error between both datasets is shown.

Steady State Multiplicity

In this section, the evolution of the two-dimensional steady state for two different Rayleigh numbers, $Ra = 2.5 \times 10^4$ and $Ra = 10^5$, upon variation of the inclination angle in the range of $\alpha \in [-180^\circ, 180^\circ]$ is investigated. We consider two different cases for the lateral walls which are either perfectly conducting or adiabatic and that the fluid in the cavity is air with $Pr = 0.71$. The Nusselt number at the hot cavity wall Nu_H , shown in (4.1) above, was used as a means of comparison between the different steady states as well as the maximum and the average flow velocity magnitude which are defined as

$$u_{max} = \max \left(\sqrt{u_x^2 + u_y^2} \right), \quad u_{avg} = \sqrt{\overline{u_x^2 + u_y^2}}, \quad (5.1)$$

respectively and where u_x and u_y are the components of the velocity on the x and y axis respectively. It should also be noted that if we consider two flows at the angles of α and $-\alpha$ and equal Nusselt numbers between the two, then the flow structure of the later will be the mirrored flow structure of the former with respect to $y = 0$, following the symmetry relation of

$$(u_x, u_y, p, \theta, \alpha)(x, y) \rightarrow (-u_x, -u_y, -p, \theta, -\alpha)(-x, y). \quad (5.2)$$

This relation is valid independent of the boundary condition of the lateral walls.

The basic flow was computed conventionally using Newton's method in Chapter 3 for most inclination angles. However, a variation of the inclination angle with $|\alpha| < \Delta\alpha$ and $0 < \Delta\alpha < 25^\circ$ required that the basic flow be computed using the arclength continuation method for the basic flow in Section 3.7 due to an existence of multiple steady states which are smoothly connected to each other. The angle interval where state multiplicity is possible includes angles with $\alpha < |\Delta\alpha|$ and the size of $\Delta\alpha$ is dependent on the Rayleigh number and the boundary condition of the lateral walls, which will be discussed in the sections below. The present results largely agree with the results of Huelsz & Rechtman [23] who considered an identical case as ours with adiabatic lateral walls. However, instead of showing a smooth connection between them the steady states, they observed a discontinuity from one state to another in a form of a hysteresis since they missed some solution branches.

Moreover, many of the presented steady states originate from the two dimensional convection modes of the unstable stratification in a cavity with the same geometry as ours and adiabatic lateral walls which Boullé *et al.* [8] thoroughly outlined in their study. The reader is also referred to the study of Adachi & Mizushima [1], which conducted a similar study with the aim of identifying the two dimensional convection modes of the unstable stratification in a water filled cavity with $Pr = 7$.

5.1 Perfectly Conducting Lateral Walls

First, we consider the case of a cavity with perfectly conducting walls, which corresponds to the default case of this thesis. The evolution of Nu_H over α is shown for $Ra = 2.5 \times 10^4$ and $Ra = 10^5$ in Figure 5.1. The squares represent data from NEK5000, which are in good agreement with the current data, with a relative error for the Nusselt number in the order of 10^{-3} . Independent of the Rayleigh number, the graph is always symmetrical with respect to $\alpha = 0^\circ$ due to the symmetry relation in (5.2). Higher Rayleigh numbers lead to an increase of Nu_H , although at $\alpha = \pm 180^\circ$ the Nusselt number is always 1, which corresponds to a stratified motionless state. The maximum Nusselt number is located at $\alpha = \pm 59.35^\circ$ with $Nu_{H,max} = 2.381$ for $Ra = 2.5 \times 10^4$ and at $\alpha = \pm 70^\circ$ with $Nu_{H,max} = 3.454$ for $Ra = 10^5$.

The multiple states occur at angles $\alpha < |\Delta\alpha|$, with $0 < \Delta\alpha < 8^\circ$. The discovered states are grouped into different, independent solution sets and the number of the sets as well as $\Delta\alpha$ are dependent on the Rayleigh number. As such, a state that belongs to one solution set cannot transition continuously to a solution which belongs to another set. There is always a main solution set whose states have continuous transitions to states that lie outside of the angle interval of state multiplicity, with $\alpha > |\Delta\alpha|$. Therefore, Figure 5.1 displays only the main solution sets and the other discovered solution sets will be shown in detail in the next sections below.

The basic flow is illustrated at the angles of 135° , 90° and 45° along the curve of Nu_H in Figure 5.2. Both Rayleigh numbers lead to a similar flow regime within the cavity until $\alpha = 0^\circ$ and both exhibit a stratification at $\alpha = \pm 180^\circ$. Naturally, the flow at $Ra = 10^5$ exhibits stronger velocity gradients on the walls. As the angle gradually increases, the fluid rotates around a single vortex which eventually evolves into more vortices when the inclination angle lies within the interval of state multiplicity with $|\alpha| < \Delta\alpha$. Since the state multiplicity manifests differently depending on the Rayleigh number, it will be analysed in two separate sections, each covering a different Rayleigh number.

5.1.1 Solution set at $Ra = 2.5 \times 10^4$, conducting lateral walls

The solution set for $Ra = 2.5 \times 10^4$ is shown in detail in Figure 5.3, together with the points (a) to (f) for which the basic flow and their corresponding flow variables are shown in Figure 5.4 and Table 5.1 respectively. In this particular configuration, there is only one solution set. The state multiplicity can be observed between points that have an equal inclination angle, such as the pairs (a)-(f), (b)-(e) and (c)-(d). Despite an equal inclination angle, the Nusselt number and the flow velocity are different between these pairs, as seen in Table 5.1. The solutions that the solver usually locates without the continuation method for the basic flow, are located on the upper branches of the loop, which in this case have Nusselt numbers with $Nu_H > 1.9$. The maximum and average flow velocities are higher on these branches than in the lower branches. As a result, the upper branches are more stable and the solver is able to locate them without the continuation method for the basic flow. At (a) a single clockwise rotating vortex around the centre of the cavity dominates the flow and additionally, two vortices exist on the lower left and upper right corner of the cavity, rotating counter clockwise. Compared to the other points, the Nusselt number and the average flow velocity reach their highest values at (a), with $Nu_H = 1.913$ and $u_{avg} = 23.223$ respectively. It should be noted that another symmetrical solution can exist at (a), with a counter-clockwise rotating flow. The corner vortices gradually grow in size, as seen in (b) and (c) and the Nusselt number decreases to $Nu_H = 1.695$ at

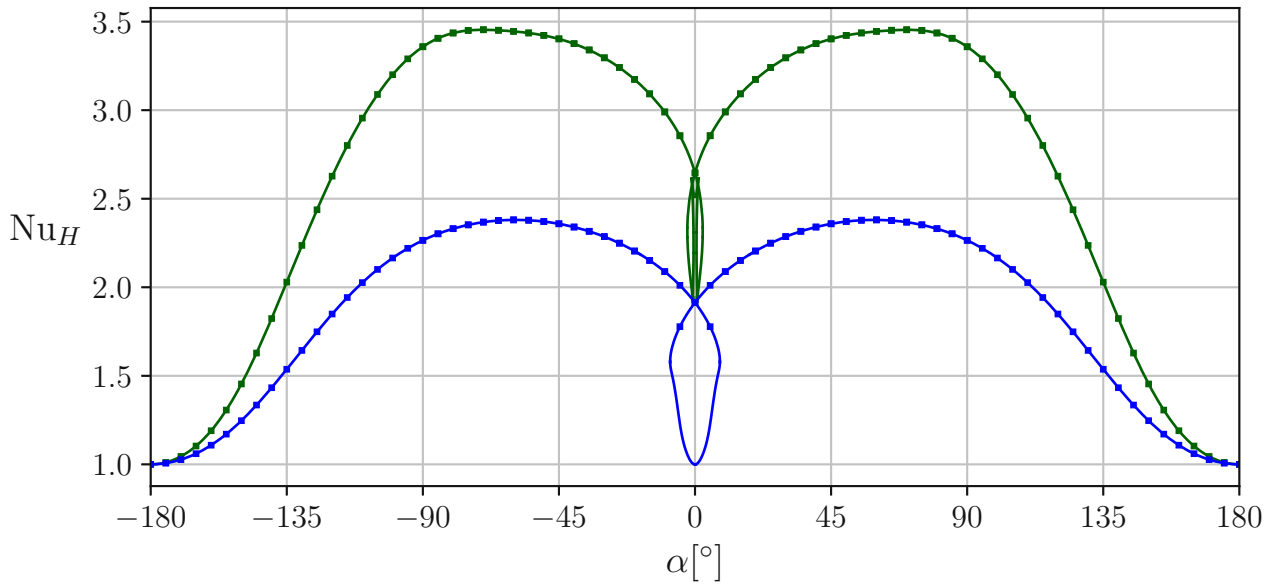


FIGURE 5.1 – Nu_H as a function of α with perfectly conducting lateral walls. Data coloured in blue indicate $Ra = 2.5 \times 10^4$ and in green $Ra = 10^5$. Continuous lines indicate present results, while the squares denote the computed points with NEK5000. The angle interval of state multiplicity, centered around $\alpha = 0^\circ$, is shown in detail in Figures 5.3 and 5.5 for $Ra = 2.5 \times 10^4$ and $Ra = 10^5$ respectively.

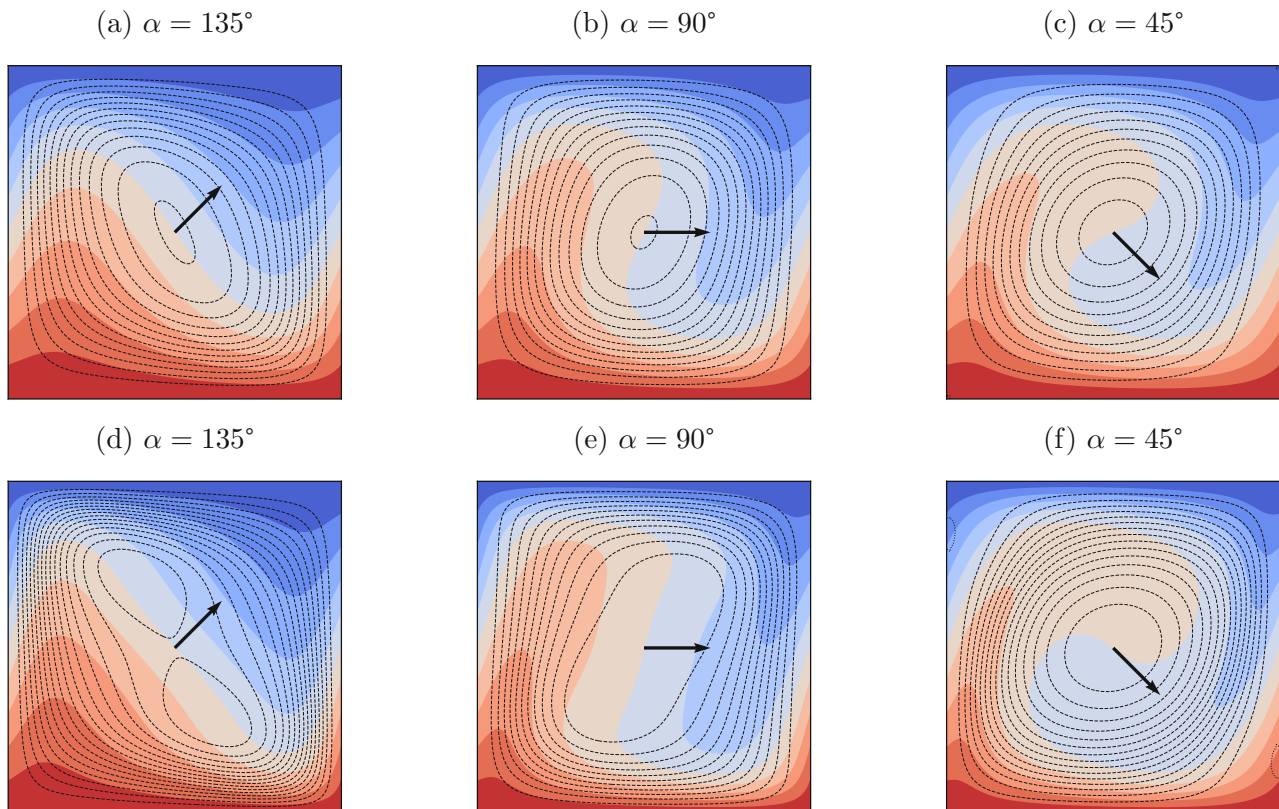


FIGURE 5.2 – Basic flow at different angles with conducting lateral walls, (a)-(c) with $Ra = 2.5 \times 10^4$ and (d)-(f) with $Ra = 10^5$. Temperature is shown by colours, with hot indicating warmer and blue colder areas. The dashed streamlines indicate a clockwise flow in the cavity, with negative vorticity and arrow indicates the direction of gravity.

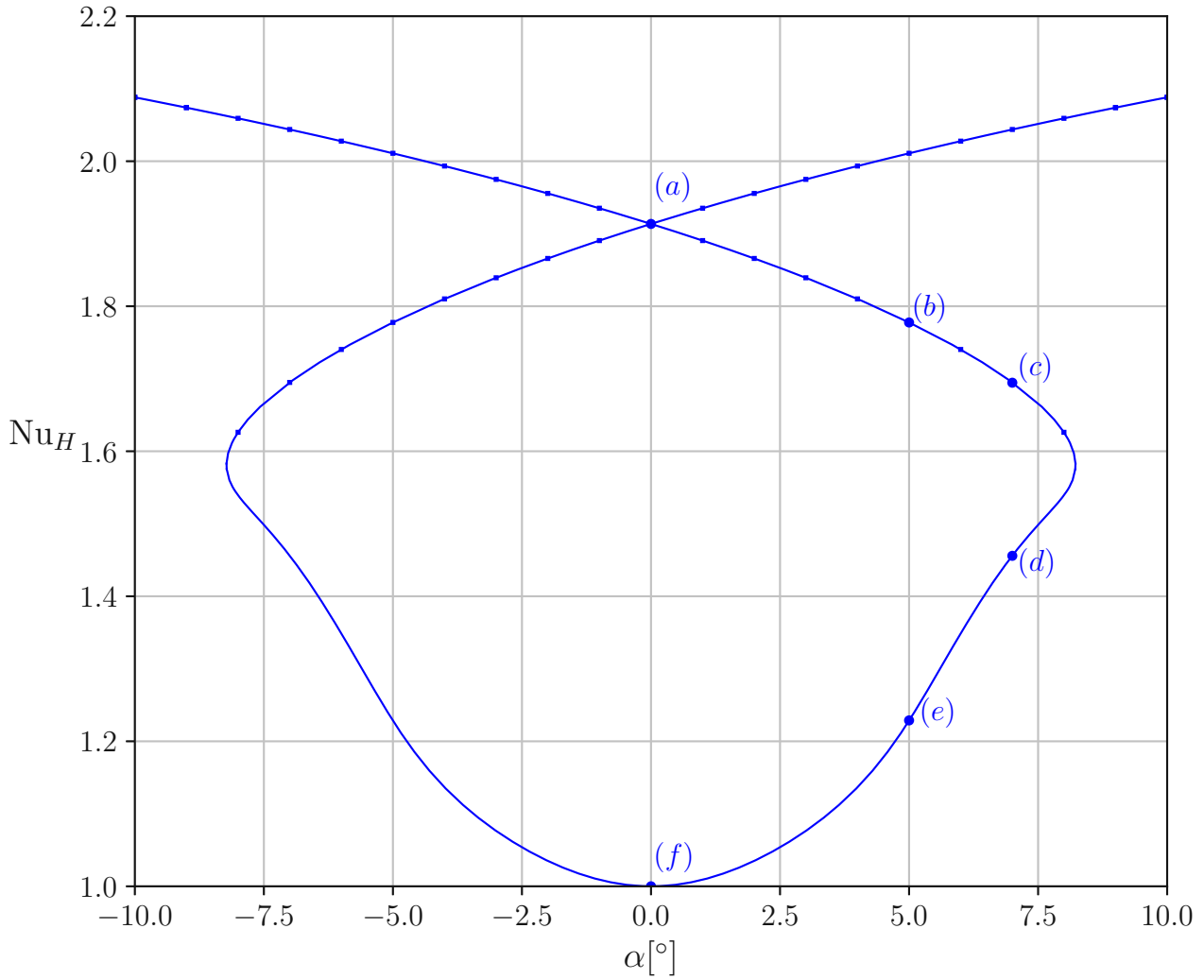


FIGURE 5.3 – $Ra = 2.5 \times 10^4$: Plot of the set of possible solutions as a function of Nu_H over α with conducting lateral walls, including the points of interest (a)-(f). The squares represent data obtained with NEK5000.

	(a)	(b)	(c)	(d)	(e)	(f)
α	0°	5°	7°	7°	5°	0°
Nu_H	1.913	1.778	1.695	1.456	1.229	1
u_{max}	46.069	41.329	38.158	24.519	16.674	0
u_{avg}	23.223	19.289	16.801	9.913	6.401	0

TABLE 5.1 – $Ra = 2.5 \times 10^4$: Flow variables α , Nu_H , u_{max} and u_{avg} at the points (a)-(l) for the solution sets with conducting lateral walls.

(c). At point (d), the corner vortices occupy a much larger area than at (a)-(c) and a sharp reduction of the Nusselt number and the mean flow velocity is observed, with $Nu_H = 1.456$ and $u_{avg} = 9.913$ at (d). Moreover, we can observe a turning point on the loop between (c) and (d) where the reduction takes place, which is located at $\alpha \approx 8^\circ$. This turning point also marks the limit in which state multiplicity is possible, with $\Delta\alpha = \pm 8^\circ$. At (e) the Nusselt number and the average flow velocity are further reduced as the middle vortex moves away from the cavity's corners. Finally, the flow is halted at point (f) due to a stratified temperature field and

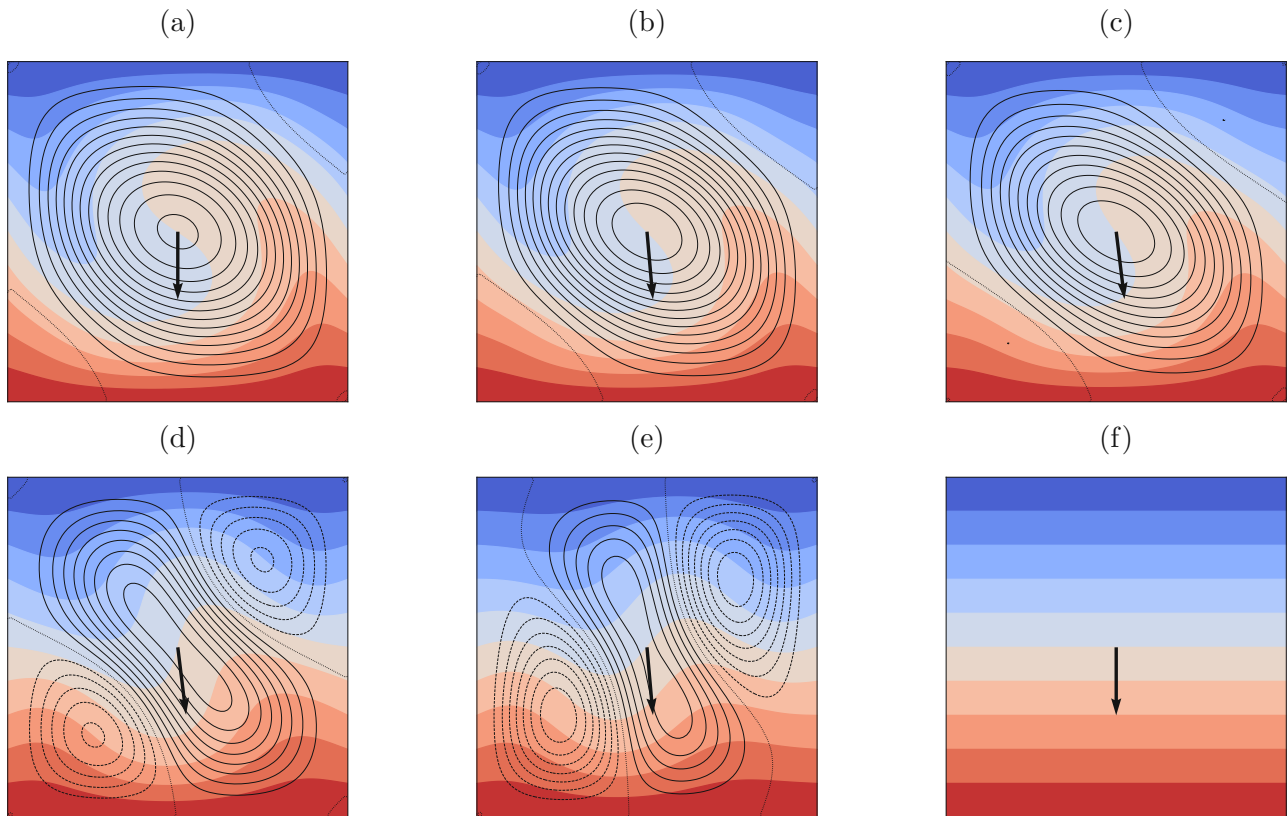


FIGURE 5.4 – $Ra = 2.5 \times 10^4$: Basic flow on the set of possible solutions with conducting lateral walls. The streamlines are represented as full lines in areas with positive vorticity, which indicates a local counter clockwise rotation of the flow. In other aspects, the plots follow the notation in Figure 5.2.

the Nusselt number reaches a minimum of $Nu_{H,min} = 1$.

5.1.2 Solution sets at $Ra = 10^5$, conducting lateral walls

By increasing the Rayleigh number, four separate and independent solution sets were discovered, as shown in Figure 5.5. The main solution set, coloured in blue, is the only set shown in Figure 5.1. The solution sets with lower Nusselt numbers, coloured in red and green are more unstable and have a lower average flow velocity. The angle interval of state multiplicity in this configuration is defined by the maximum angle span of the red solution sets, such that $\Delta\alpha = \pm 4.7^\circ$. Figure 5.6 shows the basic flow on the points (a)-(l) and Table 5.2 shows the flow characteristics of each point.

Overall, the main solution set has higher Nusselt numbers than its counterpart at $Ra = 2.5 \times 10^4$. For instance, the Nusselt number at (a) is equal to 1.913 for $Ra = 2.5 \times 10^4$ as opposed to 2.645 for $Ra = 10^5$. The basic flow in the main solution set at point (a) is very similar to its equivalent point at $Ra = 2.5 \times 10^4$, with a single vortex dominating the flow. The corner vortices gradually increase in size at points (b), (c) and the Nusselt number and the average flow velocity decrease to $Nu_H = 2.131$ and $u_{avg} = 36.130$ at (c). Instead of a transition to a stratification with $Nu_H = 1$, the decrease of the Nusselt number is reversed at $\alpha \approx \pm 1^\circ$. As such, the current data suggests that it is not possible for the fluid to arrive at a resting state when the cavity is tilted from $\alpha > |\Delta\alpha|$ towards $\alpha = 0^\circ$ with a pre-existing flow. At point

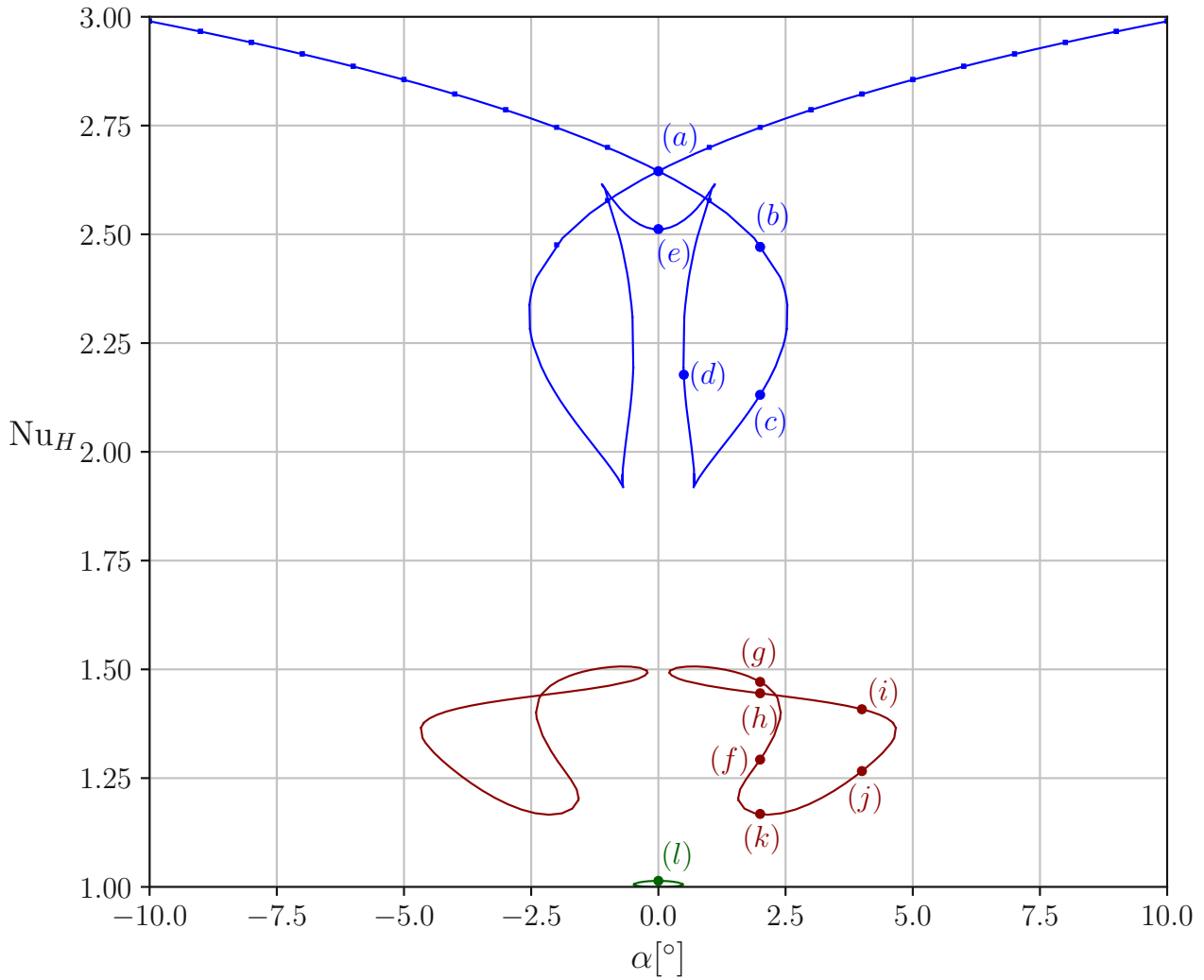


FIGURE 5.5 – $Ra = 10^5$: Plot of the sets of possible solutions as a function of Nu_H over α with conducting lateral walls, including the points of interest (a)-(l). There are four separate solution sets and each set is marked with a different colour, with the exception of the two red coloured sets which are symmetric towards each other. The squares represent data obtained with NEK5000.

	(a)	(b)	(c)	(d)	(e)	(f)
α	0°	2°	2°	0.5°	0°	2°
Nu_H	2.645	2.471	2.131	2.177	2.512	1.293
u_{max}	112.324	106.195	89.240	68.631	76.393	28.189
u_{avg}	53.471	47.733	36.130	30.443	35.724	9.751
	(g)	(h)	(i)	(j)	(k)	(l)
α	2°	2°	4°	4°	2°	0°
Nu_H	1.471	1.445	1.408	1.266	1.168	1.014
u_{max}	43.328	50.983	46.242	30.551	21.764	0.192
u_{avg}	17.067	19.790	17.646	12.046	7.268	0.66

TABLE 5.2 – $Ra = 10^5$: Flow variables α , Nu_H , u_{max} and u_{avg} at the points (a)-(l) for the solution sets with conducting lateral walls.

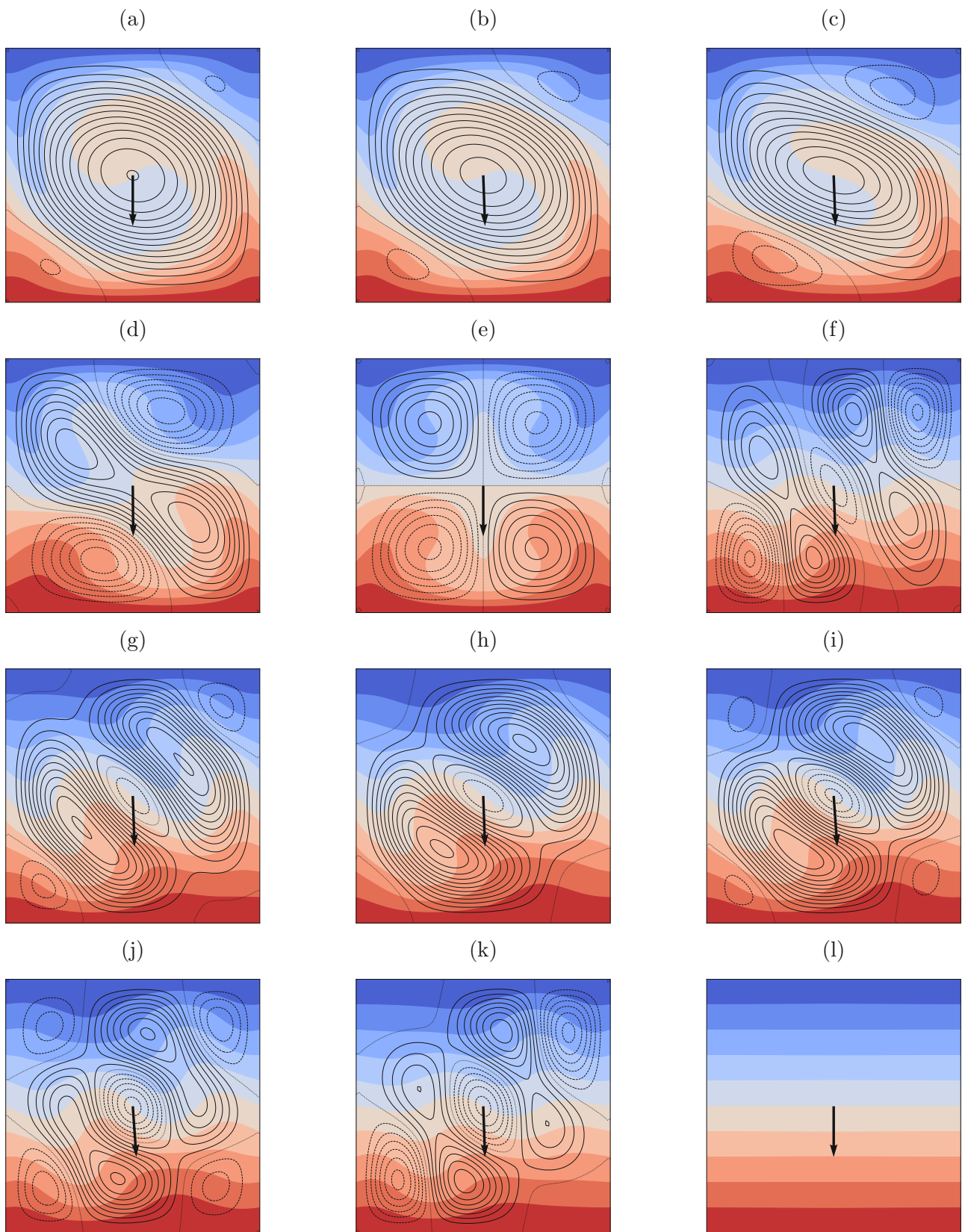


FIGURE 5.6 – $Ra = 10^5$: Basic flow on the solution sets with conducting lateral walls. The plots follow the notation in Figures 5.2 and 5.4.

(d), we see how the original vortex has started to evolve into two additional vortices, which is accompanied by an increase of the Nusselt number to $\text{Nu}_H = 2.177$. (c) and (d) have a similar average flow velocity, although the maximum velocity is higher at (c). Finally, at point (e) four counter-rotating vortices which are equal in strength are formed, with $\text{Nu}_H = 2.512$.

The two following sets, coloured in red, are characterized by a much lower average flow velocity and a greater multitude of vortices compared to the main set, which also leads to lower Nusselt numbers in a range of $\text{Nu}_H \in [1.1, 1.5]$. The points (f)-(k) are part of the red solution set with $\alpha > 0$. The flow patterns are similar to those of the main set, with the difference that many vortices have evolved into two or more additional vortices. For example, points (g)-(i) are very similar to (a)-(c), but the dominating vortex in the latter has evolved into three separate vortices. Similar conclusions can be made between points (d) and (f) or even (e) and (k). Lastly, the flow on the green set includes flows with a negligible average flow velocity which does not change significantly from the conducting state, as seen at its highest point (l), with $\text{Nu}_H \approx 1$ as well as $u_{avg}, u_{max} \approx 0$.

5.2 Adiabatic Lateral Walls

Figure 5.7 shows the curve of Nu_H over α when we consider adiabatic lateral walls. In the present data, the maximum Nusselt number is located at $\alpha = \pm 56^\circ$ with $\text{Nu}_{H,max} = 3.193$ with $\text{Ra} = 2.5 \times 10^4$ and at $\alpha = \pm 75^\circ$ with $\text{Nu}_{H,max} = 4.684$ with $\text{Ra} = 10^5$, while the minimum Nusselt number in both cases is one. The multiple states occur at angles $\alpha < |\Delta\alpha|$ with $\Delta\alpha < |23^\circ|$.

Data from NEK5000 are once again in good agreement with the present data, with a relative error in the order of 10^{-3} . Moreover, data from [23] also largely agree with the present data with the maximum relative error amounting to 3.92% at $\alpha = \pm 40^\circ$ with $\text{Ra} = 10^5$. The study includes data for the Nusselt number within the angle interval of state multiplicity for both Rayleigh numbers, as well as for $\alpha \in [-180^\circ, 180^\circ]$ with $\text{Ra} = 10^5$.

The study of Huelsz & Rechtman [23] used a transient approach coupled with a lattice Boltzman method to locate the steady states and therefore, they missed some solutions within the angle interval of state multiplicity. Instead, they discovered steady states on the upper branches on the main solution set, which are marked as crosses in Figure 5.7. While varying the inclination angle from $\alpha = -180^\circ$ to $\alpha = 180^\circ$, they observed that the Nusselt number gradually decreased for angles within the interval of state multiplicity but as of a certain inclination angle the Nusselt number rapidly increased again, which was caused by a discontinuity between the solutions. This discontinuity manifested itself at either of two angles, $\pm\alpha_{dis}$ depending on whether the cavity was tilted from $\alpha = -180^\circ$ to $\alpha = 180^\circ$ or backwards, which formed a hysteresis. In their data, the discontinuity occurred at $\alpha_{dis} = \pm 21^\circ$ with $\text{Ra} = 2.5 \times 10^4$ and at $\alpha_{dis} = \pm 18^\circ$ with $\text{Ra} = 10^5$. Since NEK5000 also uses a transient scheme, no solutions were retrieved on the lower branches of the main solution set and a discontinuity was also observed which occurred at approximately the same angles as in [23].

The basic flow is illustrated at the angles of 135° , 90° and 45° along the curve of Nu_H in Figure 5.8. We see a similar flow structure as with conducting lateral walls in Figure 5.2, with a single, dominant vortex in the cavity. However, the velocity gradients on the boundaries for both Rayleigh numbers are stronger as opposed to those with the conducting lateral walls.

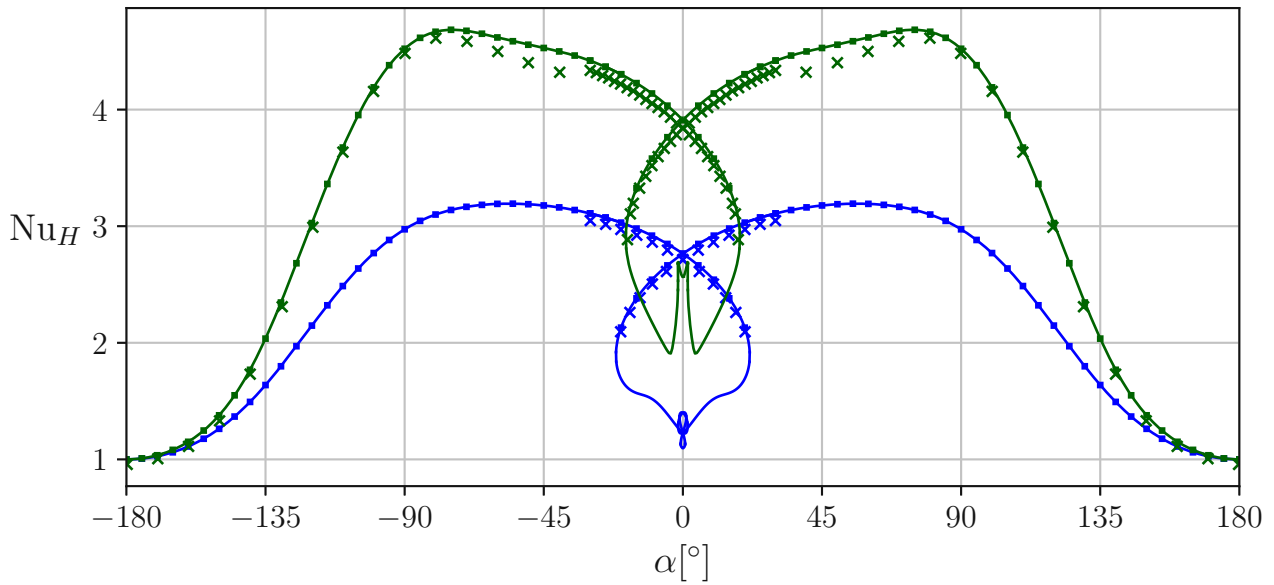


FIGURE 5.7 – Nu_H as a function of α with adiabatic lateral walls. Data coloured in blue indicate $Ra = 2.5 \times 10^4$ and in green $Ra = 10^5$. Continuous lines indicate present results, while the squares denote the computed points with NEK5000. The crosses represent literature data from Huelsz & Rechtman [23]. The angle interval of state multiplicity, centered around $\alpha = 0^\circ$, is shown in detail in Figures 5.9 and 5.11 for $Ra = 2.5 \times 10^4$ and $Ra = 10^5$ respectively.

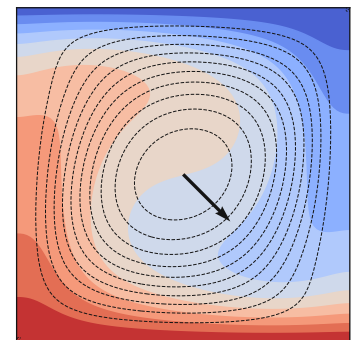
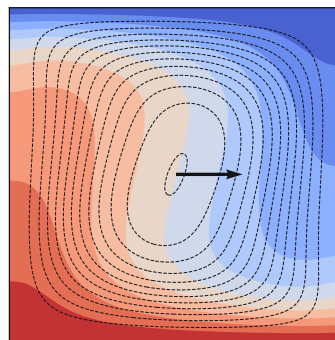
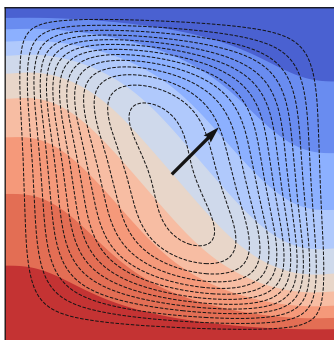
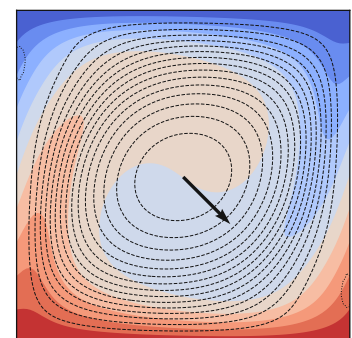
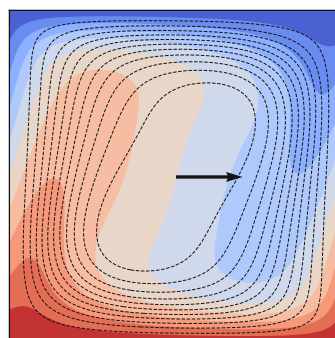
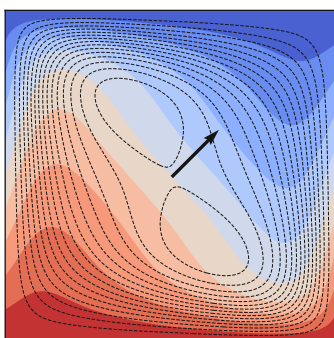
(a) $\alpha = 135^\circ$ (b) $\alpha = 90^\circ$ (c) $\alpha = 45^\circ$ (d) $\alpha = 135^\circ$ (e) $\alpha = 90^\circ$ (f) $\alpha = 45^\circ$ 

FIGURE 5.8 – Basic flow at different angles with adiabatic lateral walls, (a)-(c) with $Ra = 2.5 \times 10^4$ and (d)-(f) with $Ra = 10^5$. The plots follow the notation in Figures 5.2 and 5.4.

5.2.1 Solution sets at $Ra = 2.5 \times 10^4$, adiabatic lateral walls

The solution sets for $Ra = 2.5 \times 10^4$ are shown in detail in Figure 5.9 by Nu_H as a function of α . Two distinct solution sets can be identified, the main set, plotted in blue and a second set, plotted in red. The angle interval of state multiplicity where $\alpha < |\Delta\alpha|$ can be defined by the maximum angle of the main set, such that $\Delta\alpha = \pm 21^\circ$. The crosses spanning the upper branches of the main solution set, represent literature data from Huelsz & Rechtman [23]. They agree largely with the present data, with a consistent error of under 2%. The basic flow at the points (a)-(l) is shown in Figure 5.10 and their respective flow variables in Table 5.3.

Much like with conducting lateral walls, a single vortex dominates the flow as seen at the points (a)-(b) with two diagonally placed vortices on the upper left and lower right corner of the cavity respectively. Point (a) has the highest Nusselt number and average flow velocity out of all points, with $Nu_H = 2.764$ and $u_{avg} = 32.249$ respectively. At point (c), the diagonally placed vortices have grown in size and the Nusselt number as well as the average flow velocity have decreased significantly compared to (a)-(b), with $Nu_H = 1.691$ and $u_{avg} = 15.404$ respectively. The transition from (a) to (c) requires a much larger maximum angle span of $\Delta\alpha = \pm 21^\circ$ compared to $\Delta\alpha = \pm 8^\circ$ in the conducting case for $Ra = 2.5 \times 10^4$. The Nusselt number and the average flow velocity further decrease to $Nu_H = 1.228$ and $u_{avg} = 7.738$ at point (e). After this point, this trend is reversed and the Nusselt number increases to $Nu_H = 1.4$ at point (f). The three vortices become equal in size at point (f) and are in alignment with the gravity vector and the average velocity reaches a local maximum of $u_{avg} = 9.275$. Subsequently, the middle vortex is split into two separate vortices which forms four counter rotating vortices of equal strength at point (h), where $Nu_H = 1.099$ marks the minimum Nusselt number of the main solution set. Point (h) also marks the lowest average velocity of the main solution set, with $u_{avg} = 5.437$.

At point (i) on the second set, we see very similar values for the Nusselt number and the average flow velocity as (h), with $Nu_H = 1.1$ and $u_{avg} = 5.434$ respectively. However, the basic flow at these points differs greatly, since their vortices have an opposite vorticity when compared to each other. At point (i), the fluid is injected towards the heated walls, whereas at point (h) the fluid flows from the heated walls towards the cavity's centre. At points (j) and (k) the average flow velocity gradually decreases, and the upper right and lower left vortices are displaced away from the corners. Finally, the flow is halted at point (l), where the Nusselt number reaches a minimum of $Nu_{H,min} = 1$.

According to the results of Boullé *et al.* [8], there should be four unique states originating from the unsteady stratification for $Ra = 2.5 \times 10^4$, each one corresponding to a different number of vortices at $\alpha = 0^\circ$. The present results have located three of these states, namely the single vortex at (a), the three vortices at (f) and the four vortices at (h) and (i). Therefore, there is probably one solution that was missed which is characterised by two equally sized vortices.

5.2.2 Solution sets at $Ra = 10^5$, adiabatic lateral walls

Figure 5.11 shows the solution sets for $Ra = 10^5$ with Nu_H as a function of α . There is a good agreement between the present results and the literature data of [23], represented by the crosses, with a consistent error of under 2%. The basic flow at the points (a)-(l) is shown in Figure 5.12 and their respective flow variables in Table 5.4. In total, there are three distinct solution sets. The angle interval of state multiplicity where $\alpha < |\Delta\alpha|$ is defined by the maximum angle of the red solution set, $\Delta\alpha = \pm 22^\circ$.

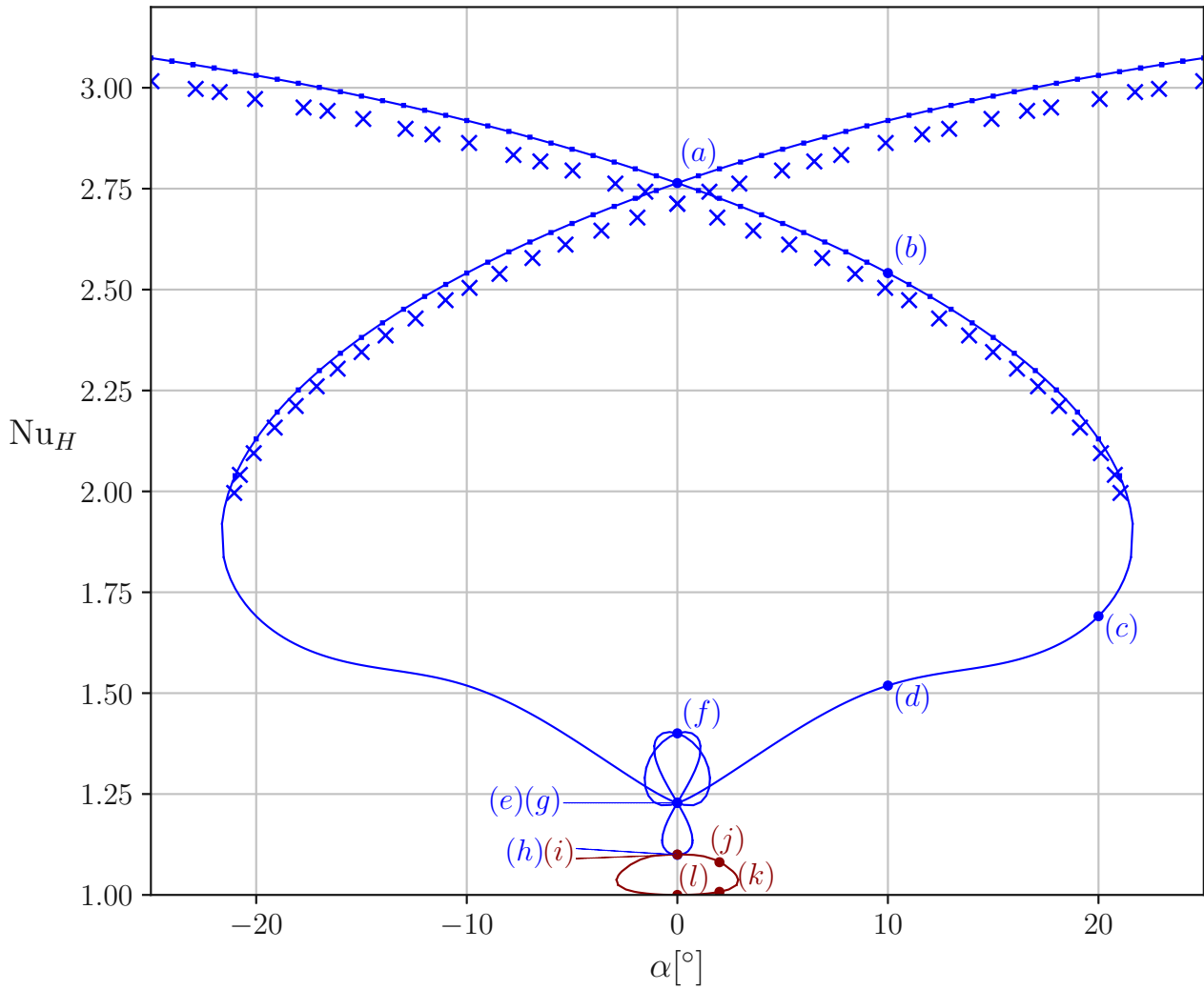


FIGURE 5.9 – $Ra = 2.5 \times 10^4$: Plot of the sets of possible solutions as a function of Nu_H over α with adiabatic lateral walls, including the points of interest (a)-(l). There are two separate solution sets and each set is marked with a different colour. The crosses represent data from Huelsz & Rechtman [23] and the squares data obtained with NEK5000.

	(a)	(b)	(c)	(d)	(e)	(f)
α	0°	20°	10°	10°	0°	0°
Nu_H	2.764	2.541	1.691	1.519	1.228	1.400
u_{max}	59.868	54.066	36.983	29.154	18.159	23.324
u_{avg}	32.249	28.993	15.404	12.446	7.738	9.275
	(g)	(h)	(i)	(j)	(k)	(l)
α	0°	0°	0°	2°	0°	0°
Nu_H	1.228	1.099	1.100	1.081	1.008	1
u_{max}	17.077	10.807	10.904	10.101	2.688	0.006
u_{avg}	6.949	5.437	5.434	4.633	1.112	0.001

TABLE 5.3 – $Ra = 2.5 \times 10^4$: Flow variables α , Nu_H , u_{max} and u_{avg} at the points (a)-(l) for the solutions sets with adiabatic lateral walls.

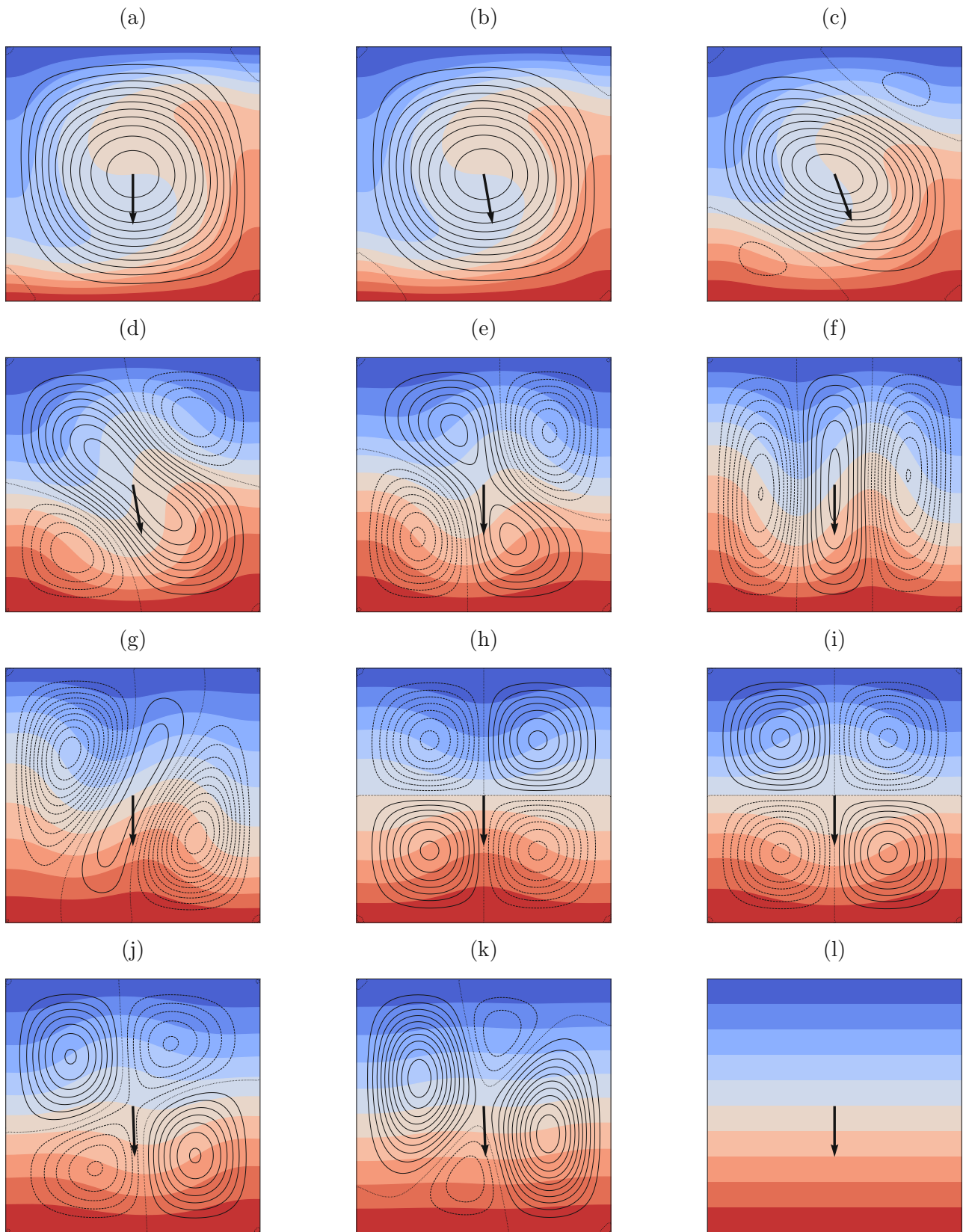


FIGURE 5.10 – $Ra = 2.5 \times 10^4$: Basic flow on the solution sets with adiabatic lateral walls. The plots follow the notation in Figures 5.2 and 5.4.

The main solution set, plotted in blue, has generally higher Nusselt numbers than $Ra = 2.5 \times 10^4$. For instance, the Nusselt number at point (a) amounts to $Nu_H = 3.91$ for $Ra = 10^5$ as opposed to $Nu_H = 2.764$ for $Ra = 2.5 \times 10^4$. Although the upper branches of the main solution set are similar in nature as those for $Ra = 2.5 \times 10^4$, we see a very different evolution of the Nusselt number occurring at its lower branches. Starting from point (a), we once again observe a single vortex dominating the flow. The corner vortices grow gradually at points (b) and (c) and their growth is accompanied by a reduction of the Nusselt number and the average flow velocity until a close proximity to (c) at about $\alpha = 3.5^\circ$. At this point, the Nusselt number reaches a local minimum of $Nu_H \approx 1.9$. By further decreasing the inclination angle, the decrease of the Nusselt number is reversed and the centre vortex evolves into two separate vortices, as seen at (c). Finally, four equally sized, counter rotating vortices appear at point (d), with $Nu_H = 2.568$ and $u_{avg} = 41.949$. Unlike $Ra = 2.5 \times 10^4$, point (d) is not the minimum of the main set. The new minima are instead located close to $\alpha = \pm 3.5^\circ$.

The second set, plotted in red, spans a wide range of Nusselt numbers and angles with $Nu_H \in [1.2, 3.5]$ and $\alpha \in [-22^\circ, 22^\circ]$. At point (e) we see a similar flow as point (d), where the fluid is injected towards the heated walls at the former and the cavity's centre at the later. Contrary to $Ra = 2.5 \times 10^4$, there is a greater difference between the Nusselt numbers and the flow velocities of these points. Nevertheless, the difference between these variables is still small. For instance, the Nusselt number measures $Nu_H = 2.568$ at (d) as opposed to $Nu_H = 2.507$ at (e). At point (f), we see a displacement of the four vortices towards the corners as well as a change in their size. Moreover, the Nusselt number decreases slightly to $Nu_H = 2.075$. The two clockwise rotating vortices at (e) now appear to be merging at point (g), where we also see a significant increase of the Nusselt number to $Nu_H = 3.545$. At about $\alpha = \pm 13^\circ$, the second set reaches its maximum Nusselt number, $Nu_H = 3.66$. Finally, the vortices at (g) evolve into eight equally sized vortices at point (h), where the Nusselt number and the average flow velocity reach a minimum of $Nu_H = 1.218$ and $u_{avg} = 7.214$ respectively.

The third set, coloured in green, is the only solution set which is connected to the stratified, motionless state. Point (i) exhibits a similar solution to point (h), with eight vortices rotating in the opposite direction but with a higher Nusselt number, with $Nu_H = 1.46$. The curve of the Nusselt number crosses the centre of the graph at $\alpha = 0^\circ$ multiple times, with some of the vortices merging at point (j) or even rearranging into nine vortices as seen at point (k). Finally, the flow is halted at point (l) and the Nusselt number reaches a minimum of $Nu_{H,min} = 1$.

According to the results of Boullé *et al.* [8], there should be ten unique states originating from the unsteady stratification for $Ra = 10^5$, each one corresponding to a different number of vortices at $\alpha = 0^\circ$. Presently, a multitude of solutions have not yet been determined, with the exception of the single vortex solution at (a), the three vortices at (j), the four vortices at (d) and (e), the eight vortices at (h) and (i) and the nine vortices at (k).

5.3 Comparison of the State Multiplicity

5.3.1 Variation of the Rayleigh number

A comparison of the solution sets of the Rayleigh numbers $Ra = 2.5 \times 10^4$ and $Ra = 10^5$ shows that the state multiplicity is very sensitive to variations of the Rayleigh number, independent of the boundary condition of the lateral walls. The bifurcation analysis of Boullé *et al.* [8] showed that the number of the modes of the unstable stratification at $\alpha = 0^\circ$ is dependent

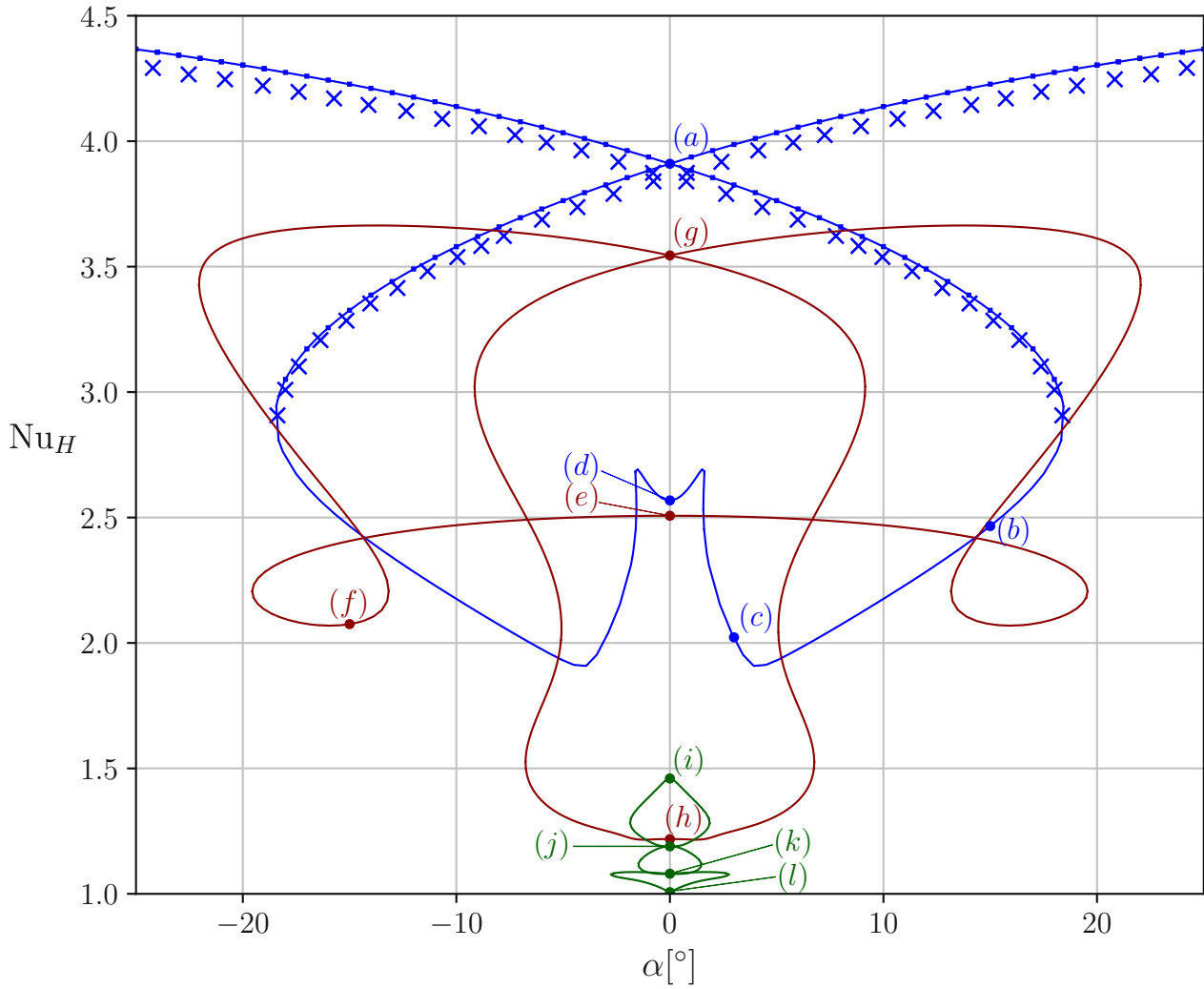


FIGURE 5.11 – $Ra = 10^5$: Plot of the sets of possible solutions as a function of Nu_H over α with adiabatic lateral walls, including the points of interest (a)-(l). There are three separate solution sets and each set is marked with a different colour. The crosses represent data from Huelsz & Rechtman [23] and the squares data obtained with NEK5000.

	(a)	(b)	(c)	(d)	(e)	(f)
α	0°	15°	3°	0°	0°	-15°
Nu_H	3.910	2.466	2.022	2.568	2.507	2.075
u_{max}	141.286	106.756	72.778	85.801	84.077	71.876
u_{avg}	73.005	46.955	31.383	41.494	41.299	31.869
	(g)	(h)	(i)	(j)	(k)	(l)
α	0°	0°	0°	0°	0°	0°
Nu_H	3.545	1.218	1.460	1.189	1.080	1.007
u_{max}	112.172	16.788	36.132	18.827	11.427	0.102
u_{avg}	44.786	7.214	15.789	7.843	4.710	0.041

TABLE 5.4 – $Ra = 10^5$: Flow variables α , Nu_H , u_{max} and u_{avg} at the points (a)-(l) for the solution sets with adiabatic lateral walls.

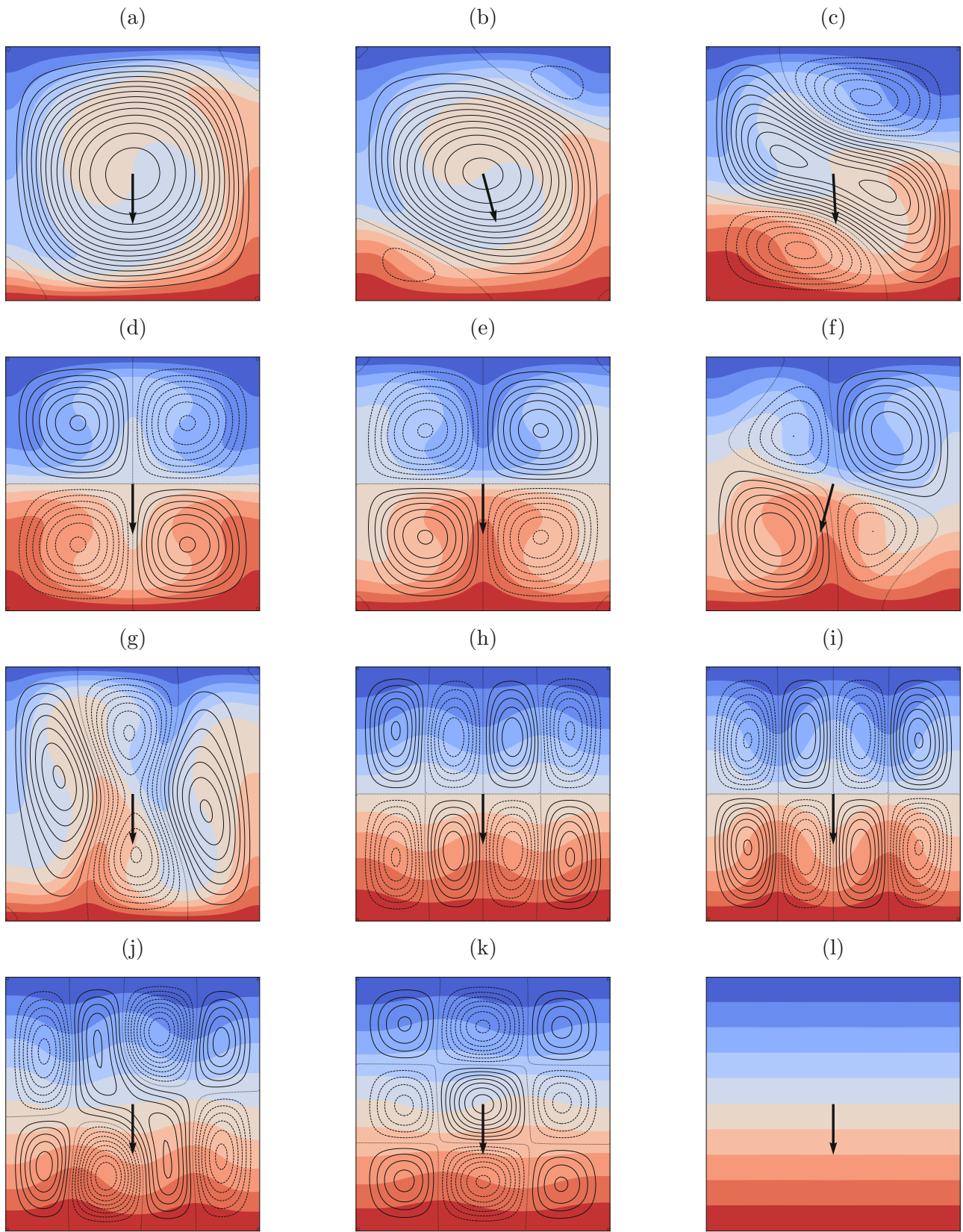


FIGURE 5.12 – $Ra = 10^5$: Basic flow on the solution sets with adiabatic lateral walls. The plots follow the notation in Figures 5.2 and 5.4.

on the Rayleigh number. Considering adiabatic lateral walls, they showed that there are four modes for $Ra = 2.5 \times 10^4$ and ten for $Ra = 10^5$. The present results showed that many of the discovered steady states originate from these modes. As such, higher Rayleigh numbers allow the emergence of more steady states at $\alpha = 0^\circ$.

Through the increase of the Rayleigh number, we also observe an increase of the Nusselt number. In the adiabatic case, the highest Nusselt number at point (a) rises from 2.764 to 3.910 between both Rayleigh numbers, which corresponds to an increase of 41%. Moreover, an increase of the Rayleigh number leads to a decrease of the maximum angle span of the main solution set, with a larger decrease when considering perfectly conducting lateral walls. Additionally, the angle span of the main solution set decreases by 69% with perfectly conducting lateral walls as opposed to 22% with adiabatic lateral walls. Therefore, smaller tilting angles are required on the main set for a smooth transition of the flow when the Rayleigh number increases. Finally, the current results suggest that the minimum Nusselt number of the main set is located at its centre ($\alpha = 0^\circ$) for lower Rayleigh numbers. For higher Rayleigh numbers, this does not seem to be the case since the main set has two symmetrical minima with respect to $\alpha = 0^\circ$.

5.3.2 Conducting or Adiabatic Lateral Walls

The boundary condition of the lateral walls, conducting or adiabatic, also affect the state multiplicity significantly. The current data shows that higher Nusselt numbers are achieved with adiabatic instead of conducting lateral walls. Considering $Ra = 2.5 \times 10^4$, we can observe an increase of the highest Nusselt number at $\alpha = 0^\circ$ from 1.941 to 2.764 between both boundary conditions for the lateral walls, which corresponds to an increase of 42%. Moreover, a conducting boundary condition decreases the maximum angle span of all solution sets. For instance, for $Ra = 2.5 \times 10^4$, we see the angle span changing from $\Delta\alpha \approx 8^\circ$ with conducting lateral walls to $\Delta\alpha \approx 22^\circ$ with adiabatic lateral walls, which corresponds to an increase of 175%. When comparing our results with both boundary conditions for $Ra = 2.5 \times 10^4$, we can also see how the second solution set is completely absent when a conducting boundary condition is chosen.

6

Linear Stability Analysis

Applying all methods that were mentioned in Chapter 3 enables locating the neutral and critical curves which extend in $\alpha \in [-180^\circ, 180^\circ]$. This section presents the neutral and critical curves of the Rayleigh number as a function of α and also illustrates the basic flow and the three dimensional perturbation at a selection of points on the critical curve. The fluid in the cavity is air, with $Pr = 0.71$.

6.1 Neutral and Critical Curves over the Inclination Angle α

Figure 6.1 shows the curve of the critical Rayleigh number Ra_c together with several other critical parameters as a function of the inclination angle α listed below.

- Critical wavenumber k_c
- Critical magnitude of the oscillation frequency $|\omega_c|$
- Normalised buoyancy production term B from (2.27)
- Maximum flow velocity magnitude u_{max} from (5.1)
- Average velocity magnitude u_{avg} from (5.1)

Each mode is represented by a differently coloured neutral curve. If the mode is critical in an angle interval, its neutral curve is represented by a thick line and if there is another critical mode besides it the neutral curve is marked by a thin line. The flow is linearly stable for $Ra < Ra_c$. Due to the symmetry relation of the basic state with respect to 0° in (5.2), only positive angles are shown. The mode which covers the angle range of $\alpha \in [-36^\circ, 36^\circ]$, coloured in purple, has two separate branches as a consequence of the steady state multiplicity. The most dangerous mode is found in the range of $\alpha \in [-10^\circ, 10^\circ]$, coloured in gray, which is a stationary mode with $\omega_c = 0$. Its lowest Rayleigh number is located at $\alpha = 0^\circ$ with $Ra_c = 2941.58$ and $k_c = 3.375$. At this point, the basic state is a stratification with $u_{avg} = 0$. As previously discussed in Chapter 5, there is also a stratification at $\alpha = \pm 180^\circ$ and this is the only possible basic state when the fluid is heated from above. As such, we see that the stability of the flow increases with larger angles as it approaches $\alpha = 180^\circ$, shown by the critical Rayleigh number, which increases by several orders of magnitude. At $\alpha = 180^\circ$ the flow stability is infinite due to an absence of a flow.

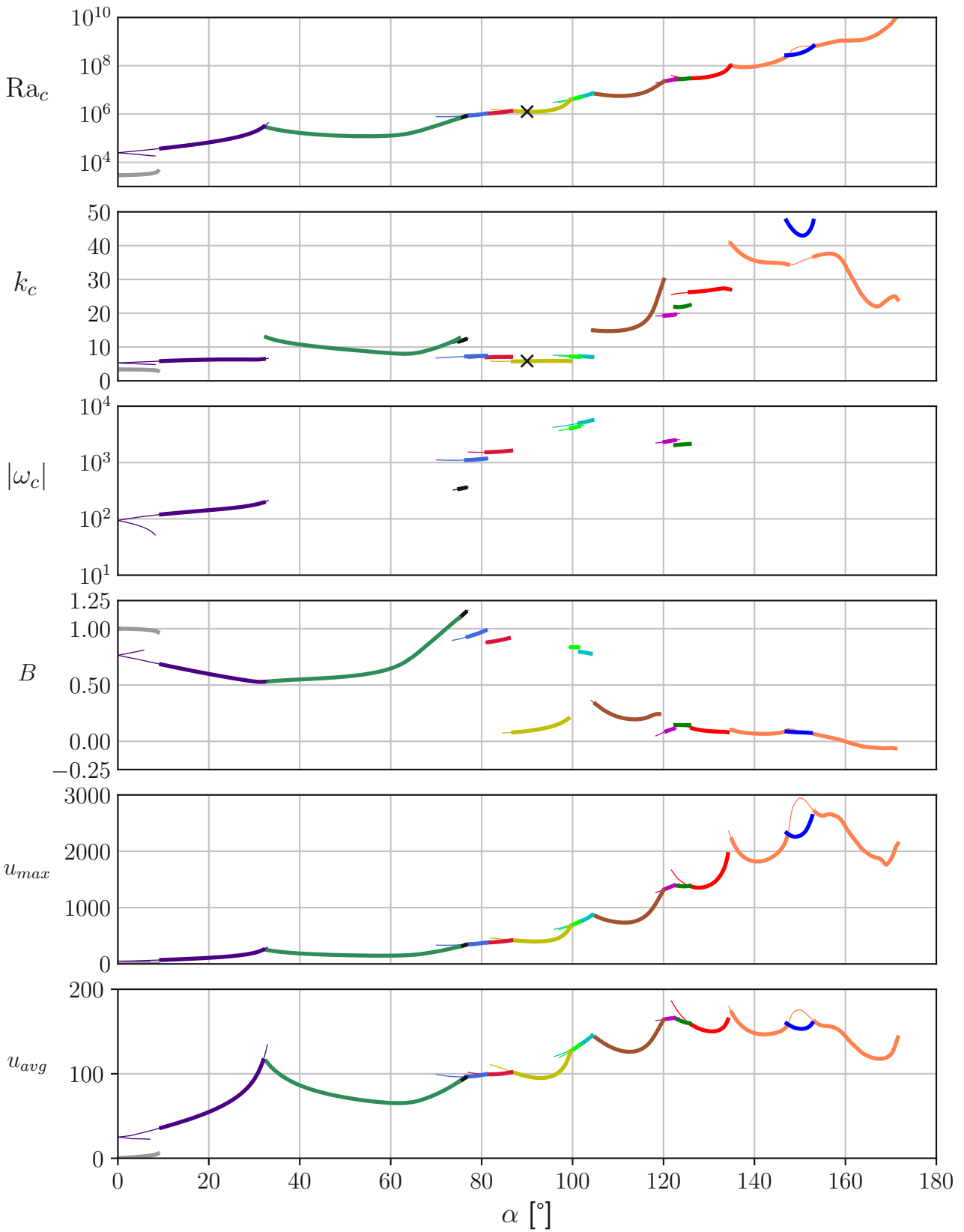


FIGURE 6.1 – Critical and neutral curves as a function of α from top to bottom Ra_c , k_c , ω_c , B , u_{max} and u_{avg} . Each mode is plotted with a different colour and is critical for angles where a thick line is present. Crosses in the graphs of Ra_c and k_c represent literature data from [38].

Smaller inclination angles tend to lead to smaller critical wavenumbers, with $k_c < 15$ for $\alpha < 110^\circ$. However, as α increases, the wavenumbers also increase significantly with $k_c > 15$ as of $\alpha > 110^\circ$. The highest critical wavenumber is detected at $\alpha = 146.88^\circ$ with $k_c = 47.77$. On the other hand, the lowest critical wavenumber is detected at $\alpha = 8.82^\circ$ with $k_c = 2.96$.

Most modes are non oscillating with $\omega_c = 0$ and do not show in Figure 6.1 due to the logarithmic scale in the graph for $|\omega_c|$. Oscillating modes centered around $\alpha = 90^\circ$ have the highest frequencies with $|\omega_c| > 10^3$. The largest frequency is located at $\alpha = 104.31^\circ$ with $|\omega_c| = 5647.18$.

The buoyancy production term B is larger than 0.5 for $\alpha < 86^\circ$, which points to buoyancy being the dominant driving force of the instability mechanism. In the opposite case with $\alpha > 86^\circ$, inertia becomes the dominant destabilising factor instead. An exception to this rule is made by two modes in the angle range of $\alpha \in [99^\circ, 104^\circ]$, displayed with light green and cyan lines, where buoyancy is instead dominant. Otherwise, the transition of the dominant destabilising factor is easily observable on the graph and occurs at $\alpha = 86.55^\circ$, between the red and yellow modes. Starting from the stratification at $\alpha = 0^\circ$ at the gray mode, we observe that the stratification is destabilised entirely due to buoyancy, since $B = 1$. Buoyancy is also dominant on the purple mode at $\alpha = 0^\circ$, however its contribution to the instability decreases by increasing the inclination angle. This trend is reversed at $\alpha = 58^\circ$, when the green mode becomes critical. In the interval of $\alpha \in [72^\circ, 76.5^\circ]$, inertial effects have a stabilising effect on the flow, since $B > 1$ and consequently $I < 0$ in this range. At higher angles there is virtually no contribution from the buoyancy term and destabilisation occurs mainly due to the inertial forces. At even higher angles with $\alpha > 160^\circ$, buoyancy forces even have a stabilising effect on the flow, since $B < 0$ in this range.

The maximum flow velocity u_{max} generally follows the trend of the critical Rayleigh number particularly at higher angles, except for $\alpha > 140^\circ$, where a decrease is observed. The average velocity u_{avg} also increases with higher angles, with the difference that there is no significant increase as of $\alpha > 120^\circ$.

6.2 Three Dimensional Flow Perturbation

In this section, the three dimensional flow perturbation together with the basic flow of neutral and critical states at the angles $\alpha = 0^\circ, 30^\circ, 80^\circ, 90^\circ, 100^\circ, 110^\circ, 120^\circ$ and 140° are presented. Table 6.1 shows the critical values of these states, together with the energy budget. If $\omega_c \neq 0$, its sign indicates the propagation direction of the perturbation. A positive value with $\omega_c > 0$ indicates a propagation from z to $-z$. Due to periodicity, the perturbation is plotted for one wavelength measuring $z_k = 2\pi/k$. We also introduce the phase velocity which is a useful term to describe the propagation of the perturbation in the z -axis in oscillatory modes, defined as

$$u_p = -\frac{\omega z_k}{2\pi} = -\frac{\omega}{k}. \quad (6.1)$$

As such the phase velocity u_p is directly proportional to the oscillation frequency ω and inversely proportional to the wavenumber k .

The most dangerous mode is shown in Figure 6.2a. It is part of the lower branch of the basic state at $\alpha = 0^\circ$ and belongs to the gray mode in Figure 6.1. The basic flow is a stratified temperature field and the mode has the highest wavelength compared to the other plotted modes. Since this is a non-oscillatory mode with $\omega_c = 0$, the isosurfaces of the strongest

α	Ra_c	k_c	ω_c	B	I	z_k	u_p
0°, lower	2.942×10^3	3.375	0.0	1.0	0.0	1.862	0.0
0°, upper	2.509×10^4	5.292	-93.850	0.762	0.232	1.187	17.73
30°	1.826×10^5	6.299	-177.586	0.54	0.467	0.997	28.18
80°	9.829×10^5	7.387	1152.91	0.971	0.031	0.851	-156.151
90°	1.253×10^6	5.819	0.0	0.092	0.908	1.080	0.0
100°	4.116×10^6	7.189	4113.62	0.836	0.164	0.874	-572.21
110°	5.584×10^6	14.806	0.0	0.218	0.787	0.424	0.0
120°	2.220×10^7	19.256	2306.033	0.079	0.927	0.326	-119.647
140°	9.204×10^7	35.575	0.0	0.069	0.923	0.177	0.0

TABLE 6.1 – Critical values Ra_c , k_c and ω_c together with the energy budget terms B and I and the resulting wavelength z_k and the phase velocity u_p for the modes in Figures 6.2, 6.3 and 6.4.

perturbation are organised into two cellular structures which are equal in size and do not propagate along the z -axis. The following two modes, at $\alpha = 0^\circ$ and $\alpha = 30^\circ$ in Figures 6.2b and 6.2c respectively, are oscillatory modes with $\omega_c \neq 0$. As such, the perturbation does not have a cellular structure. The former mode at $\alpha = 0^\circ$, is part of the upper branch of the basic state and belongs to the purple mode in Figure 6.1. Its basic flow features one large vortex and two recirculation zones in the top left and bottom right corners of the cavity. This flow structure is almost identical with one of the solutions previously discussed in Chapter 5 with $Ra = 2.5 \times 10^4$ and conducting lateral walls. The aforementioned recirculation zones are also visible at $\alpha = 30^\circ$. The areas where the perturbation is stronger in both modes are concentrated mainly around the heated walls, particularly in Figure 6.2c. The instability of all aforementioned modes is mainly driven by buoyancy since $B > I$ as seen in Table 6.1.

The next mode, shown in Figure 6.3a at $\alpha = 80^\circ$, is also an oscillatory mode with a higher phase velocity since its frequency $|\omega_c| = 1152.91$ is much higher than the previous modes, which was $|\omega_c| = 93.659$ and $|\omega_c| = 177.586$ respectively. The basic flow has no visible recirculation zones in the corners. Instead, two new zones of recirculation have appeared close to the centre of the cavity, placed diagonally from each other. As the Rayleigh number increases, we can also observe how the thermal stratification becomes stronger and the isotherms are nearly perpendicular to \mathbf{g} . Buoyancy forces once again drive the instability and the regions with the strongest perturbations are gathered around the corners of the cavity, particularly on the bottom left and top right corners where the flow is accelerated.

The mode at $\alpha = 90^\circ$, shown in Figure 6.3b, with the conducting walls placed horizontally, has a similar basic flow to $\alpha = 80^\circ$. The isosurfaces with the strongest perturbations are equally spread around the cavity and are slightly more amplified around the regions of recirculation of the basic state. In fact, at $\alpha = 90^\circ$ buoyancy is responsible for only 9.2% of the perturbation kinetic energy growth rate. The components of I are shown Table 6.2 for all modes in which the instability is driven by inertia with $I > B$. In this particular mode, we can see that $I_2 > I_4$ which is an indication that the inertial instability is driven by lift up in the boundary layer as

α	I_1	I_2	I_3	I_4	I
90°	0.040	0.601	0.077	0.191	0.908
110°	0.0	0.320	0.128	0.340	0.787
120°	0.078	0.165	0.193	0.491	0.927
140°	0.009	0.122	0.187	0.606	0.923

TABLE 6.2 – Decomposition of the inertial contribution I into I_1 , I_2 , I_3 and I_4 in modes where inertia is dominant with $I > B$.

opposed to a flow deceleration.

The last mode in this figure at $\alpha = 100^\circ$ and in Figure 6.3c, has the highest frequency out of all the plotted modes with $\omega_c = 4113.62$, which also leads to the highest absolute phase velocity of $|u_p| = 572.21$. Interestingly, the perturbation is stronger around the bottom left and top right corners much like the mode at $\alpha = 80^\circ$. Moreover, buoyancy drives the instability with $B = 0.836$ as opposed to inertia with $I = 0.164$ which explains the similar structure of the perturbation isosurfaces with the mode at $\alpha = 80^\circ$, since both modes are destabilised mainly due to buoyancy. As such, the perturbation is stronger in the regions where buoyancy forces drive the flow such as the bottom left and upper right corners of the cavity.

By increasing the inclination angle, the wavenumber sharply increases which leads to smaller wavelengths as seen in Figure 6.4. Namely, we see an increase from $k = 7.189$ at $\alpha = 100^\circ$ to $k = 14.806$ at $\alpha = 110^\circ$, which corresponds to a change of 105%. In all of the modes of this figure, inertia is the dominant factor that destabilises the flow with $I > B$. As such, the components of I of these modes are shown in 6.2. At $\alpha = 110^\circ$, shown in Figure 6.4a, the recirculation zones start to migrate towards the boundaries due to the high velocity in these regions. The perturbation is stronger only on the boundaries and also in the regions of recirculation where the flow is decelerated. Due to $\omega_c = 0$, there is no propagation on the z -axis. The inertial instability is driven almost equally by both lift up and deceleration since $I_2 \approx I_4$. As of the next mode at $\alpha = 120^\circ$, shown in Figure 6.4b, the isosurfaces with the strongest perturbation are entirely located on the bottom and upper corners of the cavity, where a deceleration of the basic flow occurs. This can also be verified by the components of I , since $I_4 > I_2$ for this mode. As the inclination angle increases, the magnitude of the velocity on the boundaries increases at the expense of the velocity in the centre of the cavity. Moreover, the temperature field of the basic state becomes steadily more stratified as the critical Rayleigh number increases with larger angles. Both of these facts can be observed in detail in the last mode at $\alpha = 140^\circ$, shown in Figure 6.4c. The flow deceleration in the bottom and upper corners of the cavity is the dominant source of instability with $I_4 \approx 5I_2$.

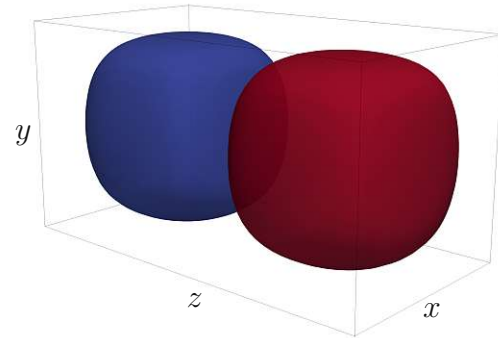
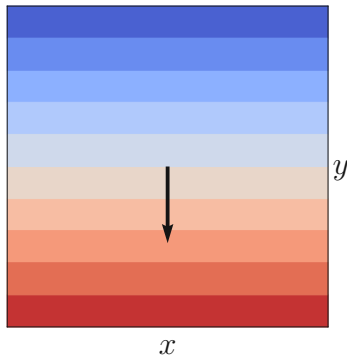
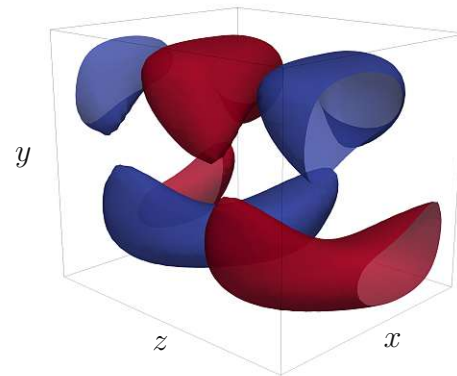
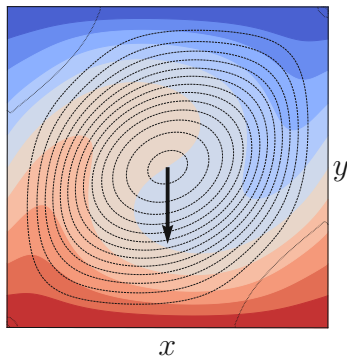
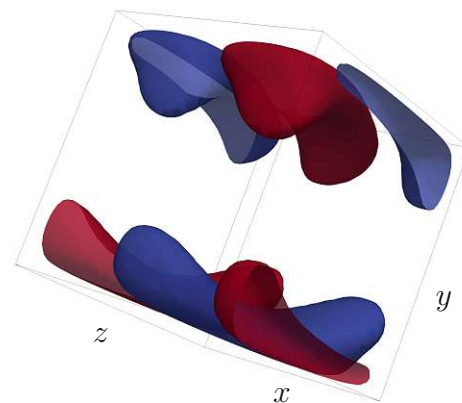
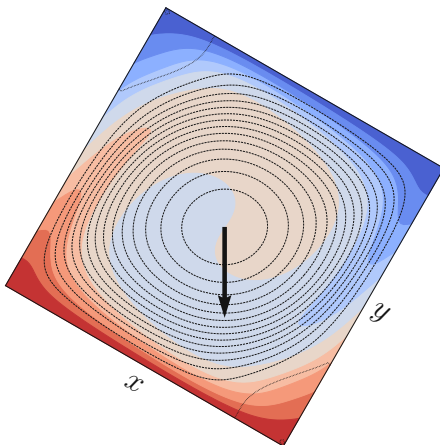
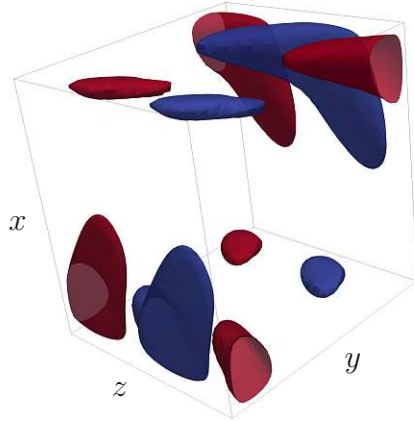
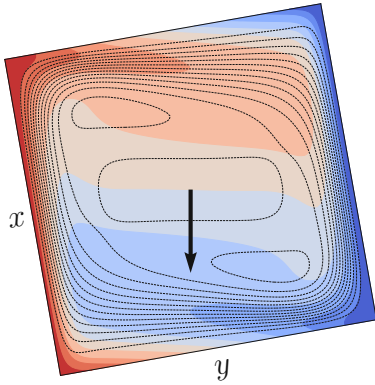
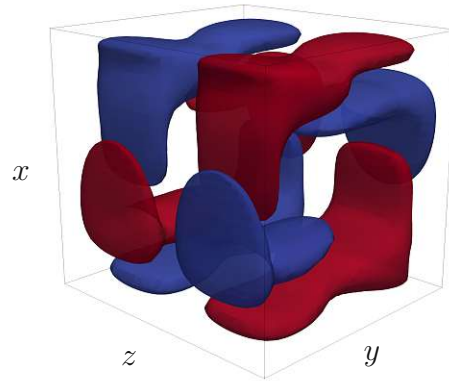
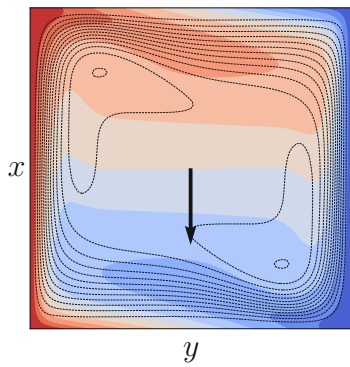
(a) $\alpha = 0^\circ$, lower branch(b) $\alpha = 0^\circ$, upper branch(c) $\alpha = 30^\circ$ 

FIGURE 6.2 – Basic flow (left column) and temperature perturbation isosurfaces (right column) at the angles 0° (both branches) and 30° . In both columns, the cavity is tilted to match the direction of gravity, which is indicated by the black arrow on the left column. On the right, the length of the three dimensional cavity on the z -axis is equal to one wavelength. Areas in red indicate $\theta > 0$ and in blue $\theta < 0$. Dashed streamlines indicate a clockwise flow and full streamlines a counter-clockwise flow.

(a) $\alpha = 80^\circ$



(b) $\alpha = 90^\circ$



(c) $\alpha = 100^\circ$

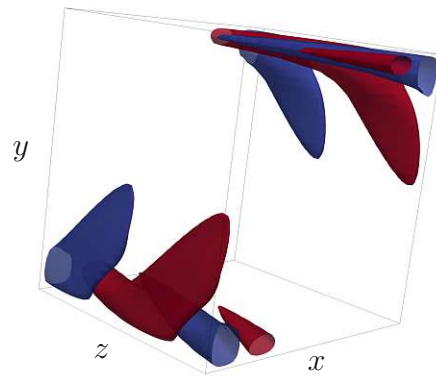
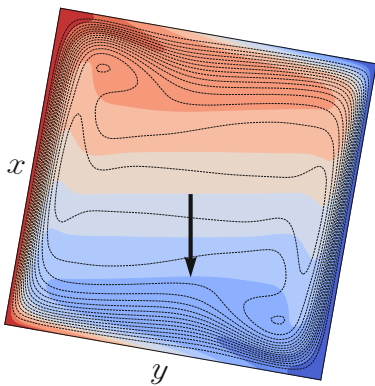


FIGURE 6.3 – Basic flow (left column) and temperature perturbation (right column) at the angles 80° , 90° and 100° . The plots follow the notation in Figure 6.2.

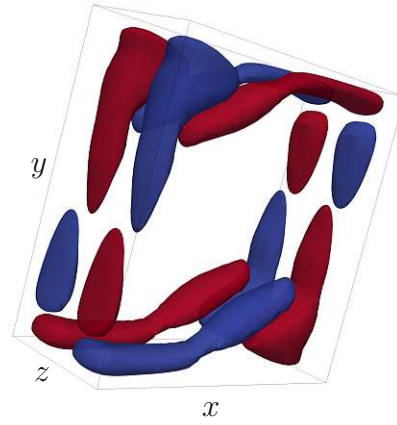
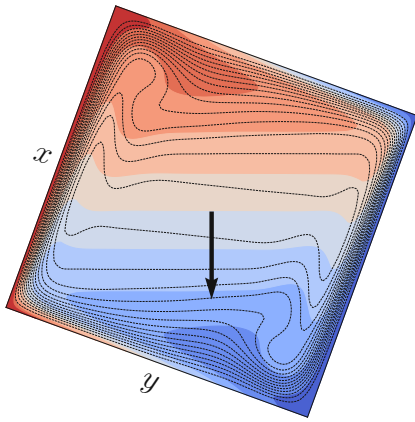
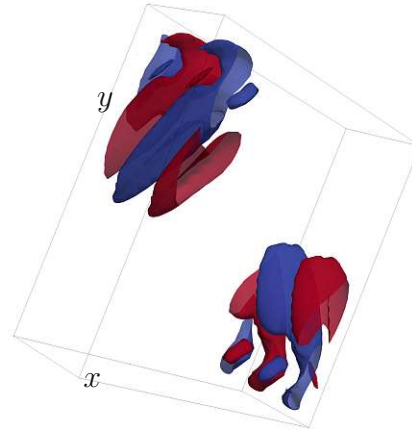
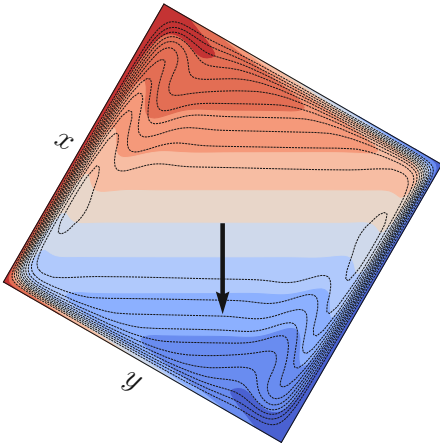
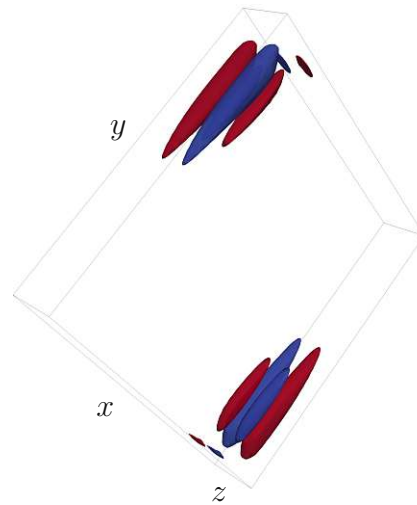
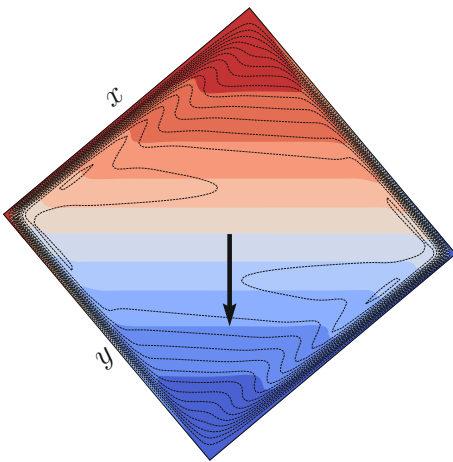
(a) $\alpha = 110^\circ$ (b) $\alpha = 120^\circ$ (c) $\alpha = 140^\circ$ 

FIGURE 6.4 – Basic flow (left column) and temperature perturbation (right column) at the angles 110° , 120° and 140° . The plots follow the notation in Figure 6.2.

7

Conclusion

In this thesis, we studied the state multiplicity and the flow stability inside an inclined differentially heated cavity for air with $\text{Pr} = 0.71$.

7.1 Steady State Multiplicity

In Chapter 5, we studied the steady state multiplicity in an inclined cavity which occurs when the fluid is heated from below. Two opposing walls of the cavity were heated and cooled respectively and the remaining lateral walls were either perfectly conducting or adiabatic. For both cases, the flow at two different Rayleigh numbers was studied extensively, namely at $\text{Ra} = 2.5 \times 10^4$ and $\text{Ra} = 10^5$. By studying the heat flux on the hot cavity wall using the Nusselt number Nu_H as a function of the inclination angle α , we showed how multiple steady states can exist through saddle node bifurcation points. Moreover, we discussed how changing either the Rayleigh number or the boundary condition of the lateral walls affects the state multiplicity.

The multiple steady states are grouped in independent solution sets. Many of the steady states at $\alpha = 0^\circ$ in these sets originate from the modes of the unstable stratification, which Boullé *et al.* [8] showed in their paper where they considered adiabatic lateral walls and otherwise identical parameters to our problem. Steady states that originate from these modes can emerge only if the neutral Rayleigh number of these modes has been surpassed. As such, higher Rayleigh numbers allow the emergence of more such states and also lead to a higher number of solution sets. Higher Rayleigh numbers also lead to higher Nusselt numbers, a decrease of the maximum angle span of the main solution set and a displacement of the minimum point on the main solution set away from the symmetry axis of $\alpha = 0^\circ$ in both directions, resulting in two minima instead of one.

An adiabatic boundary condition for the lateral walls leads to higher Nusselt numbers and a larger angle interval where state multiplicity is realisable. On the contrary, a conducting boundary condition leads to a smaller angle interval where state multiplicity is realisable and effectively decreases the maximum angle span of all solution sets.

Based on the results of Boullé *et al.* [8], there are probably more steady states than those presented in this thesis when considering adiabatic lateral walls and as such, future work on this subject could reveal them. Moreover, it would also be interesting to investigate the effect that different Rayleigh numbers have on the state multiplicity and the solution sets.

7.2 Linear Stability Analysis

In Chapter 6, we studied the flow stability using a linear stability analysis with perfectly conducting lateral walls and presented the critical curve of the Rayleigh number and other critical parameters as a function of the inclination angle. The most important find of this study was that the critical Rayleigh number increases with larger angles. On the other hand, the flow is most unstable at $\alpha = 0^\circ$, at the lower branch of the state multiplicity where the basic state is motionless with a stratified temperature field. The wavelength of the perturbation is significantly higher at smaller angles, in particular on the lower branch at $\alpha = 0^\circ$. Larger angles result to a much smaller wavelength instead. Most critical modes are stationary and most critical oscillating modes are centered around $\alpha = 90^\circ$ in the critical curve.

Moreover, we analysed the energy budget of the perturbation in order to determine the dominant factor which drives the instability mechanism, which is either inertia or buoyancy. With the exception of two modes close to $\alpha = 100^\circ$, there is a clear distinction between the angle intervals of dominance of inertia and buoyancy, in which buoyancy drives the instability with $\alpha < 86^\circ$ and inertia with $\alpha > 86^\circ$. Thus, buoyancy is more dominant in the instability mechanism at lower Rayleigh numbers. As for higher Rayleigh numbers, inertia is more dominant and at larger angles it is contributing to the instability due to a deceleration of the flow at two opposite corners of the cavity. Moreover, modes with $\omega_c \neq 0$ are usually destabilised by buoyancy rather than inertia. The regions with the strongest perturbations within the cavity were located in the majority of the plotted modes at the boundaries of the cavity and particularly at the corners.

Future work could include studying the flow stability with adiabatic instead of conducting lateral walls, particularly in the angle interval of state multiplicity, centered around $\alpha = 0^\circ$. Moreover, another interesting subject of research would be to study the effect of an inclination around the y instead of the z -axis, or even a combination of the two. The tools that were developed to conduct the linear stability analysis in this thesis are capable of performing both of the aforementioned tasks.

Bibliography

- [1] ADACHI, T. & MIZUSHIMA, J. 1996 Stability of the thermal convection in a tilted square cavity. *J. Phys. Soc. Japan* **65**, 1686–1698.
- [2] ALBENSOEDER, S., KUHLMANN, H. C. & RATH, H. J. 2001 Multiplicity of steady two-dimensional flows in two-sided lid-driven cavities. *Theor. Comput. Fluid Dyn.* **14**, 223–241.
- [3] ALBENSOEDER, S., KUHLMANN, H. C. & RATH, H. J. 2001 Three-dimensional centrifugal-flow instabilities in the lid-driven-cavity problem. *Phys. Fluids* **13**, 121–135.
- [4] ALNAES, M. S., BLECHTA, J., HAKE, J., JOHANSSON, A., KEHLET, B., LOGG, A., RICHARDSON, C., RING, J., ROGNES, M. E. & WELLS, G. N. 2015 The FEniCS Project Version 1.5. *Arch. Numer. Softw.* **3**, 9–23.
- [5] AMESTOY, P., DUFF, I. S., L'EXCELLENT, J.-Y. & KOSTER, J. 2002 MULTifrontal Massively Parallel Solver (MUMPS version 4.2 beta) user's guide. *Tech. Rep.*. Laboratoire de l'informatique du parallélisme.
- [6] ARNOLDI, W. E. 1951 The principle of minimized iterations in the solution of the matrix eigenvalue problem. *Q. Appl. Math.* **9**, 17–29.
- [7] BÉNARD, H. 1901 Les tourbillons cellulaires dans une nappe liquide. - Méthodes optiques d'observation et d'enregistrement. *J. Phys. Théorique Appliquée* **10**, 254–266.
- [8] BOULLÉ, N., DALLAS, V. & FARRELL, P. E. 2022 Bifurcation analysis of two-dimensional Rayleigh-Bénard convection using deflation. *Phys. Rev. E* **105**, 055106.
- [9] CHANDRASEKHAR, S. 1961 *Hydrodynamic and Hydromagnetic Stability*. Oxford University Press.
- [10] CHARLSON, G. S. & SANI, R. L. 1970 Thermoconvective instability in a bounded cylindrical fluid layer. *Int. J. Heat Mass Transf.* **13**, 1479–1496.
- [11] CHASSIGNET, E. P., CENEDESE, C. & VERRON, J. 2012 Buoyancy-driven flows. In *Buoyancy-Driven Flows*, chap. 1. Cambridge: Cambridge University Press.
- [12] DAVIS, S. H. 1967 Convection in a box: Linear theory. *J. Fluid Mech.* **30**, 465–478.
- [13] DRAZIN, P. G. 2002 *Introduction to Hydrodynamic Stability*. Cambridge: Cambridge University Press.
- [14] DRAZIN, P. G. & REID, W. H. 2004 *Hydrodynamic Stability*, 2nd edn. Cambridge: Cambridge University Press.
- [15] DURÁN, R. G. 2008 Mixed finite element methods. In *Lect. Notes Math.* (ed. Daniele Boffi & Lucia Gastaldi), pp. 1–44. Berlin, Heidelberg: Springer.
- [16] FISCHER, P. F., LOTTES, J. W. & KERKEMEIER, S. G. 2008 NEK5000 Webpage.

- [17] GELFGAT, A. Y., BAR-YOSEPH, P. Z. & YARIN, A. L. 1999 Stability of multiple steady states of convection in laterally heated cavities. *J. Fluid Mech.* **388**, 315–334.
- [18] GELFGAT, A. Y. & TANASAWA, I. 1994 Numerical analysis of oscillatory instability of buoyancy convection with the Galerkin spectral method. *Numer. Heat Transf. Part A Appl.* **25**, 627–648.
- [19] HARRIS, C. R., MILLMAN, K. J., VAN DER WALT, S. J., GOMMERS, R., VIRTANEN, P., COURNAPEAU, D., WIESER, E., TAYLOR, J., BERG, S., SMITH, N. J., KERN, R., PICUS, M., HOYER, S., VAN KERKWIJK, M. H., BRETT, M., HALDANE, A., DEL RÍO, J. F., WIEBE, M., PETERSON, P., GÉRARD-MARCHANT, P., SHEPPARD, K., REDDY, T., WECKESSER, W., ABBASI, H., GOHLKE, C. & OLIPHANT, T. E. 2020 Array programming with NumPy. *Nature* **585**, 357–362.
- [20] HART, J. 1983 A note on the stability of low-Prandtl-number Hadley circulations. *J. Fluid Mech.* **132**, 271–281.
- [21] HART, J. E. 1971 Stability of the flow in a differentially heated inclined box. *J. Fluid Mech.* **47**, 547–576.
- [22] HIROYUKI, O., KAZUMITSU, Y., HAYATOSHI, S. & CHURCHILL, S. W. 1974 Natural circulation in an inclined rectangular channel heated on one side and cooled on the opposing side. *Int. J. Heat Mass Transf.* **17**, 1209–1217.
- [23] HUELSZ, G. & RECHTMAN, R. 2013 Heat transfer due to natural convection in an inclined square cavity using the lattice Boltzmann equation method. *Int. J. Therm. Sci.* **65**, 111–119.
- [24] HUNTER, J. D. 2007 Matplotlib: A 2D graphics environment. *Comput. Sci. Eng.* **9**, 90–95.
- [25] JANSSEN, R. J. & HENKES, R. A. 1995 Influence of Prandtl number on instability mechanisms and transition in a differentially heated square cavity. *J. Fluid Mech.* **290**, 319–344.
- [26] KOSCHMIEDER, E. L. & PALLAS, S. G. 1974 Heat transfer through a shallow, horizontal convecting fluid layer. *Int. J. Heat Mass Transf.* **17**, 991–1002.
- [27] KOSKY, P., BALMER, R., KEAT, W. & WISE, G. 2021 Mechanical Engineering. In *Explor. Eng.*, chap. 14, pp. 317–340. Elsevier.
- [28] KUHLMANN, H. C. 2018 Hydrodynamic stability theory.
- [29] LANDAU, L. D. & LIFSHITZ, E. M. 2013 *Fluid Mechanics: Volume 6*, bd. 6 edn. Elsevier Science Publishers B. V.
- [30] LEHOUCQ, R. B. & SORENSEN, D. C. 1996 Deflation techniques for an implicitly restarted Arnoldi iteration. *SIAM J. Matrix Anal. Appl.* **17**, 789–821.
- [31] MARTYNYENKO, O. G. & KHRAMTSOV, P. P. 2005 Free-Convective Heat Transfer. In *Free. Heat Transf.*, chap. 1, pp. 1, 13. Berlin/Heidelberg: Springer Berlin, Heidelberg.
- [32] OTTOSEN, N. S. & PETERSON, H. 1992 Introduction to the Finite Element Method. In *Introd. to Finite Elem. Method*, chap. 4, pp. 48–64. Prentice-Hall.

- [33] PILLER, M., POLIDORO, S. & STALIO, E. 2014 Multiplicity of solutions for laminar, fully-developed natural convection in inclined, parallel-plate channels. *Int. J. Heat Mass Transf.* **79**, 1014–1026.
- [34] RAYLEIGH, L. 1916 LIX. On convection currents in a horizontal layer of fluid, when the higher temperature is on the under side. *London, Edinburgh, Dublin Philos. Mag. J. Sci.* **32**, 529–546.
- [35] SALINGER, A., BOU-RABEE, N., BURROUGHS, E. A., PAWLOWSKI, R., LEHOUCQ, R. B., ROMERO, L. A. & WILKES, E. D. 2002 LOCA 1.0 Library of Continuation Algorithms: Theory and Implementation Manual. *Tech. Rep.*. Sandia National Laboratories (SNL), Albuquerque, NM, and Livermore, CA (United States).
- [36] VIRTANEN, P., GOMMERS, R., OLIPHANT, T. E., HABERLAND, M., REDDY, T., COURNAPEAU, D., BUROVSKI, E., PETERSON, P., WECKESSER, W., BRIGHT, J., VAN DER WALT, S. J., BRETT, M., WILSON, J., MILLMAN, K. J., MAYOROV, N., NELSON, A. R. J., JONES, E., KERN, R., LARSON, E., CAREY, C. J., POLAT, I., FENG, Y., MOORE, E. W., VANDERPLAS, J., LAXALDE, D., PERKTOLD, J., CIMRMAN, R., HENRIKSEN, I., QUINTERO, E. A., HARRIS, C. R., ARCHIBALD, A. M., RIBEIRO, A. H., PEDREGOSA, F., VAN MULBREGT, P., VIJAYKUMAR, A., BARDELLI, A. P., ROTHBERG, A., HILBOLL, A., KLOECKNER, A., SCOPATZ, A., LEE, A., ROKEM, A., WOODS, C. N., FULTON, C., MASSON, C., HÄGGSTRÖM, C., FITZGERALD, C., NICHOLSON, D. A., HAGEN, D. R., PASECHNIK, D. V., OLIVETTI, E., MARTIN, E., WIESER, E., SILVA, F., LENDERS, F., WILHELM, F., YOUNG, G., PRICE, G. A., INGOLD, G.-L., ALLEN, G. E., LEE, G. R., AUDREN, H., PROBST, I., DIETRICH, J. P., SILTERRA, J., WEBBER, J. T., SLAVIČ, J., NOTHMAN, J., BUCHNER, J., KULICK, J., SCHÖNBERGER, J. L., DE MIRANDA CARDOSO, J. V., REIMER, J., HARRINGTON, J., RODRÍGUEZ, J. L. C., NUNEZ-IGLESIAS, J., KUCZYNSKI, J., TRITZ, K., THOMA, M., NEWVILLE, M., KÜMMERER, M., BOLINGBROKE, M., TARTRE, M., PAK, M., SMITH, N. J., NOWACZYK, N., SHEBANOV, N., PAVLYK, O., BRODTKORB, P. A., LEE, P., MCGIBBON, R. T., FELDBAUER, R., LEWIS, S., TYGIER, S., SIEVERT, S., VIGNA, S., PETERSON, S., MORE, S., PUDLIK, T., OSHIMA, T., PINGEL, T. J., ROBITAILLE, T. P., SPURA, T., JONES, T. R., CERA, T., LESLIE, T., ZITO, T., KRAUSS, T., UPADHYAY, U., HALCHENKO, Y. O. & VÁZQUEZ-BAEZA, Y. 2020 SciPy 1.0: fundamental algorithms for scientific computing in Python. *Nat. Methods* **17**, 261–272.
- [37] WINTERS, K. H. 1987 Hopf bifurcation in the double-glazing problem with conducting boundaries. *J. Heat Transfer* **109**, 894–898.
- [38] XIN, S. & LE QUÉRE, P. 2001 Linear stability analyses of natural convection flows in a differentially heated square cavity with conducting horizontal walls. *Phys. Fluids* **13**, 2529–2542.

